UNIVERSITY OF OKLAHOMA

GRADUATE COLLEGE

COMPUTATIONAL INVESTIGATION OF NON-COVALENT STABILIZATION OF NANOPARTICLE SUSPENSIONS AND THEIR PROPAGATION IN POROUS MEDIA

A DISSERTATION

SUBMITTED TO THE GRADUATE FALCUTY

in partial fulfillment of the requirements for the

Degree of

DOCTOR OF PHILOSOPHY

By

MINH DUC MINH VO
Norman, Oklahoma
2016

COMPUTATIONAL INVESTIGATION OF NON-COVALENT STABILIZATION OF NANOPARTICLE SUSPENSIONS AND THEIR PROPAGATION IN POROUS MEDIA

A DISSERATION APPROVED FOR THE
SCHOOL OF CHEMICAL, BIOLOGICAL AND MATERIALS ENGINEERING

BY

_____

Dr. Dimitrios V. Papavassiliou, Chair

_____

Dr. Jeffrey H. Harwell

_____

Dr. Daniel E. Resasco

_____

Dr. Robert L. Shambaugh

_____

Dr. Benjamin (Bor-Jier) Shiau

For my grandparents, my parents, my wife, and my little son "Carbon"

Acknowledgements

I would like to acknowledge my advisor, Dr. Dimitrios Papavassiliou, for his understanding and patience during my PhD life. This work absolutely can never be done without his exceptional support, guidance and encouragement. I also want to thank the members of my committee, including Dr. Jeffrey H. Harwell, Dr. Daniel E. Resasco, Dr. Robert Shambaugh, and Dr. Benjamin (Bor-Jier) Shiau for their time and helpful suggestions.

Besides, financial support from Advanced Energy Consortium (http://www.beg.utexas.edu/aec/) (AEC BEG08–022) is gratefully acknowledged. I would like to thank the computational resources support from the OU Supercomputing Center for Education & Research (OSCER) and the Texas Advanced Computing Center under XSEDE allocation CTS-090025.

In addition, I am also grateful to my colleagues and friends for useful discussions. I really appreciate the introduction of Dr. Hai Duong, Dr. Phuong Le and Dr. Luong Nguyen to my advisor.

Last but not least, I would like to thank my family for their unending care and love.

Table of Contents

List of Tables

List of Figures

Abstract

In this study, Dissipative Particle Dynamics (DPD) and Lagrangian Particle Tracking (LPT) methods were used to investigate computationally the non-covalent stabilization of carbon nanotubes (CNT) in water by using polymers and surfactants as well as the propagation of stabilized nanoparticles (NPs) in porous media. First of all, the interaction parameters of CNT and water in DPD was validated by comparing with results from Molecular Dynamics (MD) simulations in case of the water flow past an array of single-walled carbon nanotubes (SWCNT) in different Reynolds number flows. *For polymer stabilization*, it was presented the conformation of PVP molecules on carbon nanoparticle (CNP) surface. Depending on the surface area and shape of NPs, there were three configurations of polymer molecules when attached on CNP surface including trains, loops and tails. The physical adsorption of PVP on CNP depended on the shear rate of the flow. There were three possible states of NPs coated with polymer under the shear. They consisted of adsorbed, shear-affected and separated states. The range of shear rate for each state was determined for CNPs with different shapes (sphere, cylinder and graphene-like). *For surfactant stabilization*, CNT surface changed from hydrophobic to hydrophilic in the presence of the surfactants alfoterra 123-8s (AF) and tergitol 15-s-40 (TG) surfactant adsorption. This leads to increase the solubility of CNT in water. In our simulation, it was found that AF and TG surfactant primarily formed both hemi-micelles and random adsorption on CNT surface. The assembly of surfactants on CNT relied on the interaction of the surfactant tail and the CNT surface. For surfactants in solution, most micelles had spherical shape. In the binary surfactant system, the presence of TG on the CNT surface provided a considerable hydrophilic steric effect, due to the ethylene oxide

(EO) groups of TG molecules. It was also seen that the adsorption of AF was more favorable than TG on the CNT surface. Our results are applicable, in a qualitative sense, to the more general case of adsorption of surfactants on the hydrophobic surface of cylindrically-shaped nanoscale objects. Moreover, we found that sodium dodecyl sulfate (SDS) surfactant can adsorb inside surface of SWCNT if diameter of SWCNT is larger than 3 nm. When SDS was adsorbed in the hollow part of the SWCNT, the behavior of water inside the nanotube was found to be significantly changed. In addition, SDS molecules increased the retention of water beads inside SWCNT (diameter $\geq$ 3nm), while water diffusivity was decreased. Depending on the concentration of surfactant, SDS inside SWCNT can accumulate from 1% to 13% of the total of adsorbed surfactant. Besides, the steric effect of adsorbed PVP molecules in CNT coated PVP particle was evaluated by calculating the interaction force between particle – particle and particle – surface. The computations indicated that the repulsion of PVP polymer reduced the agglomeration of CNTs in solution and their deposition on silica surface. Finally, the propagation of nanoparticles (NPs) in porous media was also examined in both LPT and DPD simulation. It was found that drag force and random force were dominant for a single NP movement. Without the surface attraction, both spherical and cylindrical NPs can propagate through porous media. Spherical NPs underwent more collisions with the suface than cylindrical ones due to the more symmetric geometry in all directions of the sphere. For a rigid cylindrical NPs, the change of its orientation after each collision was a primary way to go around a solid surface. The distribution of orientation angle of cylindrical NPs indicated the analogous results between LPT and DPD methods.

Chapter 1. Introduction

The global demand for energy has increased rapidly in the last half century while demand is anticipated to keep growing over the next 20 years because of the growth of world population and global economy [1]. Currently, the main sources of energy are fossil fuels, but their availability is limited and they are expected to be depleted in the near future. Fossil fuels remain the dominant form of energy providing around 60% of the additional energy demands and accounting for almost 80% of total energy supplies in 2035 [2]. It is important to note that about two thirds of oil capacity in many reservoirs cannot be recovered by using conventional production methods [3]. There are large amounts of trapped oil in reservoirs, which in some cases can be harvested with enhanced oil recovery (EOR) processes. The industry needs stunning discoveries in order to open up the possibility of moving beyond current sources for energy supply by introducing technologies that are more efficient and environmentally sound.

Recently, applications of nanotechnology have been considered for employment in the oil and gas industry (exploration, drilling and production) [4]. Nanoparticles (NPs) can be used in hydraulic fracturing; enhanced oil recovery (EOR) process; water-flood and inter-well reservoir characterization; wellbore measurements and extended well logging [5]. In EOR process, NPs can increase significantly oil recovery in a reservoir through changing surface tension [1]. The viscosity of a fluid injected to displace oil (like water, CO_2 or surfactant solutions) is often smaller than the viscosity of the oil phase. The viscosity of the injected fluid can reach an optimum level by adding NPs. It leads to the net effect of improving the mobility as well as the oil recovery efficiency. Besides, NPs can be used as nanomaterial sensors, micro-fabricated sensors [5], modifiers of transport

properties, nano-scale vehicles for catalyst and contrast agents in reservoir system [6]. In these applications, the propagation of NPs in porous media (such as rock or sand in a reservoir) has a significant effect on the efficiency of the whole process. NPs should then exhibit long-term dispersion stability and should propagate long distances in reservoir rocks with minimal retention.

In addition, carbon nanotubes (CNTs) could be good candidates in surfactant EOR techniques because they can deliver surfactants to the water/oil interface while reducing surfactant adsorption to the rock [7]. The hydrophobic surface of a CNT is favorable for surfactant tail adsorption [8]. In this case, surfactants can stabilize the CNT suspension, while the CNTs take a role as surfactant carriers. CNTs stabilized by surfactants could propagate through the oil reservoir, reach the oil-water interface and then release the surfactant to lower the interfacial tension (IFT). However, there have been many difficulties with this idea, starting with the feasibility of surfactant adsorption on the CNTs.

The aim of the present study is to investigate the non-covalent stabilization of NP suspensions by using surfactants or polymers, as well as the propagation of NPs in porous media through the use of both macroscopic scale (Lagrangian Particle Tracking method) and mesoscopic scale (Dissipative Particle Dynamics) simulations.

1.1. Dispersion of nanoparticles in solution

NPs are particles with at least one dimension that falls into the range of 1-100 nm. They can be considered as a bridge between bulk materials and atomic or molecular structures [9]. Physical properties of the bulk material are constant regardless of its dimensions, but size-dependent properties are often observed at the nanoscale. The properties of materials

vary when their size approaches the nanoscale and the surface to volume ratio becomes remarkable. For bulk materials larger than one micrometer, the percentage of atoms at the surface is tiny when compared to the total number of atoms of the material. Therefore, the properties of NPs become unique, and sometimes unexpected, due to their large surface area and high surface to volume ratio.

Many commercial NP products are often sold and delivered as dry powders. If NPs are aggregated, their properties will be different from those of primary NPs [10]. Most of NPs cannot be kept isolated in the nanoscale range when dispersing in water [11]. Generally, NPs can remain as singlets or form agglomerates, or remain as aggregates after dispersing in solution. Typically, when agglomerated nanoparticle samples are released to a solution they can be separated by overcoming the weaker attractive forces, whereas the aggregated NPs cannot be separated [12]. Murdock and co-workers used Dynamic Light Scattering (DLS) techniques to characterize the dispersion of NPs in solution. Experimental results showed that depending on the material, NPs do not necessarily retain their ‘‘nano-size” in solution. With the exception of SiO_2, NPs and the Ag 10 nm dispersed particles, all of investigated materials tended to form large agglomerates that fell above the 100 nm size [13].

The dispersion of NPs is one of the most challenging problems that we have to overcome in variety of application in chemistry, biology, medicine, and material science. In the handling of NPs during a process sequence, flocculation or agglomeration of NPs should be avoided. The agglomeration of NPs in solution could not only increase their size but it can also lead to their settling out due to gravity. Successful dispersion of NPs would allow them to be chemically stable in solution, avoid flocculation, coagulation or gel

formation. The desired exceptional properties of NPs in applications would then be preserved.

According to Derjaguin, Verway, Landau, and Overbeek (DLVO) theory, the stability of a particle in solution is determined by the sum of Van der Waals attractive and electrical double layer repulsive forces that exist between particles as they approach each other due to Brownian motion [14]. If the attractive force is larger than the repulsive force, the two particles will collide, stick together and the suspension is not stable. If the particles have a sufficiently high repulsion, the particle suspensions will exist in stable state. So, the repulsive forces between NPs must be dominant in order to disperse effectively NPs in solution. Based on types of repulsive forces between NPs, there are two mechanisms of dispersion NPs in solution: one is electrostatic repulsion of the charged particle surfaces, and another is steric repulsion induced by adsorption of high-entropy polymers [15].

For electrostatic stabilization, surface charge can be modified through one or more of the following mechanisms: preferential adsorption of ions, dissociation of surface charged species, isomorphic substitution of ions, accumulation or depletion of electrons at the surface, and physical adsorption of charged species onto the surface [14]. Stabilization can be achieved by adding a charge to NPs so that they can repel one another especially under the influence of the pH of the solution. Liu et al. used DLS measurements to explore the dispersion of TiO_2, CeO_2, and C60 NPs over a wide range of pH (3-10) and ionic strength (0.01-156 mM) [16]. Using Monte Carlo simulations, it was demonstrated quantitatively that NP size increased both with ionic strength and as the solution pH approached the isoelectric point. Additionally, barite NPs were dispersed stably in aqueous solution by electrostatic stabilization [17]. Results indicated that the stable state

of dispersion was accomplished in acidic pH range with low solid loading due to the low viscosity and high zeta potential in the absence of dispersant. The zeta potential is an important key indicator of the stability of colloidal dispersions. The magnitude of the zeta potential presents the degree of electrostatic repulsion between adjacent surfaces.

For steric stabilization, the mechanism is based on the steric repulsion between molecules adsorbed on neighboring particles. Size and chemical nature of these molecules control the degree of stabilization. Due to geometric constraints around NPs, large and bulky molecules contribute a significantly effective stabilization, and an elongated or conical geometry is advantageous to retain the approaching NPs apart. Zhu et al. improved the stability of graphite NPs in water by adding polyvinylpyrrolidone (PVP) polymer as a dispersant [18]. It was found that the surface of the graphite NPs is gradually coated by PVP molecules with the increase of PVP concentration. The highest stability of graphite NPs in solution was obtained when the PVP concentration was 0.35-0.6%. Tang et al. used polymethacrylic acid (PMMA) to stabilize ZnO NPs in aqueous systems [19]. The steric effect of poly(zinc methacrylate) complex on the surface of ZnO was generated by interacting of the hydroxyl groups of NP surface and carboxyl groups (COO–) of PMAA. The presence of PMMA polymer on NPs surface did not only improve significantly the dispersion of ZnO NPs, but also retained the crystalline structure of the ZnO NPs according to the X-ray diffraction patterns.

Furthermore, both electrostatic and steric stabilization can be utilized (called electro-steric stabilization) to disperse NPs in solution by using polyelectrolytes. These are polymer chains with numerous dissociable groups. Hang et al. carried out electro-steric stabilization of barite NPs by adding of sodium polyacrylate (PAA-Na) to move the

isoelectric point (IEP) of barite NPs to lower pH and increase the negative zeta potential in a large range of pH above the IEP [17]. The adsorption of PAA was correlated to the fraction of dissociated polymer and the net surface charge of NPs at different pH values.

In addition, it has been proved that ultra-sonication is also a useful tool to disperse NPs and avoid agglomeration in aqueous suspensions [20-22]. Under ultrasonic irradiation, shock waves were generated by collapsing cavitations that improved collisions among particles. So, the interaction between NPs was eroded, and NPs were separated due to these collisions. Basically, there are three different mechanisms of NPs separation under ultra-sonication. These are rupture, erosion, and shattering. Nguyen et al. showed that alumina NPs at low concentration in suspensions were stabilized by electrostatic forces without the need for dispersants after undergoing ultrasonic de-agglomeration [23]. The presence of electrostatic repulsion and adsorption of surfactants onto NP surfaces did not have a significant contribution on the aggregate size of NPs. Tso et al. investigated the stability and morphology of three commercial metal NPs (TiO_2, ZnO, SiO_2) in aqueous solution [11]. It was found out that ultra-sonication is the most effective procedure for disaggregating these NPs in water. After ultrasonication, SiO_2 and TiO_2 suspensions were more stable than ZnO suspension. ZnO NPs aggregated rapidly because of electrostatical instability.

1.2. The transport of NPs in porous media

Due to nanotechnology development and applications in industry, transport of NPs has obtained a lot of attention in the past decades. However, there are still many possible side effects of engineered NPs when released into the environment [24]. For example, nanomaterials like NPs may leak and accumulate in ground water resources or

agricultural fields in the process of their production, use, or disposal. This could create a hazardous situation for human health and the environment. Therefore, it is crucial to understand the fate and transport of NPs in different types of media.

There are many factors that can affect the transport of NPs in porous media. They include the size, concentration, and shape of NPs [25-27]; NPs surface coating with surfactants and/or polymers [6, 28]; fluid flow velocity [29]; solution chemistry (i.e., ionic strength, pH, and ion type) [30]. Darlington and co-workers examined the transport of Al_2O_3 NPs in soil and sand matrices [26]. It was reported that the transport of NPs depended on the size of the agglomerated NPs. Lecoanet and Wiesner evaluated fullerene and oxide nanoparticle mobility in porous media with different flow rates [25]. For particles with larger diameters (>100 nm), slower flow rates resulted in more retention with a later breakthrough curve and a smaller plateau value after full breakthrough when other conditions are kept constant. Alaskar et al. indicated that Ag nanowires were trapped at the inlet of (the core) Berea sandstone and could not go through it [27]. With the same suface characteristics, Ag nanospheres could propagate with 25% recovery. The physical size of NPs could lead to their retention in porous media.

Additionally, Godinez and Darnault investigated the aggregation and transport of TiO_2 NPs in saturated porous media [28]. It was concluded that the mobility of TiO_2 NPs was limited due to the reduction of electrostatic interaction when the solution pH reached the pHpzc (point of zero charge) of NPs. But, the presence of non-ionic surfactant (Triton X-100) improved the transport of NPs by the steric effect. Kadhum et al. used binary polymer system to improve the overall transport of purified multi-walled carbon nanotube (P-MWCNT) in porous media under high ionic conditions [6]. The presence of polymer

leads to the generation of the stable dispersion of P-MWCNT and decrease the adsorption onto sandstone of polymer-coated NPs.

Besides, Jeong and Kim visualized the aggregation of copper oxide NPs during propagation in porous media [29]. The transport of NPs indicated that the higher the Darcy flow velocity, the less they deposited within the medium, and the more the CuO NPs discharged from the porous medium. In the presence of surfactant, most of CuO NPs could propagate through the porous medium, while only 30% of NPs in water flowed through the medium.

Moreover, French et al. evaluated the influence of ionic strength, pH and cation valence on the aggregation kinetics of TiO_2 NPs in aqueous solution [30]. NPs were found to form stable aggregates at pH~4.5 in NaCl suspension. Increasing the ionic strength caused longer times for creating of micro-sized aggregates in the constant pH solution. At other pH values tested (5.8-8.2), TiO_2 NPs formed a micro-sized aggregate quickly, even though the solution was held at low ionic strength. Experimental data also indicated that divalent cations could accelerate the aggregation of TiO_2 NPs in solid and surface water.

Carbon nanotubes (CNTs) are rather commonly used NPs in research and applications [31, 32]. CNTs are allotropes of carbon in a cylindrical nanostructure with a high length-to-diameter ratio [33]. The properties of CNTs suggest that they can find in many technologies, especially in creating new materials with extraordinary strength, and unique electrical and thermal properties. Jaisi and co-workers investigated the transport behavior of single-walled carbon nanotubes (SWCNTs) in a well-characterized saturated porous medium [34]. A laboratory-scale column packed with cleaned quartz sand was used to evaluate the retention of SWCNTs under a wide range of repulsive electrostatic

conditions. Results showed that the mobility of SWCNTs is effectively limited by their irregular shape and high aspect ratio. Furthermore, the effect of KCl concentration in a dispersion of carboxyl functionalized SWCNT on their transport through water-saturated columns was systematically studied. More SWCNTs were retained with a higher KCl concentration, because higher ionic strength in the solution weakened the electrostatic repulsion between nanotubes and the porous medium. So, it was easier for nanotubes to be adsorbed onto the solid surface. Moreover, Kasel et al. investigated the transport and retention of multi-walled carbon nanotubes (MWCNTs) in saturated porous media for different input concentrations and sand grain sizes [35]. Experimental results proved that normalized MWCNT transport increased with higher input concentrations and in coarser textured sand. The retention profiles showed that the majority of MWCNT retention occurred near the surface of the porous medium.

In another study, the DLVO theory and a colloid transport model were used to simulate the fate and the transport of silver NP and CNTs in the sand columns [36]. The DLVO theory worked well with silver NPs, but failed to represent the interactions between CNTs and sand media. Theories and models of colloid transport in porous media may be applicable to describe the fate and behavior of NPs under certain circumstances. In addition, Pham and Papavassiliou numerically studied the NPs transport in heterogeneous porous media with particle tracking methods [37]. It was found that NPs breakthrough curves did not present a plateau unless the pore surfaces were completely saturated. Furthermore, the heterogeneity of the mineralogical surfaces could disturb the transport of NPs depending on the physicochemical properties of the surfaces. In the microscopic scale, the transport of iron NPs, their interaction with the porous media and their

deposition on the aquifer material have been simulated by using commercial software (COMSOL Multiphysics 4.2a) [38]. These simulations have been carried out with a Langrangian approach. This study considered the effect of the relevant forces acting on a single particle such as drag, Brownian, gravity, Van der Waals and electric double layer forces. Because of the limitations associated with the time step interval, trajectories of particles could not be computed completely. There were no results from the simulations conducted in the realistic geometry which was obtained from a scanning electron microscope (SEM) image.

1.3. Contributions of this work

The research contributions of this work are summarized as follows:

- ✓ Studied the physical adsorption of PVP polymer on different shape of CNPs. The conformation of polymer molecules on the CNP surface was classified. All of Dissipative Particle Dynamics (DPD) interaction parameters for PVP polymer in water were determined and validated. We also evaluated the shear effect on the stability of CNPs stabilized with PVP, as well as calculated the range of shear rate for each state of CNPs stabilized with PVP in solution.
- ✓ Investigated the adsorption of commercial ionic and non-ionic surfactants on CNT surfaces. All required DPD parameters for the system of surfactant and water were identified by comparing with experimental data. The properties of surfactant micelles on CNT surface and in the bulk phase were quantified. Besides, the influence of temperature and shear rate on the adsorption of surfactants on CNTs was explored.
- ✓ Examined the adsorption of sodium dodecyl sulfate (SDS) surfactant inside different sizes of single-walled, arm-chair CNTs. The effect of surfactant on the properties of

water (diffusivity, density and residence time) inside SWCNTs was determined. Depending on the concentration of surfactant, SDS inside SWCNT was found to accumulate from 1% to 13% of the total of adsorbed surfactant, and the adsorbed molecules self-assemble in hemi-micellar and random formations.

- ✓ Calculated the propagation of spherical and cylindrical NPs in sphere-packed porous media. Hydrodynamic forces acting on NPs and the trajectory of the NPs were recorded. The orientation of NPs in porous media was determined in both Lagrangian particle tracking (LPT) and DPD simulation.

Chapter 2. Simulation Methods

2.1. Dissipative Particle Dynamics (DPD)

Dissipative Particle Dynamics (DPD) is a coarse grained technique in mesoscopic scale simulation. It is a variant of classical molecular dynamics that employs soft, short-ranged conservative forces, as well as dissipative and impulsive forces, chosen in such a way that the simulated system samples the canonical ensemble. In statistical mechanics, canonical ensemble is the statistical ensemble that represents the possible states of a mechanical system in thermal equilibrium with a heat bath [39]. In other words, it can be considered as an assembly of systems closed to others by rigid, diathermal, impermeable walls.

In the mesoscopic scale, DPD is an attractive method to study complex systems including polymers [40-42], surfactants [8, 43, 44], nanotube-polymer composites [45, 46], colloid particles [47] etc. It was introduced by Hoogerbrugge and Koelman in 1992 [48] and has since received substantial theoretical reports. A group of atoms are lumped together in DPD simulations, so that the computional time is reduced, allowing for the case of large simulation boxes relative to MD simulations.

The DPD system consists of a set of interacting particles, governed by Newton's equations of motion – for a simple DPD particle I,

$$\frac{d\mathbf{r_i}}{dt} = \mathbf{v_i} \tag{2.1}$$

$$\frac{d\mathbf{v_i}}{dt} = \mathbf{f_i} = \sum_{j \neq i} \left(\mathbf{F_{ij}^C} + \mathbf{F_{ij}^D} + \mathbf{F_{ij}^R} \right) \tag{2.2}$$

where $\mathbf{r_i}$ and $\mathbf{v_i}$ are the position and velocity vectors of particle i, $\mathbf{f_i}$ is the interparticle force on particle i by all of the other particles (except itself).

The interaction forces can be represented as the sum of three forces: conservative

(repulsion) $\mathbf{F^C_{ij}}$, dissipative $\mathbf{F^D_{ij}}$ and random force $\mathbf{F^R_{ij}}$ [49], as follows:

$$\mathbf{F_{ij} = F^C_{ij} + F^D_{ij} + F^R_{ij}} \tag{2.3}$$

The conservative force $\mathbf{F^C_{ij}}$ is a soft repulsion acting along the line of centers and is given by

$$\mathbf{F_{ij}^C} = \begin{cases} a_{ij}\left(1 - \frac{r_{ij}}{r_c}\right)\widehat{\mathbf{r_{ij}}} & , (r_{ij} < r_c) \\ 0 & , (r_{ij} \geq r_c) \end{cases} \tag{2.4}$$

where a_{ij} is a maximum repulsion between particles i and j, and $\mathbf{r_{ij}} = \mathbf{r_i} - \mathbf{r_j}$, $r_{ij} = |\mathbf{r_{ij}}|$, $\widehat{\boldsymbol{r_{ij}}} = \boldsymbol{r_{ij}}/|\mathbf{r_{ij}}|$; r_c is the cut-off radius.

The dissipative or drag force, $\mathbf{F^D_{ij}}$, on particle i by particle j, is given by

$$\mathbf{F_{ij}^D} = -\gamma w^D(r_{ij})(\widehat{\mathbf{r_{ij}}}.\mathbf{v_{ij}})\widehat{\mathbf{r_{ij}}} \tag{2.5}$$

where w^D is an r-dependent weight function vanishing for $r > r_C$,$\mathbf{v_{ij}} = \mathbf{v_i} - \mathbf{v_j}$, γ is a coefficient that controls the extent of dissipation in a simulation time step. The negative sign in front of γ indicates that the dissipative force is opposite to the relative velocity $\mathbf{v_{ij}}$. The dissipative force, acting against the particle motion, would reduce the kinetic energy of the system. This is compensated by the random force:

$$\mathbf{F_{ij}^R} = \sigma w^R(r_{ij})\xi_{ij}\widehat{\mathbf{r_{ij}}} \tag{2.6}$$

where w^R is also an r-dependent weight function vanishing for $r > r_c$ and ξ_{ij} is a Gaussian variable with zero mean and variance equal to Δt^{-1}, where Δt is the time step, and σ is a coefficient characterizing the strength of the random forces. These forces also act along the line of centers.

Espanol and Warren [49] showed that either of the two weight functions appearing in equation (2.5) and (2.6) can be chosen arbitrarily; the other weight function is determined by

$$w^D(r) = [w^R(r)]^2 \quad (2.7)$$

$$\sigma^2 = 2\gamma k_B T \quad (2.8)$$

where: k_BT is the Boltzmann temperature of the system. This is analogous to the fluctuation-dissipation theorem for the system [50], and ensures that the kinetic energy of the system is kept in check. Taking k_BT as the unit of energy, we have

$$\sigma^2 = 2\gamma \quad (2.9)$$

We use the standard quadratic function

$$w^D(r_{ij}) = \begin{cases} (1 - r_{ij})^2, & (r_{ij} < r_c) \\ 0, & (r_{ij} \geq r_c) \end{cases} \quad (2.10)$$

The dynamic of the system is obtained by integrating Newton's equations of motion. Here, we use the velocity-Verlet algorithm [51]. It has been proven that DPD maintains the correct hydrodynamic properties of a system because $\mathbf{F}^C_{ij}$, $\mathbf{F}^D_{ij}$ and $\mathbf{F}^R_{ij}$ forces conserve momentum locally [49, 52]. All DPD simulations in this thesis were carried out using the open-source LAMMPS software package [53].

In DPD algorithm, the conservative force is considered as an entirely repulsive force. It is required to have a suitable value for the repulsive parameter (a_{ij}) between the same and different beads. When beads i and j are the same substance (intra-species), the repulsive interaction parameter is obtained from the compressibility parameter [52].

$$a_{ii} = 75 k_B T/\rho \quad (2.11)$$

where: ρ is the number density of DPD fluid. When beads i and j are different substance (inter-species), Groot and Warren proved that the Flory-Huggins theory can be applied to determine a_{ij} between water and polymer [52]. For ρ=3, the Flory-Huggins parameter (χ) is calculated as follows:

$$\chi \approx 0.286\left(\mathrm{a}_{ij} - \mathrm{a}_{ii}\right) \tag{2.12}$$

$$\chi_{AB} = \frac{V_b}{k_B T}(\delta_A - \delta_B)^2 \tag{2.13}$$

where A, B indices are water and polymer beads; δ is solubility parameter; and V_b is the volume of a DPD bead.

However, the Schmidt number of a typical DPD fluid has been reported to be three orders of magnitude less than a real fluid, such as water. Several efforts have been proposed to increase the Schmidt number, such as increasing the cut-off radius, decreasing the temperature and/or increasing γ and using a different thermostat for the system [52, 54].

2.2. Lagrangian Particle Tracking (LPT)

This method involves following and tracking the trajectory of particles in the Lagrangian framework when they travel in a certain flow field. The basic idea of LPT is to determine the position of a particle at each time step by the multiplication of particle velocity and time increment. Fundamentally, the particle acceleration and velocity will be calculated if some specified forces acting on the rest of particle are known. For cylidrical NP, velocity of particles is determined by solving Newton's equation of motion with the effect of total hydrodynamic forces (F_{total}) acting on particle:

$$m\frac{dv_p}{dt} = F_{total} = F_R + F_{drag} + F_g \tag{2.14}$$

where: m is mass of particle, v_p is velocity of particle, t is time, F_R, F_{drag} and F_g represent random force, force due to the pressure gradient in the fluid, drag force and gravity-buoyancy force, respectively.

With white noise correlation, random force is computed as follows [55]:

$$F_R = \sqrt{\frac{12\pi kTa\mu}{\Delta t}}\xi \tag{2.15}$$

$$a = \frac{L}{2\ln\left(2L/d\right)}$$

where: L and d are length and diameter of the cylindrical particle, k is Boltmannz constant, T is temperature, Δt is time step, ξ is random number and μ is viscosity of fluid. In addition, the drag force is generally expressed over the entire Reynolds number spectra as [56]:

$$F_{drag} = 0.5C_D\rho_f S_{eff}\left|u - v_p\right|\left(u - v_p\right) \tag{2.16}$$

where: S_{eff} is particle area normal to the direction of the drag force. It depends on the incidence angle (α) between relative velocity $\left(\vec{u} - \vec{v}_p\right)$and particle major axis direction, and is determined by: $S_{eff} = \pi\frac{d^2}{4}\sqrt{\cos^2\alpha + \left(4\beta/\pi\right)^2\sin^2\alpha}$ where β is aspect ratio (length/diameter).

Drag coefficient (C_D) is determined by the method of Ganser [57].

$$C_D = \frac{24}{\mathrm{Re}\,K_1}\left[1 + 0.1118\left(\mathrm{Re}\,K_1K_2\right)^{0.6567}\right] + \frac{0.4305K_2}{1 + 3305/\left(\mathrm{Re}\,K_1K_2\right)} \tag{2.17}$$

where, coefficient $K_1 = \left(d_n/(3d) + 2/(3\Theta^{0.5})\right)^{-1}$; coefficient $K_2 = 10^{1.8148\left(-\log\Theta\right)^{0.5743}}$; d_n is the equal projected area circle diameter; Θ is particle sphericity and can be calculated as $\Theta = s/S$, s is the surface of a sphere having the same volume as the particle and S is the actual surface area of the cylindrical particle.

Additionally, gravity and buoyancy forces are computed as follows:

$$F_g = mV(\rho_p - \rho_f) \tag{2.18}$$

where V is volume of particle and ρ_p is density of particle.

Besides, particles simultaneously rotate during movement because of the non-coincident center of mass and center of pressure, and the resistance on a rotating body. So, it is necessary to find the angular velocity of particle (w_x, w_y, w_z) in order to obtain incidence angle (α) by solving system of rotation equations as follows [56]:

$$\begin{aligned} I_x \frac{dw_x}{dt} - w_y w_z (I_y - I_z) &= T_x \\ I_y \frac{dw_y}{dt} - w_z w_x (I_z - I_x) &= T_y \\ I_z \frac{dw_z}{dt} - w_x w_y (I_x - I_y) &= T_z \end{aligned} \tag{2.19}$$

where: I_x, I_y, I_z are moments of inertia with respect to the particle axes; and T_x, T_y, T_z are torques acting on particles.

Chapter 3. Interaction of Carbon nanotubes and water

3.1. Introduction [*]

Recently, Dissipative Particle Dynamics (DPD) techniques found increasing use for simulating systems in the meso-scale. They have been used to investigate the behavior of CNT particles in many applications, such as self-assembly of surfactants around CNTs [8, 43, 44] and nanotube-polymer composites [45]. The advantages of DPD are that longer length and time scales are utilized than when employing Molecular Dynamics (MD) methods, while the correct hydrodynamic behavior of the system can be maintained [58]. The main idea is to group several molecules together into a lumped particle interacting with others in a soft and short-ranged potential, as described in Chapter 2. The computational cost in DPD simulations is lower than MD simulations, when simulating the same system. This fact gives an opportunity to handle large systems that could not be feasible to treat with MD modeling. When comparing to other meso-scopic methods, the problem with isotropy and Galilean invariance of the lattice-gas automata (LGA) method is not encountered in DPD simulations [59]. In addition, mass and momentum conservation, which are not maintained in Brownian Dynamics Simulations (BDS), are valid in the DPD method [59]. Moreover, DPD is a good method to tackle problems associated with complex flow structures [60]. A solid phase present in the system can be created by using a set of frozen DPD particles on the surface with an appropriate choice of interaction parameters to obtain the desired surface properties.

The characteristics of a DPD fluid depend on the chosen values of the interaction

[*] Material in this chapter has been published in Minh Vo, Dimitrios V. Papavassiliou, 2016, Molecular Simulation, 42, 9, p737-744.

parameters, such as the repulsion (a_{ij}), dissipation (γ), and random noise (σ) constants that appear in the DPD model equations. These parameters control the interaction potential and the motion of each DPD bead at each time step. Hence, an appropriate choice of parameters is needed to ensure that the DPD beads represent the system that is simulated. A good practice to select DPD parameters is to compare properties of the simulated system with values from experiments or other validated simulations. For CNT and water interaction, Calvaresi et al. used a repulsion parameter a_{ij} equal to 80 for CNT and water interactions to study the morphology of CNTs and surfactants in an aqueous environment [8]. Arai et al. classified CNT surfaces based on the properties of chemical interactions between water and CNT [43]. Then, they suggested that the value of the repulsion parameter was 70, 50 and 25 for hydrophobic, hydro-neutral and hydrophilic surfaces, respectively. These studies indicate that there are different suggestions for CNT and water interactions in DPD simulations, while values that can be used to simulate a range of scales are needed.

In this chapter, we calculate the hydrodynamic properties of SWCNTs in the case of water flowing past arrays of SWCNT to identify the DPD interaction parameters that are suitable for a system of CNTs and water. Then, the ability of scaling up in DPD is also investigated.

3.2. Background and methods

a. Computational details

The conditions of the validation simulations were as follows: for water, the number density (ρ) was chosen to be 3 and five water molecules (N_m=5) were grouped into 1 water bead. Water beads were randomly distributed in the simulation box at the

initial step but did not penetrate into the SWCNT particle. The initial velocities of all water particles were set randomly according to the system temperature. The SWCNT was modeled as a rigid hollow cylindrical particle. Theoretically, all beads in the DPD method have the same volume. To satisfy this assumption, 24 carbon atoms of a SWCNT with chirality (32,0) and with diameter of 2.5 nm and length of 2.1 nm were grouped together [61]. In our simulation, the SWCNT particle is stationary and treated as a rigid body. Hence, there is no need to have an interaction between CNT beads, such as a bond or an angle potential. The important point we want to quantify in this study is the interaction between water beads and CNT beads.

The simulation conditions were kept similar to the conditions in Walther et al. [62]. A SWCNT was placed at the center of the computational box of dimensions 16.4x16.4x2.1 (L_x x L_y x L_z) nm^3. The onset water flow was perpendicular to the SWCNT and different flow velocities were set to achieve different values of the Reynolds number (*Re*). It was ensured that the velocity was lower than 1.2 so that the incompressible flow condition (low Mach number) was not violated (the speed of sound is around 4 in our simulations [63]). Periodic boundary conditions were imposed in the three space directions. The total number of beads was 7067 in a computational domain that included 6869 water and 198 CNT beads. All simulations were performed in the constant number of molecules and constant volume and temperature (NVT) ensemble, which preserves hydrodynamics properties [52]. Additionally, all the simulations were carried out for at least 5×10^6 steps with a time step of 0.01.

In order to maintain accurately the thermodynamic behavior of the system, the DPD method has to satisfy the fluctuation-dissipation theorem [64]. This means that the

dissipative parameter (γ) should be proportional to the noise parameter (σ). It is recommended that σ should be equal to 3 for maintaining stability of the system, as well as reaching temperature equilibrium quickly [52]. Therefore, we can determine the value of the dissipative parameter as $\gamma = \sigma^2/2 = 4.5$. For the same type of bead, the repulsion parameter (a_{ii}) is chosen by the following equation [52]:

$$\boldsymbol{a_{ii} = \frac{75 k_B T}{\rho} = 25} \tag{3.1}$$

The repulsion parameter (a_{ij}) between the carbon of the CNTs and water was determined by comparing the hydrodynamic properties with results from MD simulations. Furthermore, the interaction range (r_c, i.e., the cut-off distance) for CNT-CNT and CNT-water interactions was set to 1, while r_c among fluid beads was chosen as 1.3, in order to increase the viscosity of the DPD fluid. Setting a higher value of the cut-off distance would require higher flow velocity in order to reach the *Re* used in the Walther et al. study [62]. In that case, the incompressible flow condition would not be satisfied, because the Mach number would be larger than 0.3.

In DPD simulations, all values are dimensionless for simplicity. The bead mass and the temperature are set to units of mass and energy (m= $k_B T$= 1). The length scale (L) and the time scale (t) of the DPD system are determined by matching the density and viscosity of the fluid to that of water [65], respectively. While the time scale can be obtained by other physical properties, we chose to match the viscosity of water in order to obtain the time scale, because water flow is of interest herein, and the hydrodynamic properties of the SWCNT would be affected by the viscosity of water. Additionally, Fuchslin et al. have showed that the interaction parameters will be scale-free at arbitrary

scales, if length and time scales are appropriately chosen [66]. The physical units of the performed simulations can be obtained by using the length, mass and time scales as those are presented in Table 3.1. Since density and viscosity of water were used to determine the length and time scales of our simulations at different N_m, the density and viscosity of the DPD fluid were kept constant as 998.2 kg/m^3 and 1.01x10^{-6} m^2/s, respectively, as coarse graining changed. For diffusivity, it also remained constant (7.91x10^{-8} m^2/s) with increasing N_m. This value is larger than the experimentally obtained diffusivity for water (2.43 x10^{-9} m^2/s). The diffusivity of DPD particles was calculated from averaging the mean square displacement with respect to time. An increased diffusion with DPD has been observed in other studies [67, 68], because each DPD particle represents several water molecules. In addition, the soft-core potential employed by DPD results in higher diffusivity, since hard collisions that can impede molecule motion is softened.

Table 3.1. DPD scales converted into physical units. They are length scale (L), time scale (t) and mass scale (m).

N_m	L (nm)	t (ps)	m (kg)
5	0.766	0.926	1.496 x 10^{-25}
10	0.965	1.461	2.992 x 10^{-25}
273	2.497	13.243	8.167 x 10^{-24}

b. Hydrodynamic behavior of a SWCNT in flow

One of the most remarkable findings with MD [62] is that in the case of water flowing past SWCNTs, the drag coefficient can be calculated with the well-known Stokes-Oseen equation that applies to macroscopic systems. [In fluid dynamics, the drag coefficient (C_d) is a dimensionless parameters that quantifies the resistance of an object

in a fluid environment]. For an array of infinite cylinders, the Stokes-Oseen approximation for the drag coefficient is calculated as follows [69]:

$$C_d = C_d^{cc} \frac{3+2\emptyset^{5/3}}{3-4.5\emptyset^{1/3}+4.5\emptyset^{5/3}-3\emptyset^2} \quad (3.2)$$

where $\emptyset$ is the fraction of the volume occupied by the carbon nanotube in the computational box ($\emptyset = \frac{\pi R^2}{L_x L_y}$), and C_d^{cc} is the drag coefficient on a single circular cylinder given by [70]

$$C_d^{cc} = \frac{8\pi}{Re\ ln(7.4/Re)} \quad (3.3)$$

In the above equation, *Re* is the Reynolds number defined on the basis of onset flow velocity of the fluid (*U*) and the diameter of the SWCNT (*D*). The drag coefficient from the DPD simulation is computed by

$$C_d^{DPD} = \frac{F_x}{0.5\rho U^2 L_z D} \quad (3.4)$$

where F_x is the stream-wise component of the force acting on the cylinder.

In order to obtain the correct properties of the simulated system, the hydrophobic character of a SWCNT should be preserved in the DPD simulations. The slip length of the water as it flows over the SWCNT should then be accurately predicted through the DPD simulations. The slip length of the water on the SWCNT surface was obtained by fitting the tangential fluid velocity profile to the Stokes velocity field around a single circular cylinder [70],

$$v_t = a \ln\left(\frac{r}{R}\right) + b + c\left(\frac{R^2}{r^2}\right)$$

(3.5)

where *a*, *b* and *c* are the parameters of the fit curve, *R* is the radius of the SWCNT, and *r* is distance from the center axis of the SWCNT. When all parameters from the fit curve are known, the slip length on the CNT-water interface was computed as follows [70]:

$$L_s = R(b + c)/(a - 2c)$$

(3.6)

3.3. Results and discussion

a. Effect of repulsion parameter on the drag coefficient and slip length

In our simulation, a constant force was applied on all water beads to generate a specified flow *Re,* while the SWCNT beads were kept stationary at the center of the simulation box. All properties of system were determined by taking time averages after equilibrium was reached.

The drag coefficient (C_d) and the slip length (L_s) of SWCNT depend on the interaction between carbon atoms on the SWCNT surface and water molecules moving around its surface. In Table 3.2, we investigated the effect of the repulsion parameter between the carbon of the CNT and water ($a_{\text{CNT-water}}$) on C_d and L_s at Re = 0.137. The drag coefficients were computed using Equation 3.4 and the time average of the total wall force exerted on the CNT surface in the x-direction (the flow direction). This force depended on the interaction potential between water and CNT. It is shown in Table 3.2 that C_d decreases with increasing $a_{\text{CNT-water}}$. At high values of $a_{\text{CNT-water}}$, it is difficult for water beads to move close to the CNT beads, causing a smaller force to act on the CNT

and a drag coefficient that is smaller. This is an effect that indicates a hydrophobic surface – the hydrophobicity of the CNT surface depends on $a_{\text{CNT-water}}$. At higher value of $a_{\text{CNT-water}}$, the CNT surface gets more hydrophobic. Ou et al. [71] proved that hydrophobic surfaces lead to drag reduction.

Table 3.2. Effect of repulsion parameter ($a_{\text{CNT-water}}$) on drag coefficient (C_d) and slip length (L_s) for $N_m = 5$ at $Re = 0.137$.

$a_{\text{CNT-water}}$	C_d	L_s (nm)
50	83.84	0.47
60	79.29	0.48
70	67.04	0.51
80	67.61	0.57
90	68.76	0.57

The tangential velocity profile of water around the CNT at different values of $a_{\text{CNT-water}}$ is used to determine the slip length (L_s) on the SWCNT surface via Equation 3.5. All constants (a, b and c) in this equation are obtained by fitting the tangential velocity profile with the Stokes solution presented in Equation 3.4, as presented in Figure 3.1. It is seen in Table 3.2 that L_s becomes larger when $a_{\text{CNT-water}}$ increases. The dependence of L_s on $a_{\text{CNT-water}}$ is similar to the dependence of C_d on $a_{\text{CNT-water}}$. The slip of water particles on CNT originates on the hydrophobicity of its surface, and the CNT surface repels water stronger at the higher value of $a_{\text{CNT-water}}$. This effect is also observed in MD simulations [72] for hydrophobic surfaces. Therefore, the trends of C_d and L_s at different $a_{\text{CNT-water}}$ from DPD calculations are consistent with previous works.

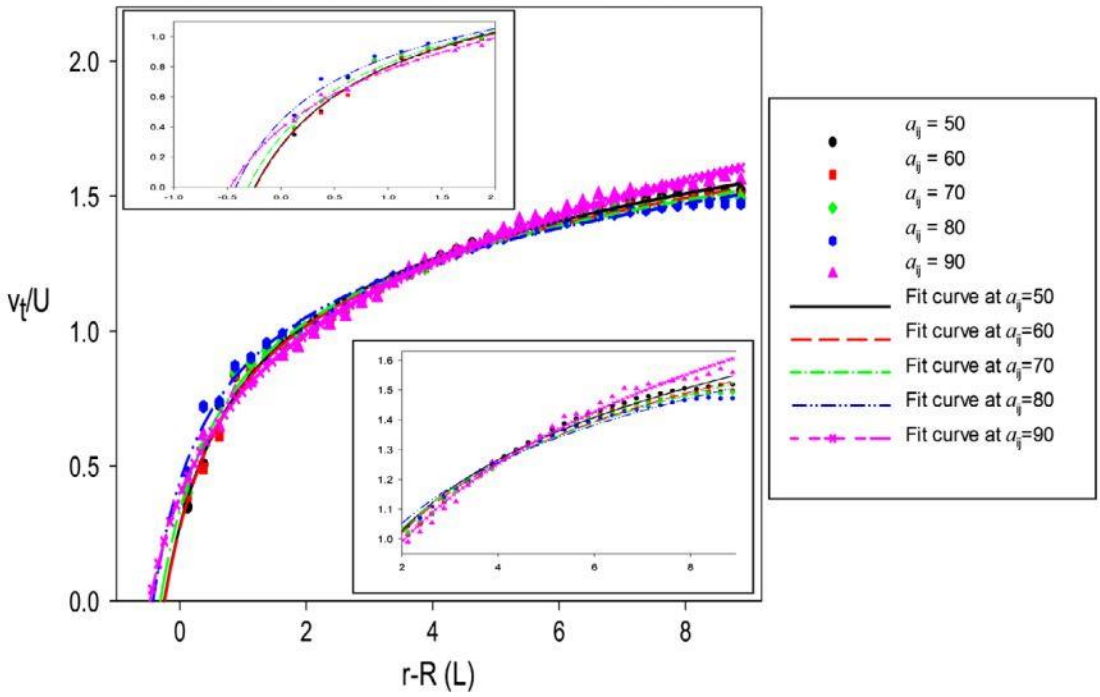

Figure 3.1. The tangential velocity profile and its curve fit with the analytical solution for flow of water flow past an array of CNT at different values of repulsion parameter ($a_{\text{CNT-water}}$). The top left and bottom right inset figures exhibit the enlarged parts of the tangential velocity with respect to distance (r-R) from -1 to 2 and from 2 to 9, respectively.

In MD simulations, Walther and co-workers determined that C_d and L_s are around 76 and 0.49 nm [62] in the same conditions as our simulations. It is seen that the deviation of C_d and L_s between the DPD method and MD simulations is smallest at $a_{\text{CNT-water}}$ = 60. In addition, the magnitude of the first peak of the average radial density profile (Figure 3.2) at a_{ij} = 60 is also fairly similar to the results of Walther et al. [62]. At this peak, the density of water is nearly 3 times the bulk density of water. This phenomenon is also observed in MD and DPD simulations for water [73]. Regarding the fluid density fluctuation, Pivkin and Karniadakis have suggested that this problem can be alleviated by using the ABC's approach (adaptive boundary conditions) [74]. Another approach is to use stochastic boundary forcing to decrease the liquid density fluctuations close to the surface in DPD simulations [75]. In these studies, a modification in the vicinity of surface was applied to

avoid density fluctuations and to obtain the no slip boundary condition. In this way, however, the surface was forced to behave as hydrophilic (or, more accurately, to exhibit $L_s = 0$). Even though the density of water in the region close to the SWCNT surface is higher than in the bulk phase, the drag coefficient from our calculations is similar to the Stokes-Oseen solution, as was observed in the MD simulations [62]. Furthermore, the drag coefficient from the DPD simulations is in good agreement with theoretical solutions obtained in previous studies without using any modification to reduce the density fluctuation [60, 76, 77]. Since the objective of this work is to obtain both the slip length and the drag coefficient for SWCNTs in water, we think that the density profile in our results is acceptable. Therefore, we chose $a_{ij} = 60$ for the rest of the simulations.

Table 3.3. Drag coefficient (C_d) and slip length (L_s) of SWCNT at different *Re* when N_m=5.

Re	C_d from Stokes-Oseen solution	C_d from DPD	L_s (nm) [62]	L_s from DPD (nm)
0.137	76	79.29	0.49	0.48
0.274	46	41.43	0.27	0.29
0.548	29	25.79	0.28	0.26

The effect of *Re* on C_d and L_s is presented in Table 3.3. Both C_d and L_s decrease as the *Re* of water flow increases. The drag coefficient for water flowing over an array of cylinders is very similar to the macroscopic Stokes-Oseen solution. The deviation of C_d between DPD results and the Stokes-Oseen approximation is about 10% at different velocities of flow. These results seem to be better than calculations from MD simulations. For the slip length, results by MD simulation [62] and slip length from DPD are in good agreement.

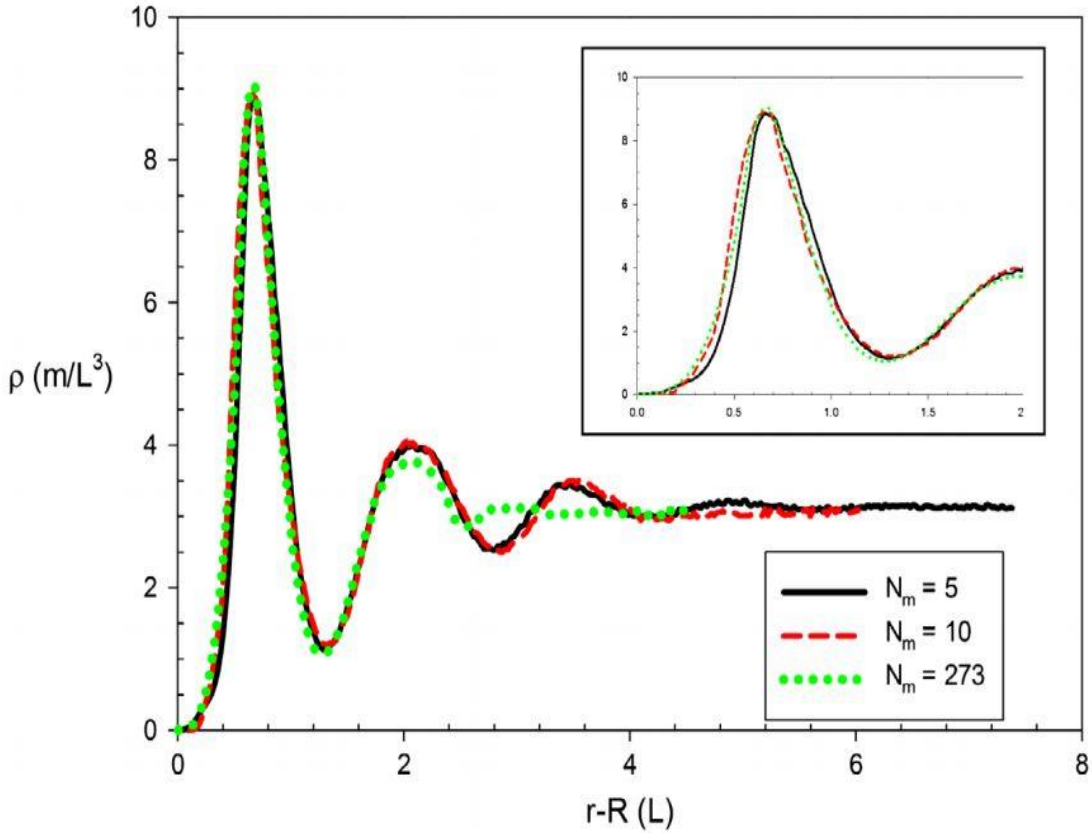

Figure 3.2. Average radial density profile of water at $a_{CNT\text{-}water}$=60 at different length scales. The inset figure displays the enlarged parts of the density profile from 0 to 2.

In addition, the effect of periodicity in the computational conditions and the effect of slip length anisotropy are also studied. The flow direction in these cases is illustrated in Figure 3.3. The axis of the CNT is on the *xz* plane. For examining the effect of the flow periodicity, we simulated a case where the flow of water is set at an angle of 17^o with the x axis (case A). For examining slip length anisotropy of flow around a CNT, we simulated the case of flow at an angle between the flow direction and the x and z axes at 45^o (case B). In MD simulations, Walther et al. [62] found a very interesting result that the periodicity effect can be neglected in case A, while there is considerable slip length difference for flow along the axis of the CNT and across the axis of the CNT in case B. The slip length in the r-z plane was apparently more than 35 times the CNT diameter and

220 times the slip length in the x-y plane in case B (r is the radial direction of the CNT).

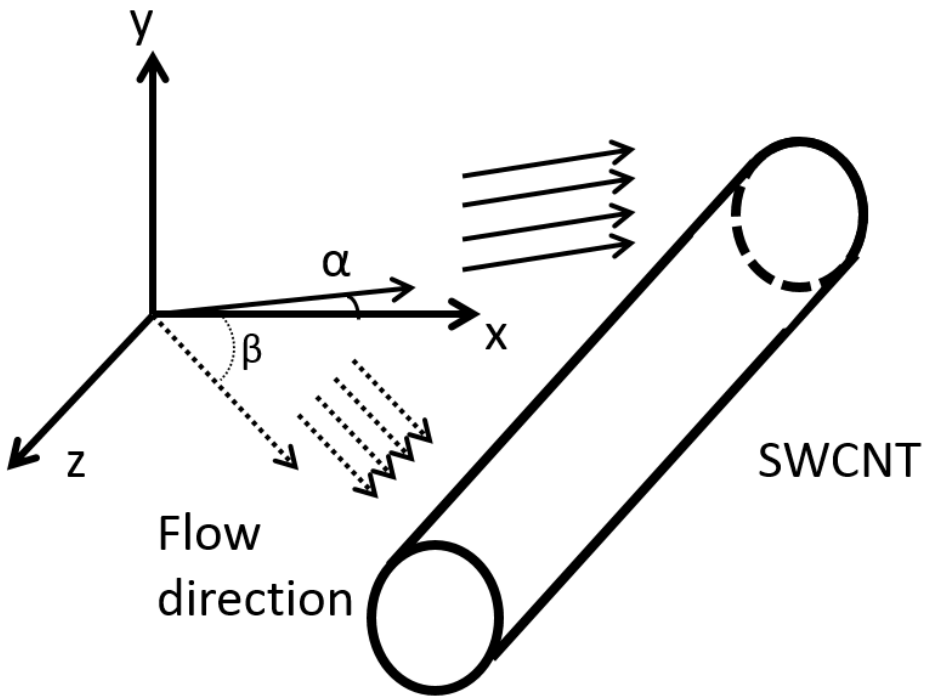

Figure 3.3. Flow direction for simulations designed to examine periodicity effects (green arrows - case A) and anisotropic slip length (red arrows – case B) study. In case A, the angle between the flow direction and the x axis is 17°. In case B, the water flow is slanted along x and z axis with an angle (β) of 45°. The axis on the SWCNT is on the xz plane, parallel to z.

Results in Table 3.4 indicate that the influence of the periodic boundary condition and the slip length anisotropy of SWCNT are also reproduced from DPD calculation. In case A, the drag coefficient and the slip length are nearly similar to the case when the direction of the flow is parallel to the x axis at *Re*=0.274, presented in Table 3.3. This indicates that the calculations for the slip length are not an artifact of the computational box periodicity. In case B, the finding that there is anisotropy in the slip length over a SWCNT is also observed with DPD simulations. Even though the slip length in the r-z plane in DPD is smaller than in MD simulations, the difference between slip length in r-z and x-y plane from DPD is also very large. This is an important point of agreement

between MD and DPD simulations with respect to slip length anisotropy. In other words, it is observed that the hydrodynamic properties of SWCNT are completely recovered with the DPD method.

Table 3.4. Drag coefficient (C_d) and slip length (L_s) of SWCNT (Re=0.274) at N_m=5 for case A and case B.

	Case A		Case B		
	C_d	L_s (nm)	C_d	L_s (nm) in x-y plane	L_s (nm) in r-z plane
Nm = 5	40.85	0.30	42.35	0.31	57.51
MD simulation	46	0.33	46	0.40	88

b. The effect of length scale in DPD simulation

The advantage of DPD as a coarse graining technique is that the length scale of the simulation can increase by changing the number of molecules (N_m) grouped into one bead. With a specified system, the use of higher N_m can save time and computational cost. About coarse-graining level, Pivkin et al. suggested that there might be numerical effects when increasing N_m up to 20, (e.g., solidification of the DPD liquid, compressibility effects and geometry constraints [78]). Similarly, Travimof pointed out that the limitation of N_m is 10 [79]. The reason for these findings is the assumption of a linear scaling relation of the repulsion parameter (a_{ij}) with N_m. In those studies, a higher value of a_{ij} was used for higher coarse graining level. Hence, DPD beads exhibited stronger repulsion to each other and created large errors in the radial density function and the hydrodynamic properties of the simulated DPD system. To determine the repulsion parameter, Groot and Warren [52] calculated the compressibility of the DPD system and compared with the compressibility of water at room temperature (300K). Then, the repulsion parameter

(a_{ii}) was determined (see Equation 2.11 above). It only depended on temperature and density. In later work, Groot and Rabone [67] reported that the conservative forces in DPD should scale linearly with the coarse graining level. In general, the DPD system should satisfy the following relation.

$$\frac{1}{k_B T}\left(\frac{\partial P}{\partial \rho}\right)_{simulation} = \frac{N_m}{k_B T}\left(\frac{\partial P}{\partial n}\right)_{experiment}$$

(3.7)

However, Fuchslin et al. [66] argued that the DPD formalism can be valid if one scales the particle interaction cut-off distance appropriately "the DPD formalism is scale-free". In that study, the pressure of a DPD system (obtained from the virial theorem) was computed at different coarse-graining levels. Results in reference [66] indicate that if one uses reduced units in the DPD simulations, which are obtained by scaling the cutoff distance in physical units, then the interaction parameters that scale like energy over length will need to remain constant as the scaling increases, while maintaining system properties. In other words, they argued that a set of DPD interaction parameter values can represent the system at arbitrary length scales. We only increase the scales to N_m =273, because we do not want to have water beads larger than the CNT diameter. Maintaining the same interaction parameters were able to reproduce the properties of a system with different coarse graining levels (N_m). It is an important point to indicate that DPD simulation can work well for the system in meso-scale. Actually, there are several studies [80-82] that use N_m in a wide range (even up to 10^7-10^9), while the hydrodynamic properties of the system are represented correctly.

To investigate the ability of DPD simulations to scale up, the number of water molecules

in one bead was increased while all parameters were kept the same as when N_m = 5. For our system (SWCNT with diameter of 2.5 nm), N_m = 273 was the maximum of water molecules that we were able to group together. At this case (N_m = 273), the length scale of a bead is equal to the diameter of the SWCNT. If the length scale was further increased, the projected area of SWCNT beads and water beads would not be comparable. Hence, N_m = 273 is the upper limit of scaling in our case. All DPD interaction parameters for the system with N_m =5 were used to run the cases of N_m = 10 and N_m = 273. Regarding the geometry of the SWCNT, it was still a hollow cylinder when N_m = 10. However, it becomes a string of connecting spheres (Figure 3.4) as N_m = 273. When the length scale of the system is increased, the amount of DPD beads in the simulation box is also reduced. The total beads in the simulation were 2656 beads (2601 beads of water and 55 of CNT) and 916 beads (903 water and 13 CNT) for N_m = 10 and N_m = 273, respectively.

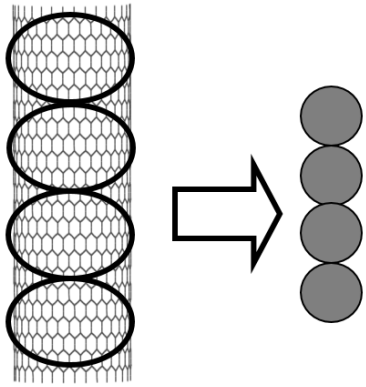

Figure 3.4. The fragmentation of SWCNT into 4 DPD beads when N_m=273. At this scale, a green circle represents a segment of SWCNT in DPD simulation. There are 13 CNT beads that represent the whole SWCNT in the simulation box.

To maintain the incompressible flow condition, the Mach number of the system must be less than 0.3. The isothermal speed of sound (c_s) is about 4 [83]. The maximum Mach number in our system at different length scales is determined by dividing the maximum

velocity in the flow by c_s. Data in Table 3.5 indicate that the incompressibility condition is satisfied in different length scales. Besides, the radial density profiles at N_m=10 and N_m=273 are also drawn in Figure 3.2. The density profiles at different length scales are similar to each other in the position of the first density peak and its magnitude. As the length scale increases, the size of the simulation box is reduced. Hence, the range of density profile seen in the x-axis of Figure 3.2 is smaller when N_m is increased. For N_m = 273, the density profile is nearly constant after the 2nd peak instead of having a 3rd peak, but this is because of the smaller box size in case of N_m=273. It appears that the density profile of the water is quite similar at different coarse graining levels in the simulation.

Table 3.5. Mach number of water flow at different coarse graining levels

N_m	V_{max}	Mach number
5	0.240	0.060
10	0.303	0.076
273	0.711	0.178

Table 3.6. Drag coefficient (C_d) and slip length (L_s) of SWCNT at different *Re* when N_m = 10 and N_m = 273.

	N_m = 10		N_m = 273	
Re	C_d	L_s (nm)	C_d	L_s (nm)
0.137	79.67	0.45	80.10	0.43
0.274	42.15	0.25	41.28	0.22
0.548	26.29	0.25	24.27	0.23

Results for the drag coefficient and the slip length as N_m = 10 and 273 are shown in Table 3.6. These results are comparable with the case of N_m = 5. The value of the drag coefficients and the slip length are almost identical when N_m is equal to 5, 10 and 273, indicating that the hydrodynamic properties of the particle were preserved even though

the length scale of the system was expanded. Additionally, the influence of periodicity and the slip length anisotropy are also examined in the cases of N_m = 10 and 273 in Table 3.7. The drag coefficient and slip length are quite close to these values when Nm is equal to 5. There is no effect of flow periodicity in case (A) while the anisotropic slip length in case (B) is reproduced. The slip length in the x-y plane is quite smaller than the MD results. But the large difference of slip length in r-z and x-y planes is replicated in these longer scales. Therefore, the interaction parameters for CNT and water do not depend on the length scale of DPD simulation system, while the hydrodynamic properties of the SWCNT are maintained.

Table 3.7. Drag coefficient (C_d) and slip length (L_s) of SWCNT (Re=0.274) at N_m = 10 and N_m = 273 for case A and case B.

	Case A		Case B		
	C_d	L_s (nm)	C_d	L_s (nm) in x-y plane	L_s (nm) in r-z plane
Nm = 10	43.20	0.26	39.65	0.25	61.51
Nm = 273	38.90	0.23	40.17	0.21	55.73
MD simulation	46	0.33	46	0.40	88

3.4. Conclusions

The appropriate interaction parameter for CNT and water in DPD simulation was determined by simulating water flowing past an array of SWCNT. Validating the results based on the drag coefficient and the slip length, DPD results showed a good agreement with MD simulations when $a_{\text{CNT-water}}$ is equal to 60. The hydrophobicity of the CNT surface is also demonstrated in DPD simulation. Moreover, we have calculated the hydrodynamics properties of SWCNT at different length scales. It is seen that the correct

hydrodynamic properties and the slip length anisotropy effect of SWCNTs were maintained as the length scale of the system was increased. The scaling up of the DPD simulation is a promising alternative way to study CNTs and their interactions in nano-fluidic environments.

Chapter 4. Polymer coated carbon nanoparticles in aqueous solution

4.1. Introduction [†]

Carbon nanoparticles (CNPs) have received attention for possible use as biosensors and electrodes and for applications in drug delivery, tissue engineering, enhanced oil recovery, composite technology etc. due to their unique optical, magnetic, electronic and chemical properties [84-89]. Generally, the poor solubility of CNPs in an aqueous phase is a major difficulty in handling them for practical use [90]. They are easy to agglomerate in solution due to strong hydrophobic attractions [91]. Obtaining a stable dispersion of nanoparticles is an important step, when they are used as nano-carriers [92]. Polymers have been used to stabilize CNPs by a non-covalent wrapping mechanism [93, 94]. The dispersion of polymer-coated nanoparticles is strongly influenced by their size and shape, polymer molecular weight, the interaction between polymer and nanoparticle, as well as the hydrodynamic forces of the fluid. There is, however, still need for insights that can be gained by theoretical advances and by simulations regarding the factors that govern the physical adsorption of polymers on CNPs.

Various types of CNPs have been investigated intensively for use as drug delivery agents and as nano-carriers [95-98]. In experiments, Ganeshkumar et al. used hollow amphiphilic carbon nano-spheres coated with pH-sensitive polymer as a carrier to deliver oral insulin [99]. It was showed that the interstinal absorption of insulin was improved significantly effectively and the blood glucose level decreased in a diabetic rat model.

[†] Material in this chapter has been published in Minh D. Vo, Dimitrios V. Papavassiliou, Carbon, 2016, 100, p291-301 and Minh D. Vo, Dimitrios V. Papavassiliou, Nanotechnology, 2016, 27, 32, 325709.

Furthermore, both carbon nanotubes and carbon nano-horns were found to be promising candidates for drug delivery with high drug-loading capacity [100, 101]. Moreover, Liu and co-workers functionalized nano-graphene oxide with branched polyethylene glycol for delivery of water insoluble cancer drugs [102]. Their results displayed a feasible way to use graphene for *in vivo* cancer treatment with diverse aromatics and low-solubility drugs. Using MD simulations, Skandani and Al-Haik found that the SWCNT penetrability into the lipid membrane was affected in the presence of polyethylene glycol (PEG) molecules and the PEG chains also decrease the adhesion energy up to 10% in the blood serum [103]. Furthermore, Pham et al. explored the transport and kinetics of nanoparticles (representing polymer-stabilized purified multi-walled carbon nanotubes) in porous media by lattice Boltzmann methods in conjunction with Largangian particle tracking [37, 104, 105]. It was discovered that the diffusivity of the nanoparticles does not depend on the nanoparticle adsorption and desorption nominal rates on the porous media matrix surface, and that nanoparticles with smaller size are retained more than larger ones.

In this chapter, we investigate the effects of the shape of the particle and of the surface curvature on the adsorption of PVP polymer on CNPs of different shapes (such as sphere, cylinder and graphene sheet) under shear, and we quantify the range of shear rate corresponding to each state of PVP adsorption on the nanoparticle. In addition, the arrangement of PVP on the CNP is investigated. The choice of PVP was made since PVP is often used to stabilize suspensions of carbon nanotubes, and because it has the characteristics of a polymer that can be used for such applications. To characterize the conformation of adsorbed PVP molecules, the end-to-end distance (L_e) and the radius of

gyration (R_g) at equilibrium and under shearing forces due to the flow were calculated. These properties could be a signature for the state of PVP adsorption on CNP. Finally, the adsorption and desorption of polymer on a flat hydrophobic surface was studied to identify the threshold shear rate to remove PVP completely from the surface, and to observe differences in the mechanism of polymer desorption from a surface with zero curvature.

4.2. Background and methods

a. Simulation details

The simulations were performed in a periodic cubic box of constant volume V = Lx×Ly×Lz, where Lx, Ly, Lz were the simulation box side lengths. For simplicity, reduced units are used throughout this report. The number density of water is three (ρ=3) in dimensionless units. All simulations were set at constant reduced temperature k_BT=1 (equivalent to 298 K). All DPD calculations were performed in the canonical ensemble (NVT – constant-temperature, constant-volume). The noise amplitude and friction coefficients were set to σ = 3 and γ = 4.5, respectively [52]. Additionally, all the simulations were conducted with a time step of 0.02. Visual molecular dynamics (VMD) software was used to visualize all snapshots presented in this report.

In prior experiments conducted at the University of Oklahoma, PVP with molecular weight of 40,000 g/mol was employed to stabilize CNTs successfully [6, 106, 107]. There were about 360 repeating monomer units in each polymer chain. It was assumed for the present study that the volume of a PVP repeating unit is equal to the volume of monomer N-vinylpyrrolidone. Hence, it was found that the volume of a PVP repeating unit was

176.94Å^3 (nearly equal to the volume of 6 water molecules). In our DPD coarse grained model, each PVP bead was composed of 6 PVP repeating units. Then, every PVP molecule consisted of 60 beads. It follows that 36 water molecules should be grouped to make sure that all DPD beads have the same volume. By scaling this way, the length scale and cut-off distance (r_c) of the DPD simulation was 1.47 nm. The CNT was considered to be a closed-end, rigid hollow cylindrical body. Its diameter and length were $6.8r_c$ and $34r_c$, respectively. Note that the shape of the CNT was kept a cylinder during the whole simulation. It is not needed to have additional bond and angular potential among CNT beads.

Carbon nanoparticles are assumed to be rigid bodies in the simulation and water cannot penetrate into them. For spherical particles we used two different particle sizes, and we designated these two particles as particles S1 and S2. They have diameters of 7.3 and 22 nm, respectively. In simulations, the S1 and S2 particles were considered as hollow spheres. There were 390 and 3604 DPD beads arranged on the spherical surface of the S1 and S2 particles, respectively. The graphene sheet-like particle (designated as particle G) was a single layer of carbon with dimensions of 25.1 x 30.3 nm^2. The G particle was created by 1820 beads in a square lattice arrangement.

The adsorption of polymer on a nanoparticle is related to the surface area of the nanoparticle. In order to study the curvature effect on the adsorption, particles S2 and G had the same surface area for adsorption. Note that the G particle could allow PVP polymer molecules to adsorb on both its sides. All of PVP-coated CNPs were released at the center of the flow field when conducting shear flow simulations.

Furthermore, Maiti and coworkers suggested that the repulsion interaction between CNT

and polymer can also be calculated via Flory-Huggins theory, in the same way as computing a_{ij} of water and polymer [45]. Finally, the interaction parameters between CNT and water beads, a_{ij}, were determined by validating with MD results [108]. Briefly, all repulsive parameters implemented in this work are reported in Table 4.1.

Table 4.1. Repulsion parameters a_{ii} and a_{ij} for water, CNT and PVP beads.

	Water	CNT	PVP
Water	25	60	44.9
CNT		25	34.1
PVP			25

b. The shear flow conditions

Two parallel walls were added at opposite faces of the simulation box in order to generate the shear flow in DPD simulation. Each wall was considered as a rigid region that included three layers parallel to the (xy) plane. Each layer was built in a square lattice with constant nearest neighbor distance in x and y directions ($l=0.5\ r_c$). The distance between two consecutive layers was equal to $0.5r_c$. To avoid the penetration of water into the wall region, the bounce-back reflections were manipulated at the water-wall interface. Besides, the no-slip boundary conditions at the wall were also applied to determine the interaction between water and wall beads [109]. Additionally, the density of the wall was set equal to that of water. It is noted that the presence of two parallel plates was to produce the shear flow. The repulsion parameters of wall and other species were similar to those of water and these other species. Periodic conditions were employed in x and y dimensions. The direction of shear flow was the x direction.

For Couette flow, a force (F_{wx}) was applied to the top wall to move it in x direction, while the bottom wall was kept stationary. The Lees-Edwards boundary condition [110] was

used to prevent the fluctuations of water density and system temperature due to the frozen wall. In this way, a constant shear rate along the z direction was achieved after running around 500,000 simulation steps. The velocity profile (v_x) was proportional to the distance (z) from the two walls (zero at the bottom wall, and maximum at the top wall). The constant shear rate (γ_s) can be calculated from the relation

$$\gamma_s = \left|\frac{dv_x}{dz}\right| \tag{4.1}$$

For Poiseuille flow, a force in the x direction (f_x) was imposed on each water bead to drive the flow. This body force corresponded to the application of a pressure drop along the length Lx of the simulation box. After the flow was fully developed, we obtained a parabolic velocity profile and a linear shear stress profile.

c. Determination of the bond and angle interaction parameters for PVP

First of all, the simulation is required to reproduce the structure of the polymer at equilibrium. In solution, a polymer chain has a continuously varying shape. An instantaneous shape of a polymer chain is called a conformation, which is typically quantified in terms of its radius of gyration (R_g) and end-to-end distance (L_e). The radius of gyration is defined as the root mean square distance of a polymer mass segment from the overall polymer center of mass. The end-to-end distance (L_e) indicates the distance between two ends of a linear polymer chain in a particular conformation. Therefore, we used a freely rotating chain model for the polymer to duplicate this behavior. Both L_e and R_g can be determined in the simulation as follows [111]:

$$L_e = |\boldsymbol{r}_N - \boldsymbol{r}_O| \tag{4.2}$$

$$R_g^2 = \langle \frac{1}{N+1} \sum_{i=0}^{N} (r_i - r_G)^2 \rangle = \frac{1}{N+1} \sum_{i=0}^{N} \langle (r_i - r_G)^2 \rangle \tag{4.3}$$

where N is the number of segments of polymer chain; $\mathbf{r}_i$ is the position of the i^{th} polymer bead; $\mathbf{r}_G$ is the center of mass of the whole polymer chain, and the brackets indicate average for all polymer molecules in the simulation.

We utilized these values (L_e and R_g) in order to determine the appropriate parameters (k_a and k_b) for PVP in water. Kokuoz et al. [112] calculated L_e at different molecular weight of polymer (from 37,000 to 159,000 g/mol) by multiplying the statistical segment length with the square root of the degree of polymerization. In this way, we have L_e of PVP with 40,000 g/mol to be 11.38nm. Additionally, values of R_g of PVP polymer in the range of molecular weight from 55,000 to 360,000 g/mol have been calculated from static light scattering [113], and by extrapolating these experimental data it is found that R_g of PVP (40,000 g/mol) is approximately 13.87 nm.

In our simulation, the PVP chain was considered as a straight line at its initial conformation. The equilibrium distance between two consecutive beads was set at 1 (r_o=1). A rectangular simulation box of dimension (80x20x20 r_c^3) was used and periodic boundary conditions were applied. The total number of beads was 96,060 including 96,000 water beads and 60 PVP beads. The equilibrium state of the system of one polymer chain and water with different values of k_a and k_b were obtained after running $6x10^6$ time steps for PVP. Figure 4.1 is a display of the equilibrium conformation of a single PVP in water environment. In Table 4.2, we present the values of L_e and R_g for single PVP molecule in water. McFarlane et al. obtained R_g experimentally while Kokuoz et al. estimated L_e with the assumption that the statistical segment length of PVP is similar to those of polystyrene. Based on their data, we got values of L_e that are smaller than R_g for PVP (40,000 g/mol). However, our DPD results always showed that L_e is larger than R_g.

For ideal polymer chain, the ratio between L_e and R_g is $6^{1/2} \approx 2.45$ [111].

Table 4.2. L_e and R_g of a single PVP molecule (40,000 g/mol) in water medium.

	From literature review	From DPD simulation
L_e (nm)	11.38*	23.06
R_g (nm)	13.87**	15.97

* This value was interpolated from data of Kokuoz et al. [112]

** This value was extrapolated from data of McFarLane et al. [113]

So, we decided to choose parameters that match R_g instead of L_e. The difference of R_g between our results and the experimental value in Table 4.2 is quite small to allow the assumption that the structure of PVP is described well in our model. The suitable bond and angle potential parameters for polymers (k_b=100 and k_a=5) were determined for the simulation, and were used in the simulations. Since R_g and L_e are average values, it is more appropriate to compute these properties in a solution that has a lot of PVP molecules. So, 20 PVP molecules were added into the water medium in the simulation. The initial conformation of each chain was obtained from the previous simulation of the single PVP molecules in water (Figure 4.1). The positions of all 20 PVP chains were set randomly in the simulation box. The simulations comprised of a total of 82,200 beads including water and PVP polymer, in a computational box of 44.1 x 44.1 x 44.1 nm^3 with periodic boundaries. Figure 4.2 is a snapshot of all PVP chains in water after running $2x10^6$ steps. The average end-to-end distance $<L_e>$ and radius of gyration $<R_g>$ of PVP in solution were found to be 20.79 nm and 12.10 nm, respectively. It is noted that L_e and R_g of polymers in solution get smaller than those of one individual PVP molecule, because of the attraction among PVP molecules. Comparing with the data from the literature in Table 4.2, the difference of $< R_g >$ is quite small (around 12%) to consider that our DPD results can represent the conformation of PVP molecules in meso-scale simulations.

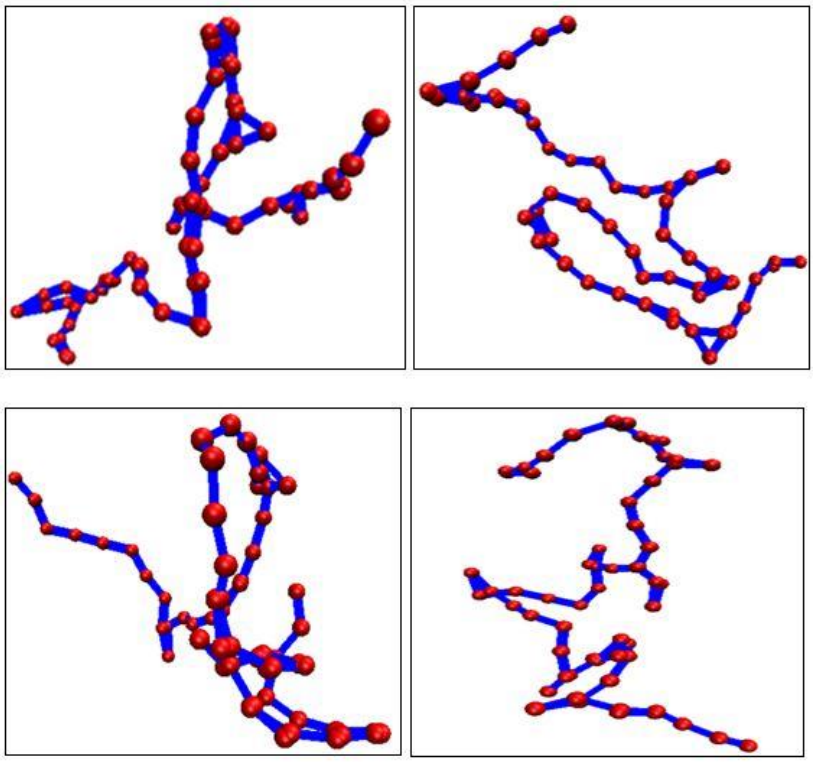

Figure 4.1. Some conformations of a single PVP molecule in water (all water beads are removed for clarity). Red spheres are PVP beads and blue lines are spring bonds to connect two consecutive PVP beads.

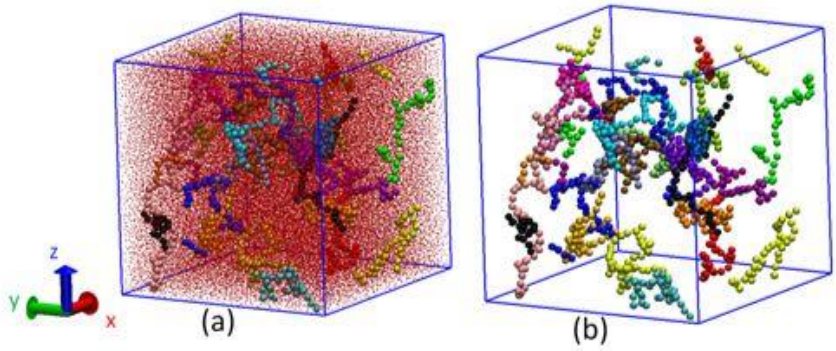

Figure 4.2. A snapshot of PVP molecules in water. (a) Small red dots are water beads. Other color beads are PVP, using the same color for the same PVP molecule. (b) All of water beads are removed.

4.3. Results and discussions

a. Conformation of physically adsorbed PVP on CNP

In Figure 4.3, we display the equilibrium physical adsorption of PVP on surfaces of different shapes: spherical (Figure 4.3(a) and 4.3(b)), cylindrical particle (Figure 4.3(c)), graphene particle (Figure 4.3(d)) and a hydrophobic surface (Figure 4.3(e)). Due to the strong attractive forces, the surface of CNPs was fully covered by PVP molecules. Both PVP and CNP are non-polar compounds, and they could attract each other. Fleer and Scheutjens have suggested that there are three possible conformations of a polymer at a liquid – solid interface: trains (the whole polymer molecule is in contact with the solid surface), loops (a part of polymer molecule is in the solution while both ends of the polymer chain are on the surface) and tails (one end of the polymer molecule is on the surface and another end is oriented to the solution) [114]. For the S1 particle (smaller sphere), most of the PVP polymer chains were adsorbed in loops and tails style on the surface. When the diameter of the sphere increased, the conformation of the PVP molecules switched into the trains style with only a few of molecules attached on their tails. This might be caused by the increase of surface area available for adsorption. There is more space for the polymer molecules to adsorb entirely on a bigger spherical surface. Note that every carbon bead on the CNP surface was able to become an adsorption site. For cylindrical shape, it is found that most of PVP molecules prefer to form trains style on CNP surface. A few of polymer chains also adsorbed in loops and tails style. On the surface of the cylindrical CNP, adsorbate polymer chains occupy areas like islands, forming a single layer adsorption. The conformation of PVP polymer distributed on surface of cylindrical CNP (Figure 4.3(c)) looks similar to results of Nativ-Roth et al. in MD simulation [94]. In that work, the non-wrapping adsorption mechanism of poly-

ethylene-oxide block group of copolymer on carbon nanotubes was also like islands (lack of structure). In the case of the G particle, it is observed that PVP molecules can exist in all three possible conformations (trains, loops and tails). Most of them, however, were adsorbed in trains style.

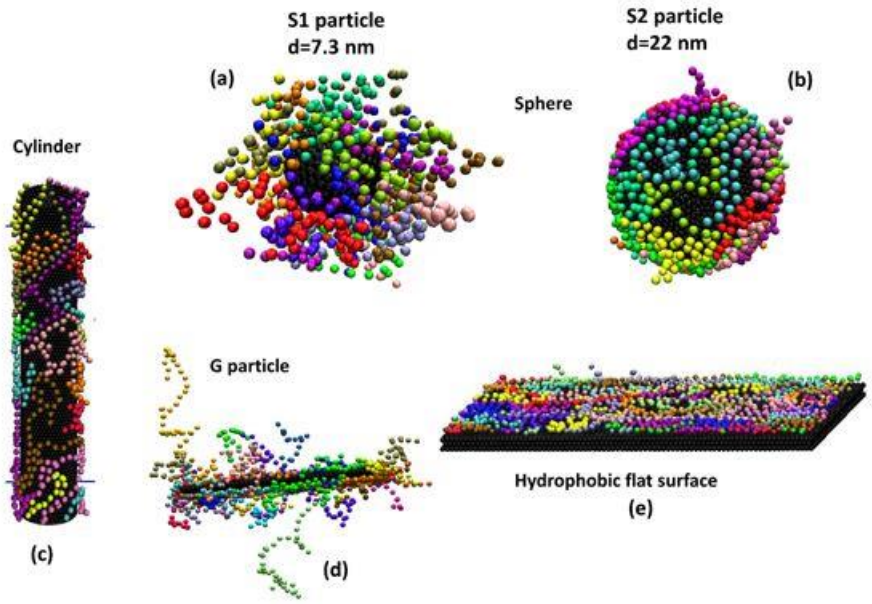

Figure 4.3. The conformation of PVP polymer on different shape of CNP including sphere (a, b), cylinder (c), graphene-like (d) and hydrophobic flat surface (e) in water medium. All water beads are removed for clarity. CNP and flat surface is black bead. Other color beads are PVP, the same color for the same PVP molecule.

Concentration of adsorbate polymers on CNP surface is listed in Table 4.3. For spherical shaped particles, the S2 particle had a higher concentration of adsorbed polymer than S1 because of increasing surface area. Even though the surface area of S2 is 9 times that S1, the increase of adsorbed polymer was around 1.5 times. With the same surface area, cylindrical CNP is more attractive PVP polymer than S1 particle. For the G particle, it is seen that there is a high ability for PVP adsorption on both of its sides. In addition, the average values of end-to-end distance ($<L_e>$) and radius of gyration ($<R_g>$) of adsorbate polymers shown in Table 4.3 imply that the polymer conformation might be

quite similar on surfaces of different shapes, although they can adsorb on the surface with different styles (trains, loops or tails). In the following sections, the particles with PVP adsorbed at equilibrium were individually released into a Couette flow to investigate their behavior under constant shear rate.

Table 4.3. The properties of adsorbate PVP polymer on CNP surface

Shape of particle		Surface area of particle (nm^2)	Adsorbate concentration (ppm)	$<L_e>$ (nm)	$<R_g>$ (nm)
Sphere (d=7.4nm)	S1	167.4	134.9	13.72	7.54
Sphere (d=22nm)	S2	1520.5	205.8	11.66	6.65
Cylinder		1570.8	258.1	12.17	7.43
Graphene-like		760.3	548.5	11.24	7.40
Flat surface		864.4	283.7	10.75	6.02

b. Desoprtion of the PVP from CNP under shear flow

A suspension of PVP wrapped CNP needs to be stable under shear, in order for it to be used in a practical application, where it will likely need to go through a pump and be sheared. In addition, if the PVP wrapped CNP suspension would be pumped into tight pores, such as the micro- and nanoscale pores in hydraulic fracturing, it will also undergo shear. It is, therefore, needed to be able to predict the stability of the suspension under such conditions. The system of PVP-wrapped CNP (as seen in Figure 4.3) was subjected to simple shear flows (Couette flow), to study the desorption of PVP under shear. The PVP wrapped CNP was only allowed to move after the velocity profile of water was steady and fully developed. The positions of the PVP wrapped CNP were reported every 1000 time steps.

i. Spherical CNP

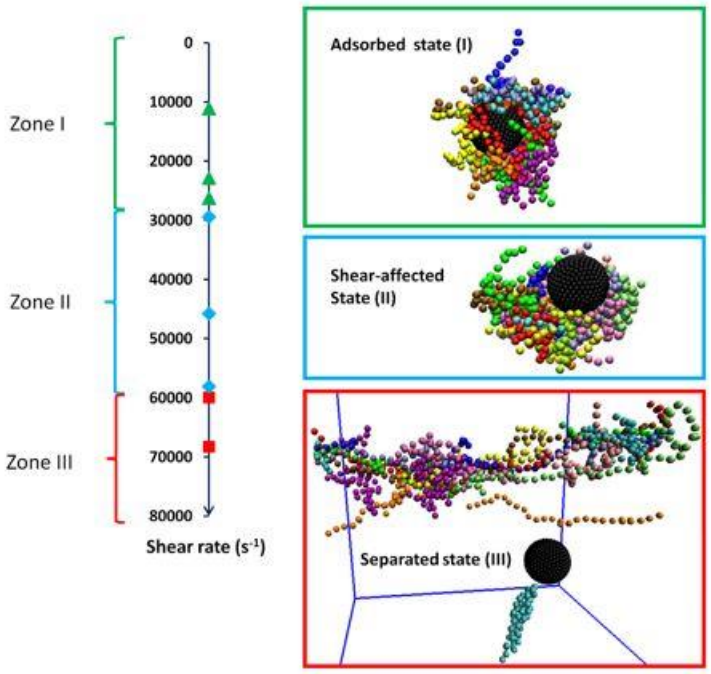

Figure 4.4. Simulation snapshots of all PVP-wrapped spherical CNP states under shear (water beads are not shown for clarity. Color code is the same as that in Figure 4.3). There are three zones of shear rate which is corresponding to three possible states of spherical particle such as zone I (adsorbed state), zone II (shear-affected state) and zone III (separated state).

Depending on the value of the shear rate, the status of the spherical particle grafted with PVP was classified into 3 states: adsorbed, shear-affected and separated. In Figure 4.4, we present the shear rate zones for each state of both S1 and S2 particles. At low shear rate conditions (zone I), the physical interaction between PVP and particle is strong enough to dominate the shearing force of the flow. It means the adsorption of PVP on spherical particles is preserved stably during the particle propagation in Couette flow. In the shear-affected state (coresponding to zone II), the adsorded PVP on the spherical particle migrated on the surface and gathered in a region where minimum shear stress occurred. About half of the surface area of the spherical particle did not have any polymer

coverage. At very high shear rates (zone III), the PVP polymer chains were completely separated from the spherical particle and can be seen in the bulk fluid. We define as γ_1 and γ_2 the transition shear rate values for PVP to change its status from adsorbed to shear-affected, and from shear-affected to the separated state, respectively. It is seen that the shear rate range of each zone is nearly the same for both S1 and S2 particles. Therefore, we can say that both particles have nearly the same transiton values for each zone of shear rate: zone I (0 to γ_1 = 27,800 s^{-1}), zone II (from γ_1 to γ_2 = 58,800 s^{-1}) and zone III (> γ_2).

ii. Cylindrical CNP

The physical adsorption of PVP on a CNP is influenced by exerting a shearing force. Figure 4.5 is a visual illustration of the states of the PVP-wrapped cylindrical CNP when it undergoes shear. It is clearly seen that there are also three conditions that we can distinguish, named as follows: Adsorbed (I), where the PVP is adsorbed on the CNT surface forming the typical islands of adsorbent; Shear-affected (II), where the PVP chains start to stretch and extend away from the CNP surface while still adsorbed at the surface; Separated (III), where the PVP chains are fully desorbed from the CNP. The shear-affected state is a transition state between the adsorbed and separated states. Each state appears within a specific range of shear rate. We can approximate that the adsorbed PVP started to get affected by shear at about γ_1 = 4265 s^{-1} and desorbed at γ_2 = 5400 s^{-1}. For shear rate (γ_s) $\leq \gamma_1$, the interaction between PVP and CNP is strong enough to hold PVP chains adsorbed around the CNP. In this state, the PVP is physically adsorbed on the CNP and the suspension is stable. The PVP chains still cover almost fully the surface of the CNP. Then, the PVP-functionalized nanotubes start to be affected by the shear, when γ_s is between 4265 and 5400 s^{-1}. In this state, the distribution of PVP on CNP begins

to change. PVP chains untangle and move forward in the direction of the flow, they stretch out unveil more free space on the surface of the CNT. Finally, PVP chains get completely separated from the CNP and go into the bulk phase under high shear rate ($\gamma_s > \gamma_2 = 5400\ s^{-1}$). In the separated state, the physical adsorption of PVP on CNP is reversed because of the strong shearing force.

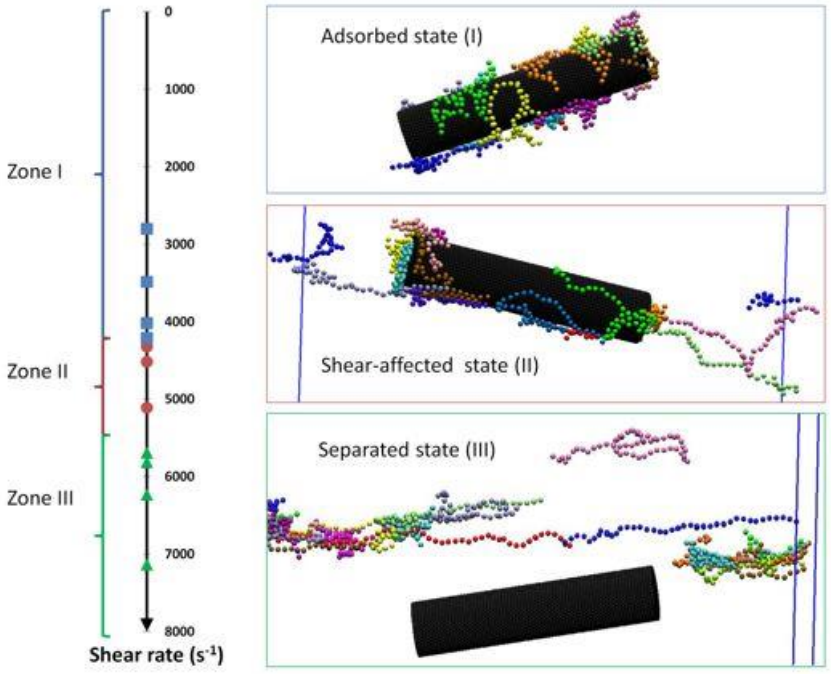

Figure 4.5. Snapshots showing all states of all PVP-wrapped cylindrical CNP under shear (water beads are not shown for clarity. Color code is the same as that in Figure 4.3). There are three zones of shear rate, which correspond to three states of PVP-functionalized nanotubes: zone I (adsorbed state), zone II (shear-affected state) and zone III (separated state).

iii. Graphene-like particle

For the graphene-like particle (G), there also have been three possible states of polymer adsorption as the shear rate changed (see Figure 4.6). It is also seen that the range of zone I was smaller than for spheres, with values of $\gamma_1 = 12{,}400\ s^{-1}$. For zone II, the zone was expanded from γ_1 to $\gamma_2 = 73{,}900\ s^{-1}$. The desorption of PVP occured when shear

rate of the flow was larger than γ_2 (zone III). The adsorbed PVP polymer on the G particle was also affected under shear. The PVP molecules began to stretch out from the surface of the G particle when the shear rate increased. Before departing totally from the surface of the G particle, the PVP molecules stretched with long tails around the particle. Eventually, these tails got longer with increasing the shear rate and finally the whole PVP molecule went into the solution and propagated as a free molecule.

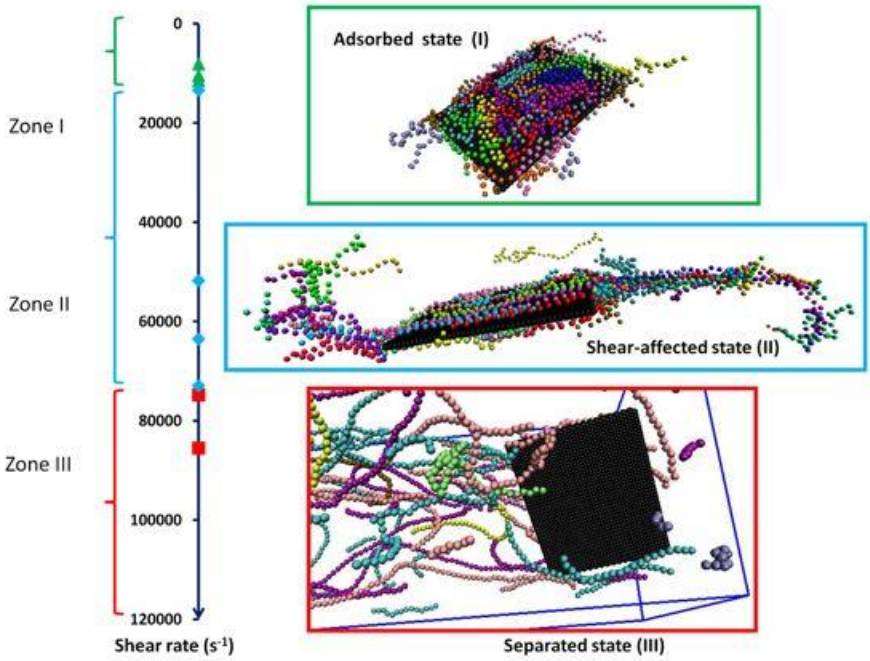

Figure 4.6. Simulation snapshots of all PVP-wrapped graphene-like particle states under shear (water beads are not shown for clarity. Color code is the same as that in Figure 4.3). There are three zones of shear rate which is corresponding to three possible states such as zone I (adsorbed state), zone II (shear-affected state) and zone III (separated state).

iv. The effect of curvature

Table 4.4 is a presentation of the range of shear rates that correspond to the three possible states of PVP adsorbed on CNPs that have the same surface area but different shapes (cylinder, sphere and graphene). It is seen that the coating of the graphene-like particle is the most stable under shear. This phenomenon might be explained by

considering that the sum of attraction potentials between the beads of the PVP molecule and the carbon beads and on the graphene surface is more than for the cylindrical and spherical particles. For spherical particles, a higher shear rate is required in order to completely separate the polymer coating compared to the cylindrical particles. A hydrodynamic reason for this effect is that the shear rate acting on a sphere is more symmetric than for a cylinder. The shearing forces exerted along the axial direction on a cylinder is different than those in the tangential direction. Additionally, it is presented in

Table 4.4. The range of shear rate for different CNP shape (same adsorbed surface area)

Shape of CNP	Shear rate (γ) corresponding to each possible state (s^{-1})		
	Adsorbed state	Shear-affected state	Separated state
Cylinder	0 – 4,265	4,265 – 5,400	> 5,400
Sphere (S2)	0 – 27,800	27,800 – 58,800	> 58,800
Graphene-like (G)	0 – 12,400	12,400 – 73,900	> 73,900

Table 4.4 that the range of zone I (adsorbed state) for a graphene particle was narrower than for the spherical one, but wider than for a cylindrical particle. In the shear-affected state, the G particle has a wider range of zone II (expanded to 73,900 s^{-1}) than both the cylindrical and spherical particles. It is implied that the adsorption of PVP on the graphene-like particle was stronger than for cylindrical and spherical particles. This is a clear case where the effect the particle shape is obvious. Furthermore, the concentration of adsorbed PVP on the graphene-like particle is higher than for the cylinder, and the cylinder is in turn larger than the spherically shaped particle (see Table 4.4). This is another demonstration of the effect of surface curvature on the adsorption of the polymer on CNP.

c. The adsorption and desorption of PVP on a hydrophobic flat surface

The physical adsorption and desorption of PVP on a hydrophobic flat surface (like a carbon surface) under the effect of shear was also investigated. The hydrophobic surface consisted of three layers parallel to the (xy) plane. All DPD beads on each layer were arranged in a square lattice with constant nearest neighbor distance equal to $0.5r_c$ in the x and y directions. The distance between two consecutive layers was equal to $0.5r_c$. It is noted that water and PVP beads could not penetrate into the hydrophobic surface. Figure 4.3(d) is a display of the equilibrium adsorption of ~285 ppm PVP on the hydrophobic flat surface. The concentration of PVP in solution was the same as in the previous simulations, 565 ppm. Almost all adsorbed polymer molecules stayed on the surface following the trains style (i.e., each molecule laid on the surface with all parts of it in contact with the surface). A few of them had a short tail oriented outward from the surface (tails style).

Under the influence of shear, adsorbed PVP on the surface could separate and move into the bulk phase. We see in Figure 4.7 that there were only two states (adsorbed and separated state) of PVP adsorption on the surface. Because carbon surface is hydrophobic, the velocity of the water in the region close to the surface is not zero – there is a velocity slip. So, PVP polymers can slide on the hydrophobic surface. Based on our observations, there does not appear to be a shear-affected state, like the case of PVP molecules adsorbed on CNPs. When the shearing force was strong enough, PVP departed from the surface immediatedly. In contrast to the case of CNPs that were themselves moving, the PVP molecules can only move with the flow when the surface is kept stationary. The adsorption of PVP on surface was stable (zone I) as the shear rate of the fluid was lower

than 113,200 s^{-1}. The desorption happened when shear rate was larger than 113,200 s^{-1}.

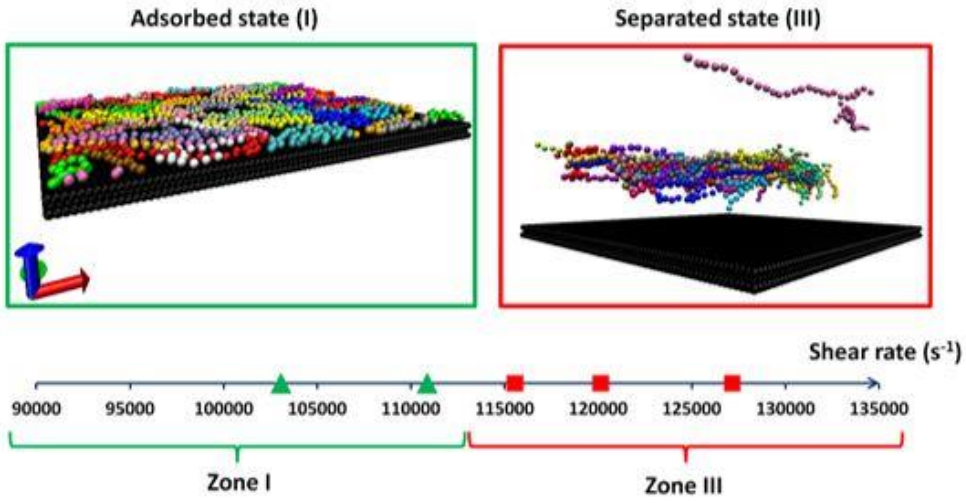

Figure 4.7. Snapshots showing adsorption status of PVP polymer on hydrophobic flat surface under shear. Water beads are not shown for clarity and color code is the same as that in Figure 4.3. There are two zones of shear rate which is corresponding to the adsorption (zone I) and desorption (zone III) of PVP polymers on surface.

4.4. Conclusions

In this chapter, we have investigated the effect of shearing force on the physical adsorption of a polymer on CNPs with different shapes (spherical, cylinder and thin sheets), as well as its adsorption/desorption on a hydrophobic flat surface. It was found that there are three possible states of PVP adsorption on CNPs under shear (adsorbed, shear-affected and separated states) depending on the strength of the shear rate. The zone of shear rate corresponding to these states relies on the shape of CNP. For spherically shaped particles, the polymer stays adsorbed when $\gamma < \gamma_1 \sim= 27{,}800\ s^{-1}$), it is shear-affected when $\gamma_1 < \gamma < \gamma_2 \sim= 58{,}800 s^{-1}$ and is separated when $\gamma > \gamma_2$. For a graphene-like particle, the stable adsorption occurs when $\gamma < \gamma_1 \sim= 12{,}400 s^{-1}$, the polymer is shear-affected when $\gamma_1 < \gamma < \gamma_2 \sim= 73{,}900 s^{-1}$ and it gets separated from the surface when $\gamma > \gamma_2$. The shape of the nanoparticle affects the threshold shear rates for these three states of

PVP adsorption. For particles that have the same surface area, the order of decreasing stability strength of PVP adsorption under shear is as follows: graphene sheet > sphere > cylindrical particle. Regarding the conformation of PVP polymers on the CNP surface, the average values of $<L_e>$ and $<R_g>$ increased with increasing of shear rate.

While changes in the molecular weight of the polymer could likely lead to different threshold values for transition between one state of polymer adsorption to another, the finding that there are three states of adsorption under shear should hold. Changes in the molecular weight of the polymer will likely lead to different percentages of polymer chains adsorbed as trains or loops or tails, leading to changes on the values of shear needed to detach the polymer.

For a hydrophobic flat surface, there were only two states (adsorbed and separated state) of PVP molecules on the surface under shear. There is no shear-affected state, like the one observed for PVP on a CNP surface. Due to the hydrophobic properties of the surface, polymer chains could slip on the surface in the adsorbed state when $\gamma > \gamma_1 \sim= 113{,}200\ s^{-1}$. The desorption of PVP molecules took place thoroughly and it was seen that the polymer moved into the bulk phase when the shear rate of the flow filed was higher than γ_1.

When using nanoparticles as a delivery agent, the agglomeration of nanoparticles is an undesired problem that needs to be avoided for successful application. So, the presence of coating materials is one of the essential factors to disperse nanoparticles in the solution. Our findings show that the nanoparticle coating with physical adsorption can be lost when they undergo high shear rate conditions might be encountered when the suspension flows through pumps or through tight pore spaces. Depending on equipment and purpose of

use, shear rate changes over a wide range. For example, shear rates at centrifugal pump impellers could be reach the order of 100,000 s^{-1} [115]. A commercial parallel plate rheometer can reach shear rates up to 80,000 s^{-1} [116]. An extremely high shear rate (250,000 s^{-1}) could be obtained in a piston driven capillary rheometer with a magnetic valve) [117]. In typical flow through Berea sandstone, however, it has been found that the stress follows a probability distribution but the maximum shear stress is around 1.5 dyne/cm^2 (equivalent to shear rate 150 s^{-1}) for pressure drop of 10,000 Pa/m in 250mD Berea [118]. This should be considered in pumping strategies for ensuring that coatings can remain adsorbed on the nanoparticles.

Chapter 5. Surfactant stabilized suspensions of carbon nanotubes

5.1. Introduction [‡]

Enhanced oil recovery (EOR) processes are often applied to increase the amount of oil recovered in mature oil reservoirs. One of the main EOR techniques is chemical flooding [3], where flooding with surfactants can be used to recover conventional oil (API specific gravity higher than 25^{o}) that remains in the reservoir after water flooding [119]. Fundamentally, surfactant flooding is used to reduce the interfacial tension (IFT) between oil and water. The IFT must be lower than 0.01 mN/m to mobilize residual oil through surfactant solution injection [120]. Surfactant flooding leads to increases in the capillary number, as well as to the mobilization of residual oil trapped in the pore structure [3]. However, loss of surfactant due to adsorption on the rock surface can significantly increase the cost for the whole process. To overcome this economic problem, a number of solutions have been explored. Zaitoun et al. suggested using anti-adsorption agents (ANTISOB^{TM}) to decrease the adsorption of the primary surfactants [121]. Dawe and Oswald indicated that the losses of surfactant could be reduced by using optimized surfactant blends (including DOWFAX disulfonated surfactant) in field trials.[122] Liu et al. proved that the efficiency and economics of a chemical flood process could be improved by varying the injection scheme [123]. However, there is still need for improvement in order to make surfactant EOR economically feasible.

Recently, nano-technology offered a promising approach to reduce the loss of surfactants

[‡] Material in this chapter has been published in Minh D. Vo, Benjamin Shiau, Jeffrey H. Harwell, Dimitrios V. Papavassiliou, Journal of Chemical Physics, 2016, 144, 20,204701.

by using nanoparticles as surfactant carriers [7]. CNTs could be good candidates for delivering surfactants to the water/oil interface and reducing surfactant adsorption to the rock. The hydrophobic surface of a CNT is favorable for surfactant tail adsorption [8]. In this case, surfactants can stabilize the CNT suspension, while the CNTs take a role as surfactant carriers. The nanoparticles (we use this term to indicate a CNT with adsorbed surfactants) could propagate through the oil reservoir, reach the oil-water interface and then release the surfactant to lower the IFT. Actually, there have been many difficulties with this idea, starting with the feasibility of surfactant adsorption on the CNTs.

The adsorption of surfactants on CNTs has been addressed in several published reports with MD simulations. Tummala and Striolo studied the aggregate morphology of sodium docecyl sulfate (SDS) on a SWCNT [124]. They found that the adsorption morphology of SDS on SWCNT depended on CNT diameter, its chirality and the concentration of SDS. Lin et al. investigated the adsorption and surface self-assembly of bile salt surfactant sodium cholate on SWCNT in an aqueous solution [125]. It was found that cholate ions wrap around a SWCNT like a ring, with a small probability of perpendicular orientation along the major axis of the SWCNT. Sohrabi et al. pointed out that the random and disordered adsorption of mixed surfactants (cetyltrimethylammonium bromide and SDS) on CNTs could happen at low surfactant concentration [126].

At the coarse-grained level, DPD simulations have been used to study the behavior of surfactants in solution [52]. Because of the larger time and length scales possible, application of DPD allows the simulation of a system with higher concentration and higher molecular weight of the surfactant, as well as calculations of the hydrodynamic properties of the system. Angelikopoulos and Bock used DPD methods to investigate the

self-assembly of the general surfactant (H_5T_5 – 5 hydrophilic head beads and 5 hydrophobic tail beads) on crossing CNTs [44]. It was concluded that surfactant aggregation is directed to the CNT crossing and the size and shape of adsorbed surfactant aggregates could be estimated from properties of the bulk micelles. Calvaresi et al. showed possible conformations of surfactants (SDS and sodium dodecylsulfonate) on a CNT (cylindrical micelle, hemimicelles and random adsorption) with DPD simulation [8]. Arai et al. studied the self-assembly and polymorphic transition of the general surfactant in nanotubes, as well as the effect of water-nanotube interaction on the self-assembly morphologies in DPD [127]. In other words, DPD simulation is a good tool to describe the adsorption of surfactants on the CNT surface, as well as to model other systems at the mesoscopic scale.

In the present work, we give a detailed description of the morphology of mixed surfactants adsorbed on a CNT. This report includes the presentation of the DPD algorithm and simulation protocol for simulating surfactant interactions with the CNTs. We determine the self-assembly of commercial surfactants (AF and TG) in water, and we calculate quantitatively other properties of surfactant micelles (shape, size, diffusivity) via their asphericity, radius of gyration, aggregation number, and mean squared displacement (MSD). The critical micelle concentration (CMC) of each surfactant was employed to validate our surfactant model. We then describe the adsorption of AF, TG and their mixture on the surface of the CNT. The morphology and behavior of surfactants adsorbed on the CNT are also examined in detail.

5.2. Simulation details

A schematic representation of the coarse-grained model applied in this report is shown in

Figure 5.1, where the model for water, surfactant molecules and CNT is presented. Tails of both surfactants were nearly the same size (13 CH_2 atoms). One DPD bead represented the whole of the surfactant tail. From the experiments of Lu et al., we find that the volume of the surfactant tail is around 380 A^3 [128]. It is nearly equivalent to the volume of 13 water molecules. The number density of water (ρ) was set to a value of 5. So, the length scale (r_c) of the DPD simulation was 1.249 nm. For alfoterra, there were 4 beads (C–N–N–S) connected via harmonic bonds to form its single molecule. The length of the surfactant tail was calculated from the following empirical equation [129]

$$l_c = 1.5 + 1.265n \quad (\text{Å}) \tag{5.1}$$

where *n* is the number of carbons in the alkyl chain, so that the length of AF was 1.79 nm. We assigned the equilibrium bond length of C and N bead ($r_{o(C\text{-}N)}$) to be 1.44 r_c. For N-N and N-S bonds, their equilibrium bond length was set to 0.35 r_c, which was found based on the DPD assumption of maintaining the same volume for all beads. For TG surfactant, we used 8 beads (E–O–O–O–O–O–O–O–H) to duplicate the structure of this non-ionic surfactant in the DPD simulations. The last bead (H) was considered to be more hydrophilic than other O beads, because of the hydroxyl group at the head of the TG molecule [130]. Two consecutive beads were also connected by harmonic bond potential. The equilibrium bond length of E-O, O-O and H-H were selected as 1.44, 0.35 and 0.35 r_c, respectively. The spring constant (ks) was set to 100 k_BT/r_c^2 for all bond potentials in both AF and TG, to maintain the bond length around the equilibrium value [131]. The CNT was modeled as an infinite cylinder at the center of the computational domain during the whole simulation with diameter of 10 nm (equal to $8r_c$). Since this study is focused on the adsorption of surfactant on the outer surface of the CNT, it was not needed to have

additional bond and angular potential among CNT beads. The surface of the CNT was constructed by 8162 beads, and it was treated as a rigid body. All CNT beads were organized in an equilateral triangular lattice with nearest neighbor distance $h= 0.3r_c$ (see Figure 5.1).

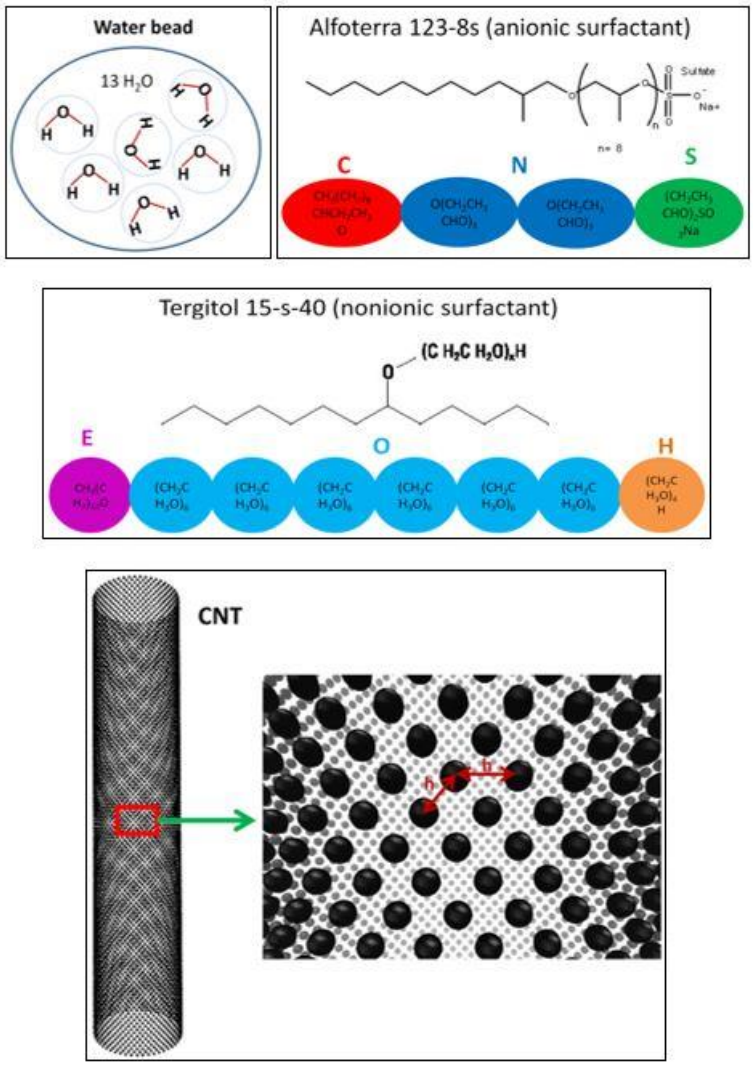

Figure 5.1. Schematic representation of the coarse-grained model for water, CNT, AF and TG surfactants in our DPD simulation. An AF molecule contains one tail bead (red – C), two PO group beads (dark blue – N) and one head bead (green – S). TG molecule has 8 beads including one tail bead (purple – E), six hydrophilic EO group beads (light blue – O) and one last hydrophilic EO group bead (orange – H).

One of the most important issues in DPD is the value of the repulsion parameters. For the

same species, Groot and Warren proved that a_{ii} is equal to 15 k_BT for number density of water ρ=5 [52]. For the head bead (S) of AF anionic surfactant, electrostatic interactions were indirectly added into the DPD algorithm by increasing the repulsion parameter to $a_{S\text{-}S}$ = 20 k_BT [132, 133]. For different species, the repulsion parameters were chosen by following published reports about DPD simulations. For water and CNT interactions, the repulsion parameter has been obtained in prior work from our laboratory by ensuring that the slip length and the drag coefficient agree with MD results [108], as described in Chapter 3. The use of these specifically obtained parameters is one of the main reasons that the simulations described herein are specific to a system of CNTs in an aqueous solution. The repulsion parameter of water and surfactant molecules was validated by comparing CMC and aggregation number (N_{ag}) between DPD results and experiment data. Maiti et al. proved that the repulsion parameter between CNT and polymer could be determined via the Flory-Huggins theory as well [45]. So, we could consider beads (C, E), (N, S), (O, H) as polyethylene, polyethylene oxide and polypropylene oxide, respectively. For ρ=5, Maiti and McGrother also demonstrated that the repulsion parameter depends on the solubility parameter of each component, the temperature and the volume of bead as follows [134]:

$$\chi_{ij} \approx 0.689\left(a_{ij} - a_{ii}\right) \tag{5.2}$$

$$\chi_{ij} = \frac{V_b}{k_B T}(\delta_i - \delta_j)^2 \tag{5.3}$$

where indices *i, j* designate beads i and j; δ is the solubility parameter; χ is the Flory-Huggins parameter and V_b is the volume of a DPD bead.

Kuo et al. calculated the Flory-Huggins parameter via the average mixed energies from Monte Carlo simulation for both ionic and non-ionic surfactants [135]. Then, the

repulsion parameters among AF and TG beads were adopted from Kuo's study. All repulsion parameters implemented in this work are reported in Table 5.1. For simplicity, reduced units were used in DPD calculations. The simulations were performed in a periodic cubic box of constant volume V = 40x40x40 r_c^3. The temperature of the system was kept constant at reduced temperature $k_BT=1$ (equivalent to 298 K). The canonical ensemble (NVT – constant-temperature, constant-volume) was implemented in all DPD calculations. The noise amplitude and friction coefficients were set to $\sigma = 3$ and $\gamma = 4.5$, respectively [52]. Additionally, all the simulations were carried out for $5x10^6$ steps with a time step of 0.02 in reduced DPD units. The visual molecular dynamics (VMD) software was used to visualize all snapshots presented in this report. In the system of water and surfactant, there were 320,000 water beads in the system and the amount of surfactant depended on its concentration. In the presence of CNT, the number of water beads was 309,947 in order to maintain its number density. Initially, positions of water and surfactant molecules were randomly distributed in the whole simulation domain. Once every 1000 time steps, configurations of the whole system were recorded for further analysis. The time scale in the simulation was determined by calibrating with the diffusion constant of water [67]. The slope of the mean square displacement of water beads with time is equal to six times the water DPD diffusion constant (D_w). So, the time scale (τ) in our DPD report was 2.42 ns.

Table 5.1. List of all repulsion parameters in terms of k_BT/r_c. All symbols are similar to those used in Figure 5.1.

	W	CNT	C	N	S	E	O	H
W	15	60	43.5	36.75	0	81	20	5
CNT		15	20.6	28.3	42.4	20.6	40.8	40.8
C			15	55	81	15	74	74
N				15	79	55	81	81
S					20	53	32	32
E						15	81	81
O							15	40
H								15

Vishnyakov et al. have presented an algorithm to determine the critical micelle concentration (CMC) of surfactants based on their position in the system for DPD [136]. Two surfactant molecules in an aqueous medium would be considered in one aggregate if any two of their tail or middle beads overlapped. An aggregate would be counted as a micelle, if the number of molecules in this aggregate was larger than a specified threshold (N_{mic}). If the number of surfactant molecules in an aggregate was less than a specified number (N_{mono}), it would be considered to belong to the aqueous solution (free monomer) in equilibrium with the micelles. The concentration of these free monomer surfactants was determined as the CMC in water. The system would be considered to have reached equilibrium when the number of free surfactants and micelles stabilized. Based on the distribution of micelle aggregation numbers, we chose $N_{mono} = 4$, $N_{mic} = 15$ and $N_{mono} = 4$, $N_{mic} = 6$ for computing the CMC of AF and TG, respectively. There is no clear criterion for choosing the value of N_{mono} and N_{mic} in DPD calculations.[137] Any aggregate whose N_{ag} was in the range of N_{mono} and N_{mic} was considered as a non-equilibrium micelle. The aggregation number of almost all surfactant micelles from our calculation was larger than

N_{mic} when the system reached equilibrium state.

5.3. Results and discusions

a. Critical micelle concentration and morphology of AF and TG in water

To obtain the appropriate values of the repulsion parameters for a real anionic (AF) and non-ionic (TG) surfactant in water, the CMC of each surfactant in water was found first, in order to validate our DPD results and to ensure that the model parameters chosen were appropriate for the simulated systems. Note that all interactions of water and surfactant beads in Table 5.1 were the final choice by employing trial and error. Figure 5.2(a) is a plot of the equilibrium conformation of 2.1 wt% of AF (simulation case A) in water at room temperature. As expected, AF molecules tend to agglomerate in the aqueous phase. In each aggregate, the hydrophobic tail assembled in the center (red beads) and the polar head beads (green) were on the outside. In order to calculate the CMC of the surfactant, we conducted simulations at different surfactant concentrations to calculate the free surfactant concentration as a function of total surfactant concentration [138] and plotted the results in Figure 5.3(a). It is seen that the concentration of the free monomer reaches a plateau when the total concentration of the surfactant is greater than 108 ppm. At higher total concentration, there is a slight decrease of free monomer concentration. So, the CMC of AF in our DPD calculation is reported to be 108 ppm. In experiments, Witthayapanyanon et al. determined that the CMC of AF is around 98 ppm [139]. The difference between the DPD simulation results and the experimental value is 10.2%. It is acceptable that our simulation can be used to characterize the behavior and the properties of AF in water. The number of molecules in each micelle varied from 15 to 60 (see Figure 5.3(a)). This is the aggregation number of the surfactant (N_{ag}). The average of N_{ag} was

approximately 32 for AF micelles.

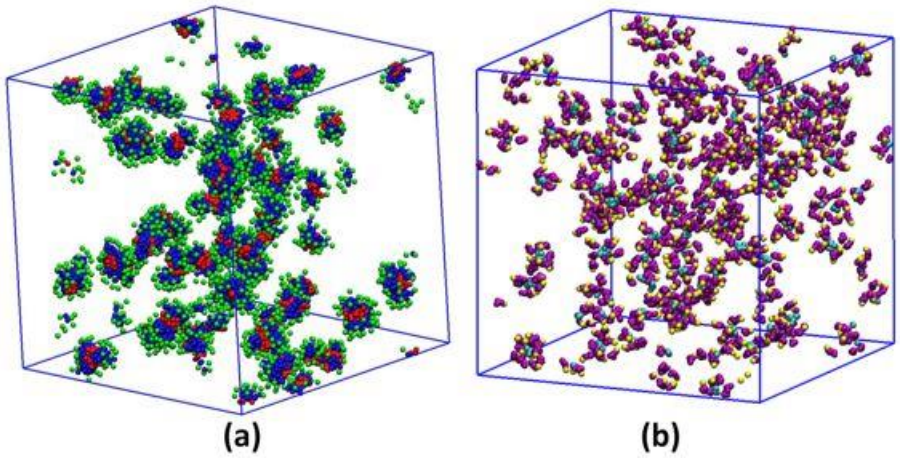

Figure 5.2. The snapshot of 2.1% (wt) of AF (a) and TG (b) in water after $5x10^6$ time steps. All of water beads are removed for clarity. (a) In case A, there are 8,000 AF beads (2000 molecules) in the system. Red, blue, green beads are C, N and S beads, respectively. (b) In case B, there are 6,400 TG (800 molecules) beads in simulation box. Cyan, purple, yellow beads are hydrophobic tail, hydrophilic EO groups and last hydrophilic EO groups of TG molecules, respectively.

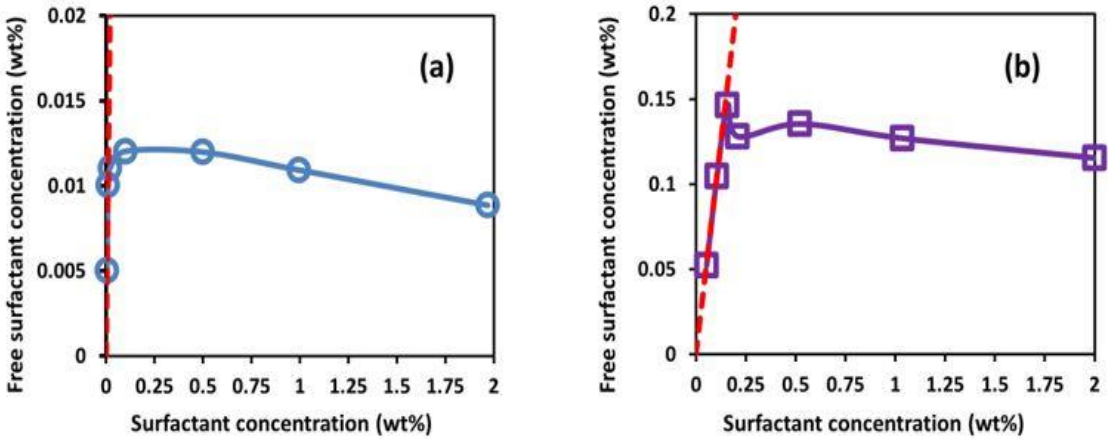

Figure 5.3. The monomer concentration as a function of the total surfactant concentration for AF (a) and TG (b). The red dashed line has a slope of one.

To characterize the shape of the AF micelles, the value of the parameter asphericity (A_s), which is a quantitative measure of the deformation of a micelle from a spherically symmetric geometry, was calculated [140]. It was assumed that the shape of a micelle

can be determined by the position of all AF hydrophilic head beads. Asphericity of a body varies from 0 to 1 (A_s=0 for a perfectly spherical globule; A_s=0.25 for a circle without width, a disc; and A_s=1 for an infinite cylinder) [141]. The values of A_s were computed from the moment of inertia tensor (T) of each micelle [141],

$$A_s = \frac{(R_1^2 - R_2^2)^2 + (R_2^2 - R_3^2)^2 + (R_3^2 - R_1^2)^2}{2R_g^4} \quad (5.4)$$

$$T_{ij} = \frac{\sum_{m=1}^{N} (S_{im} - S_i^{CM})(S_{jm} - S_j^{CM})}{N} \quad (5.5)$$

where N is the total number of head beads in a micelle, R_1^2, R_2^2 and R_3^2 are three eigenvalues of tensor T (i.e., the three principal radii of gyration squared for all N beads), S_{im} is the position of bead m in the i^{th} Cartesian component (*i* denotes x, y or z), S_i^{CM} is the center of mass of N beads in coordinate *i*. The distribution of asphericity and radius of gyration of all AF micelles at equilibrium can be seen in Figure 5.4 for simulation case A. All of the micelles were sphere-like (A_s<0.1). It is noted that the shape of micelles is not expected to be perfectly spherical. The radius of gyration of AF micelles varied from 3.2 to 4.1 nm, with the mean value of 3.6 nm.

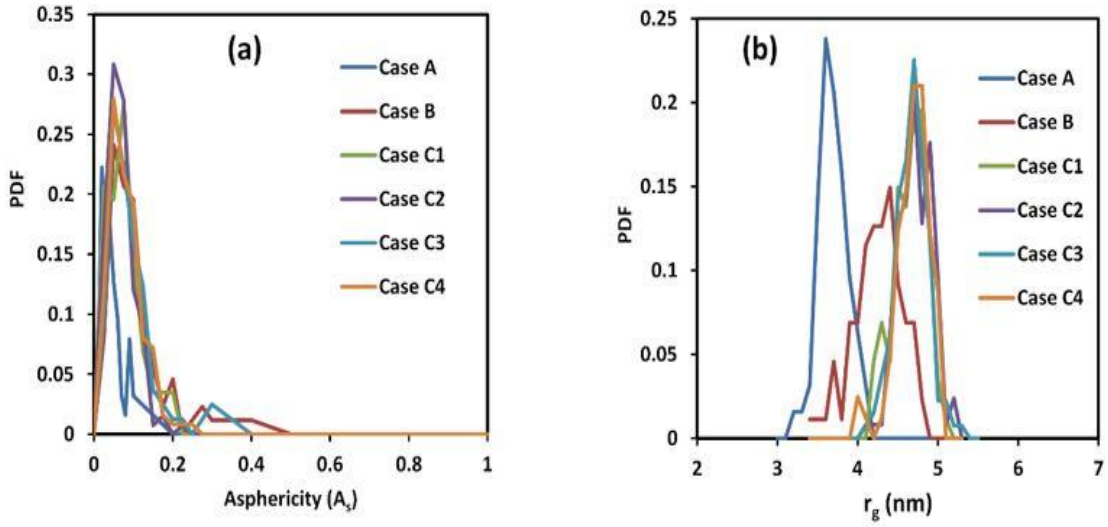

Figure 5.4. Distribution of asphericity (a) and radius of gyration (b) of surfactant micelles in water.

Similarly, 2 wt% of TG surfactant (simulation case B) was also reproduced in DPD simulation (see Figure 5.2(b)). Most of TG molecules also form a micelle in water. The change of free TG monomer concentration at different total surfactant concentration, plotted in Figure 5.3(b), was used to determine its CMC value. It was found to be 1264 ppm. According to the data of the TG producer (Dow Chemical), its CMC is 1314 ppm. The difference in CMC is smaller than the difference between simulations and experiments for AF (it is 3.8%). Additionally, the aggregation number of TG was quite small (average of N_{ag} =9.64, see Figure 5.3(b)). This is due to the long hydrophilic head (40 EO groups) of TG. Experimentally, Becher has determined the value of N_g for non-ionic surfactants with different number of EO groups (the length of the tail has the same composition as TG) [142]. So, average of N_{ag} for TG was around 10 by extrapolating the data in reference [142]. The value of N_{ag} strengthened the assumption that our DPD model could duplicate the structure of TG in water. In addition, the size and shape of the TG micelles were also quantified via asphericity and radius of gyration (see case B of Figure

5.4). It is noted that the last hydrophilic bead (bead H) on a tail of TG was used to calculate its asphericity and radius of gyration. The values indicate that most of TG micelles had spherical shape (A_s of TG varied from 0 to 0.31). The reason for this is that the aggregation number N_{ag} of TG micelles is rather small. The total size of a TG micelle was larger than an AF micelle. The radius of gyration of TG micelle varied from 3.2 to 4.8 nm with the mean value of 4.20 nm.

b. Binary mixture of AF and TG surfactants in water

The mixtures of AF and TG at different molar ratio in water were also studied at room temperature. All simulation cases are shown in Table 5.2. The asphericity calculations for simulation cases C1, C2, C3 and C4 (Figure 5.4(a)) indicate that the shape of micelles including both AF and TG was spherical. Hence, we can conclude that the shape of mixed micelles does not depend on their molar ratio at low concentration.

Table 5.2. CMC and average radius of gyration of micelles for binary surfactant system.

case	Wt% (AF)	Wt% (TG	Molar ratio	CMC (ppm)	$<r_g>$ (nm)
C1	0.8	2.1	1:1	107	4.6
C2	0.78	4.1	1:2	57	4.7
C3	1.6	1.04	4:1	100	4.6
C4	3.1	1.04	8:1	117	4.6

For the size of mixed micelles, it is seen that the average value of radius of gyration ($<r_g>$) was moderately increased relative to the size of single surfactant micelles. The distribution of r_g is from 4 to 5.5 nm (see Figure 5.4(b)). The mechanism creating micelles with mixed surfactants in water environment is similar to that for individual surfactants. Hydrophobic tails of both AF and TG can aggregate in order to form a micelle. In each micelle, the amount of AF and TG was related to the molar ratio of AF and TG (see Figure

5.5).

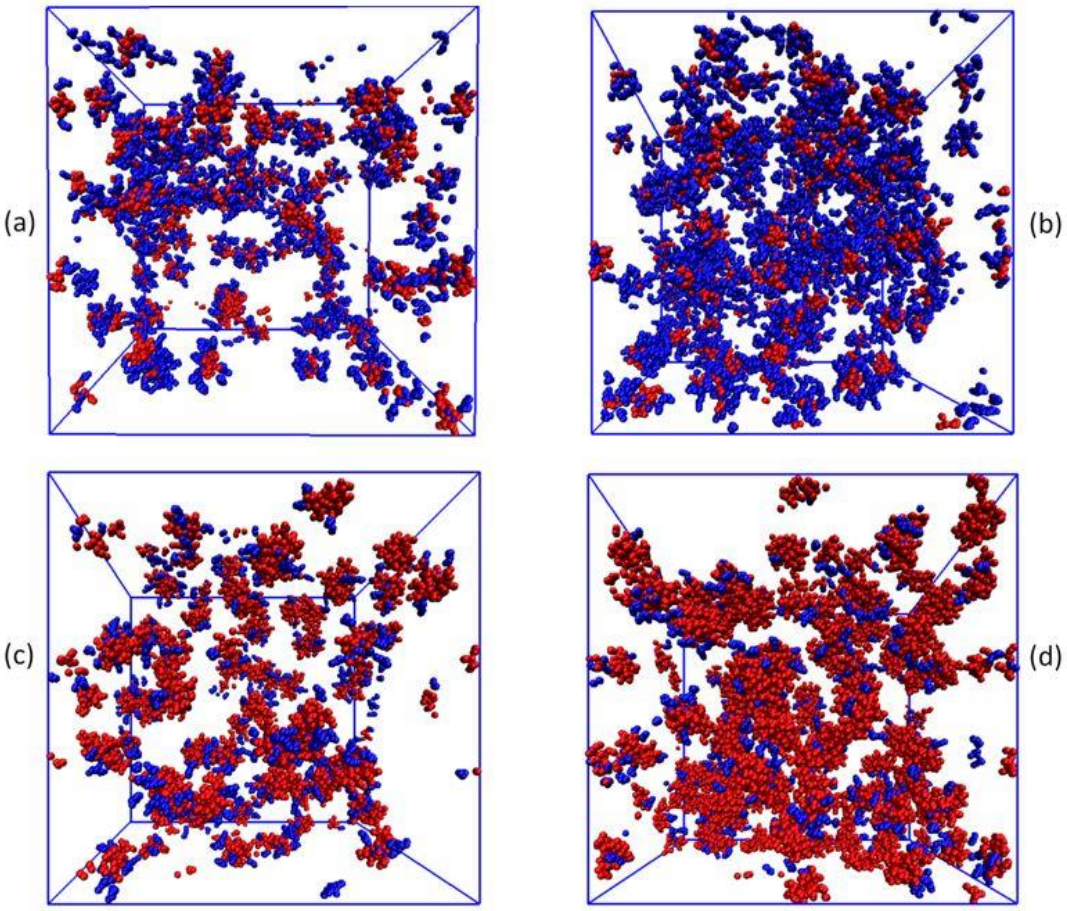

Figure 5.5. Snapshots of mixture of AF and TG in water in equilibrium. Red and blue dots are AF and TG beads, respectively. Each AF molecule has 4 beads while the TG molecule includes 8 beads. (a) Simulation case C1 (b) Simulation case C2; (c) Simulation case C3; (d) Simulation case C4

In terms of CMC, it was observed that all free surfactants in the binary AF/TG system were only AF molecules. Almost all small TG aggregates (that could be otherwise considered as free monomers) were filled in by some AF surfactant molecules. Because of this, the CMC of the binary system was close to the CMC of AF in water. For simulation case C2, the CMC dropped to 57.4 ppm. This is because of the high molar fraction of TG in this case (see Figure 5.5 (b)). For ideal mixed surfactants, the CMC of

binary surfactants can be predicted by Clint's equation as follows [143]:

$$\frac{1}{CMC} = \frac{\alpha}{CMC_1} + \frac{1-\alpha}{CMC_2} \tag{5.6}$$

where α is the mole fraction of surfactant 1; CMC, CMC_1 and CMC_2 are the critical micelle concentration of the mixture, pure surfactant 1 and pure surfactant 2, respectively. In Equation 5.6, the activity coefficient of surfactants 1 and 2 was assumed to be unity. It means the interaction between the two surfactants was ideally considered to be similar to the interaction of the same kind of surfactant. The CMC of mixed surfactants (AF and TG) from DPD simulation and from ideal solution theory can be found in Figure 5.6.

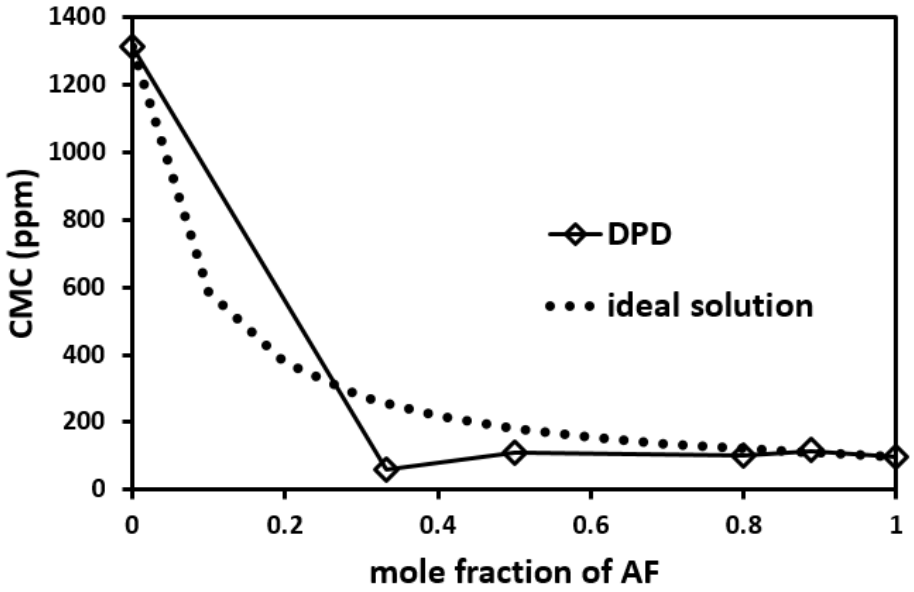

Figure 5.6. The CMC of AF/TG system at different mole fraction of AF from DPD simulation and ideal solution theory.

The simulation findings indicate a deviation from the ideal surfactant mixture assumption. This difference is the result of the differences in the interaction among beads of AF and TG in our simulation. The interaction of AF and TG is different from the self-interaction (AF – AF, or TG – TG). Basically, anionic and non-ionic surfactants have different chemical structure, so that their binary system could not be considered to behave

like an ideal solution. The CMC deviation of mixed surfactant of AF and TG in water is therefore not surprising. The same tendency has also been observed in the experiment of Akbaş et al. to measure the CMC of the surfactant system including dodecyl sulfate-polyoxyethylene-23-lauryl ether and sodium chloride solution in water at 25°C [144].

c. The adsorption of anionic and non-ionic surfactants on the CNT

To study the adsorption of the surfactants on the surface of CNTs, an infinitely long CNT is built and placed at the center of the simulation box. The diameter of the CNT was 10 nm, as already mentioned in Section II. The percentage of adsorption was defined as the ratio of adsorbed surfactant molecules and the total number of the same surfactant molecules in the system. It represents the relative distribution of surfactant on CNT surface vs. in solution. The CMC was based on the amount of free surfactants that were not adsorbed on the surface of CNTs. All simulations were run up to $5x10^6$ time steps.

In Figure 5.7 we present the whole adsorption process of AF on CNT at different times. In our simulation, AF molecules were only allowed to diffuse after water in the system reached equilibrium (i.e., the temperature of the system was constant). Initially, individual surfactant molecules were adsorbed on the surface of the CNT when they moved close enough to the CNT (within the range of the cut-off radius). At the same time, other surfactants agglomerated to form small micelles. This means that the surfactant molecules dispersed under the effect of two processes: forming micelles in solution and adsorbing on the CNT. These processes occurred spontaneously and competed with each other. The adsorption of surfactants is based on the attraction of the hydrophobic tails and CNT. Eventually, surfactants accumulated and re-arranged on the CNT surface. Micelles with low N_{ag} could also be adsorbed on an occupied surface, while a big micelle (high

N_{ag}) was difficult to attach on the CNT surface after it was formed in the bulk.

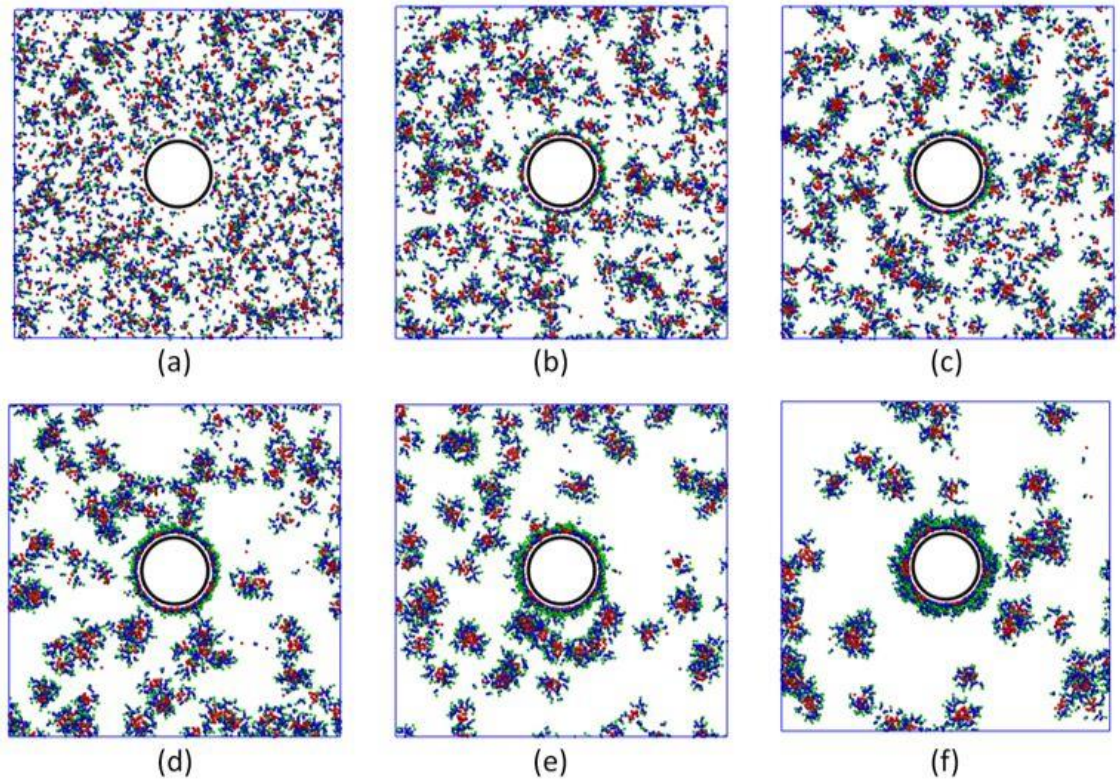

Figure 5.7. Snapshots of the adsorption of AF molecules on the CNT surface in top view. All water beads were removed for clarity. Red, blue, green beads are C, N and S beads of AF molecules, respectively. Black beads are CNT. (a) At 10 ps; (b) At 50 ps; (c) At 100 ns; (d) At 50 μs; (e) At 0.1 ms; (f) At 0.24 ms.

There are two reasons for this: first, a high N_{ag} micelle has hydrophilic heads on its outer surface, while the CNT surface is hydrophobic. They are unlike each other. Second, hydrophilic heads of adsorbate surfactants orient outward from the CNT surface (see Figure 5.7(a) and 5.7(b)) after surfactant molecules form a cluster on the surface. The adsorption of surfactants makes the CNT surface to become more hydrophilic. It would repel other surfactant micelles that try to move close to the CNT surface. So, our DPD results show that adsorbed surfactants form a single layer on the CNT surface. The rate of adsorption was high at earlier times and decreased rapidly after that. When the amount of adsorbate surfactants on the surface was almost constant, the adsorption could be

considered to reach equilibrium. For TG, the mechanism was similar to the adsorption of AF. In water, the adsorption mechanisms of anionic and non-ionic surfactants on the CNT surface were similar. Adsorption basically relied on the attraction of the hydrophobic tail of the surfactant and the surface.

Table 5.3. The adsorption properties of AF and TG on CNT surface.

Surfactant	Wt%	Case	% adsorption	CMC (ppm)	$\langle r_g \rangle$ on CNT(nm)
AF	1	D1	74.3	92	3.1
	2	D2	46.8	91	3.2
	4	D3	22.6	108	3.2
TG	1	E1	57.5	310	3.5
	2	E2	37.9	516	3.4
	4	E3	22.5	633	3.5

The percentage of AF and TG adsorption decreased with increasing AF concentration (Table 5.3). It means that the ratio of adsorbed surfactant molecules compared to the total surfactant molecules was reduced, indicating that the adsorption was limited by the surface area of the CNT. The amount of adsorbed surfactant could not increase any more when the surface was saturated, since this was monolayer adsorption. Therefore, increasing initial concentration of surfactant did not affect the maximum coverage of the CNT surface. This is why the percentage of adsorption with higher concentration of surfactant was reduced. At 1 and 2 wt%, the adsorption of AF on the CNT surface was higher than that of TG. This finding can be explained because TG has many hydrophilic EO groups (40) on its head. It is less preferable for TG to adsorb on the CNT than it is for AF molecules. However, the percentage of adsorption of AF and TG was similar when the surfactant concentration was at 4 wt%. This might be explained by small TG

aggregates that have a higher probability to adsorb on CNT, when the number of TG molecules in the system and around the CNT grows.

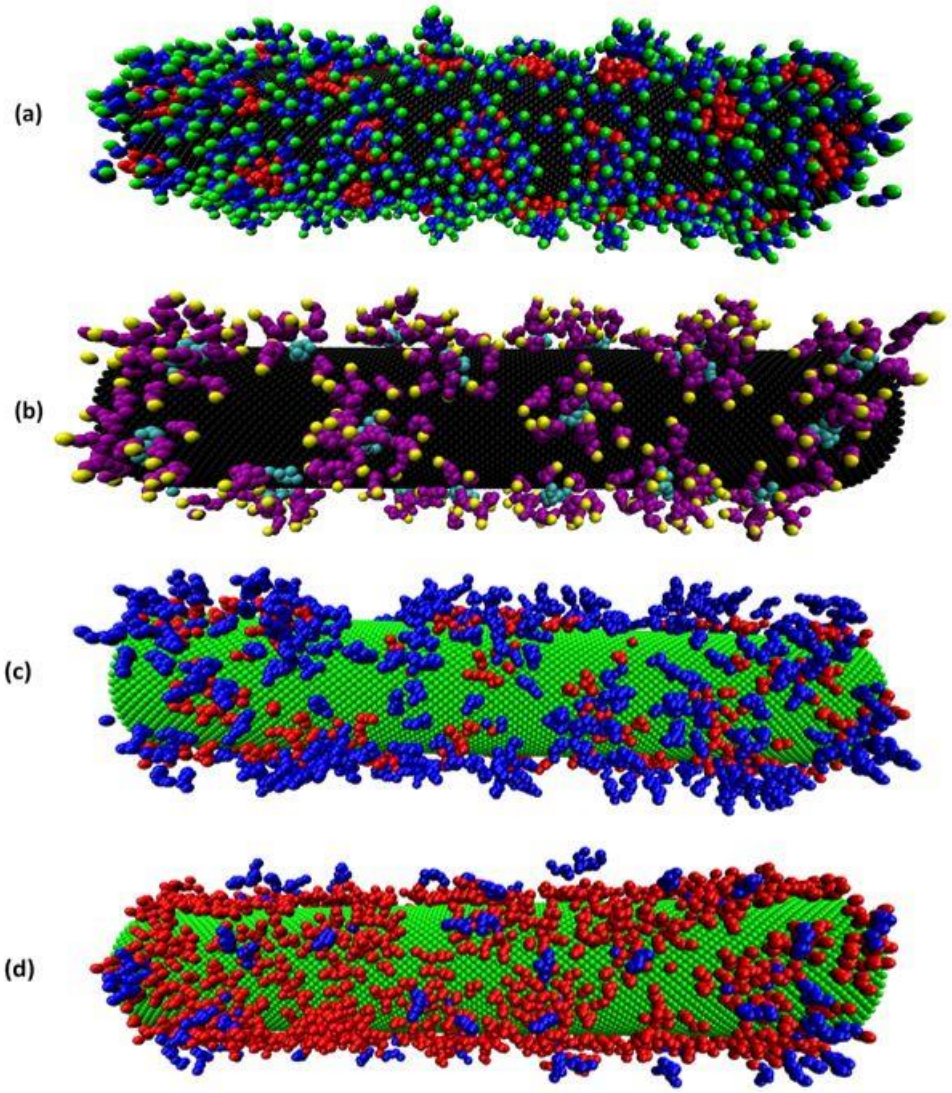

Figure 5.8. The distribution of surfactant on CNT surface. All water beads were removed for clarity. (a) Simulation case A; (b) Simulation case B. Red, blue, green beads are C, N and S beads of AF molecules, respectively. Cyan, purple, yellow beads are E, O and H beads of TG molecules. Black beads are CNT. (c) Simulation case F2; (d) Simulations case F4. Red, blue, green beads are AF, TG and CNT, respectively (see Table 5.5 for the condition of simulations F2 and F4).

The CMC of surfactants in solution was also determined and is presented in Table 5.3 for the cases when a CNT was present. For AF, the CMC at different concentrations was

similar to its CMC in water. With low CMC of extended surfactants [139] and high average N_{ag}, like AF, the adsorption on the CNT did not affect strongly the number of free monomers in solution. On the contrary, the CMC was significantly reduced in the presence of CNTs for TG. The adsorption of surfactant on the CNT surface was based on the hydrophobic-hydrophobic attraction between surfactant tails and CNT surface. The amount of hydrophilic heads on micelles is proportional to their N_{ag}, so that high N_{ag} micelles were more hydrophilic in an aqueous environment. So, it was more difficult for large micelles to adsorb on the CNT surface rather than free monomer surfactants or small micelles. A lot of free TG surfactant monomers preferred to move close to the region around the CNT and be adsorbed on it. This phenomenon could lead to reduced CMC for TG when adsorption on the CNT surface occurred.

In terms of morphology of the adsorbate surfactant, Figures 5.8(a) and (b) are depictions of the arrangement of AF and TG on the CNT surface. It is observed from our simulations that almost all AF and TG molecules tend to form aggregates on the surface. A few single surfactant molecules were distributed arbitrarily among these surfactant clusters. It has been observed in published reports that the distribution of surfactants on CNT could be the result of random adsorption [145], encapsulation in a cylindrical micelle [146], hemimicellar adsorption [147] and micelle adsorption [148]. Depending on many factors, the shape of the surfactant on the surface belongs to one of these four categories. To quantify the shape of surfactant clusters on CNT, the sphericity (S_p), defined as the ratio between surface area of a sphere of the same volume as the object and its surface area, was computed as follows [149]:

$$S_p = \frac{\pi^{1/3}(6V_o)^{2/3}}{A_o} \tag{5.7}$$

where V_o and A_o are volume and surface area of the object. The sphericity is independent of the size of an object. It has the value of 1 for a sphere, but for any non-spherical object S_p is less than 1. The sphericity of different shapes is listed in Table A1 in the Appendix A1. The distribution of sphericity of all AF and TG aggregates on the CNT surface is also presented in the Figures 5.9(a) and 9(b). S_p varies from 0.50 to 0.85 with the mean value of 0.79. On the CNT surface, each aggregate of both AF and TG has tails in the middle and hydrophilic heads oriented towards the bulk solution. The aggregates look like parts of a half-sphere covered on a surface. This type of aggregate can be called a hemimicelle. The average size of hemimicelles is 3.151 and 3.470 nm for AF and TG, respectively. Comparing to the size of micelles in water, the size of aggregates of surfactants on the surface was smaller than in the bulk solution.

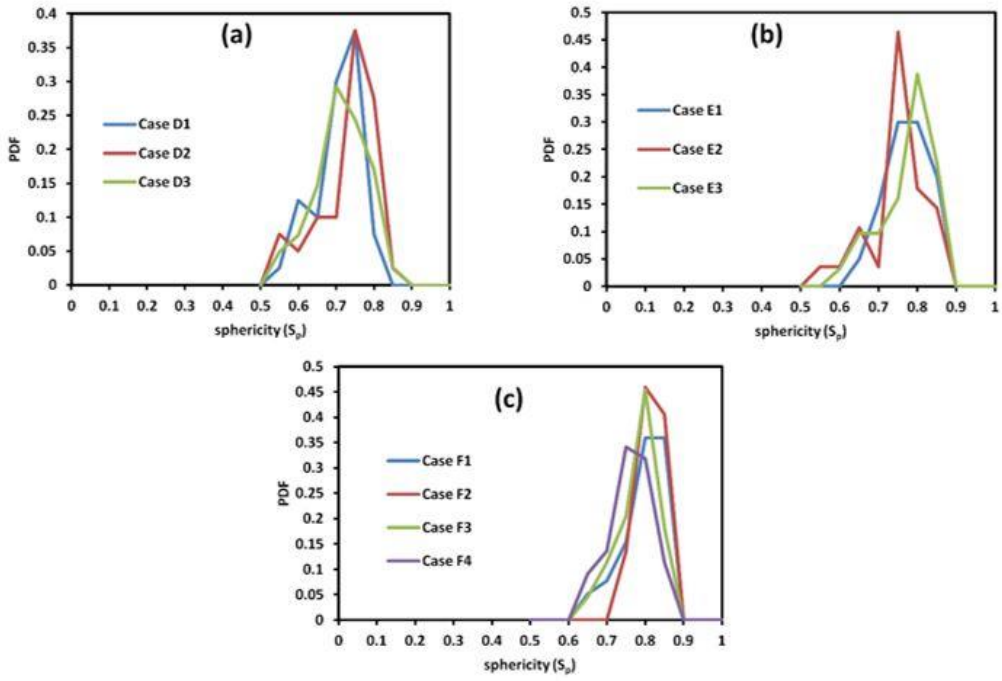

Figure 5.9. The distribution of sphericity of hemimicelle surfactant on CNT. (a) AF surfactant; (b) TG surfactant; (c) Binary surfactant system (AF/TG). See Table 5.5 for the conditions of simulations F1 – F4.

The maximum adsorption density of a surfactant on the CNT surface is another important characteristic that was considered in our calculations. It is seen in Figure 5.9 that there were still available spaces on the CNT surface for surfactant adsorption, even though the system reached equilibrium. The CNT surface became more hydrophilic due to surfactant heads on it. Surfactant micelles in solution were repelled when moving close to its surface. It is observed that only free surfactants, or low N_{ag} micelles, had a high probability to adsorb on unoccupied CNT surface at this time. Hence, a procedure to count the maximum adsorption in our simulation (see Figure 5.10) is as follows:

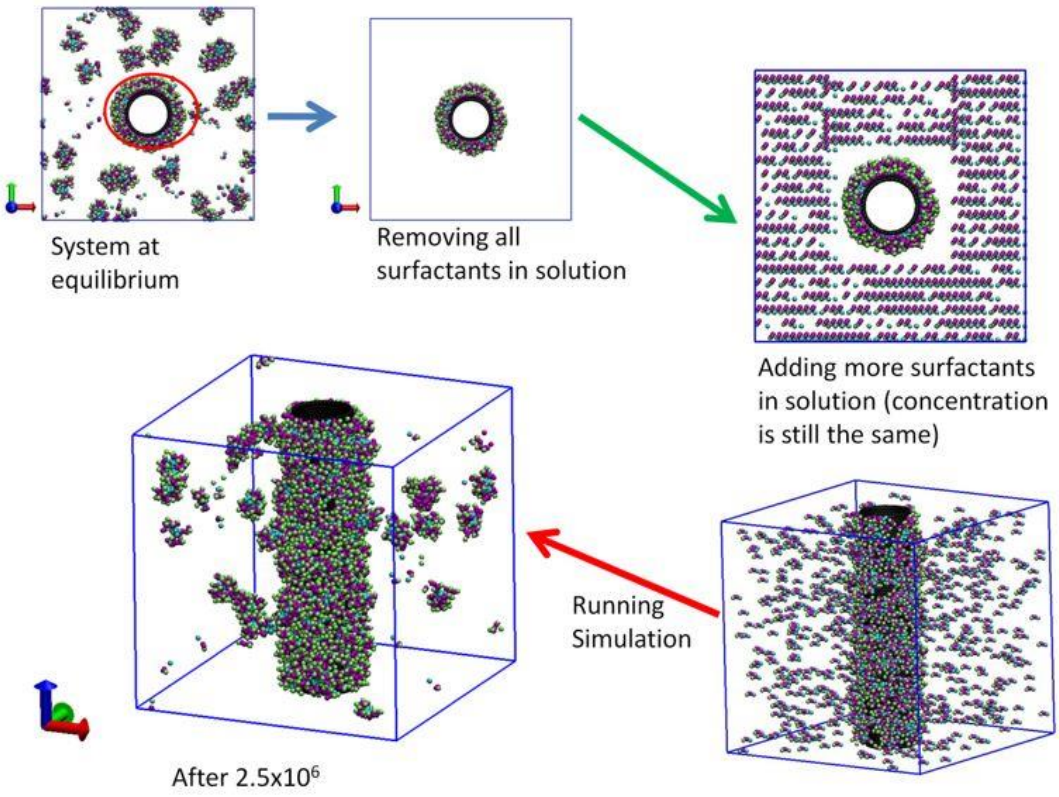

Figure 5.10. The procedure to get the maximum adsorption density of surfactant. All water beads are removed for clarity. Cyan, purple, green and black beads are C, N, S and CNT beads of AF molecules, respectively.

At equilibrium state, all of surfactants (either formed in micelles or as free monomer surfactants) in the bulk solution were removed from the simulation box. Only adsorbate

surfactants were kept in the simulation box. New free surfactant molecules, equal to the number of the removed molecules, were released into the solution. The new system with the new configuration was run until it reached equilibrium again (the run was for about $2.5x10^6$ additional time steps). The physical equivalent of this numerical procedure is to imagine that the CNT solution underwent a filter that removed surfactants in the bulk. Then it was released into a new surfactant solution with the concentration of the whole system being the same. The procedure was repeated until the difference of adsorption density was less than 5%. Table 5.4 gives results of AF and TG adsorption density on CNTs from DPD simulation. The maximum adsorption for AF and TG was 0.72 and 0.27 molecules/nm^2, respectively. Additional calculations were carried out to determine the average value and the standard deviation for each data point reported on Table 5.4. Different initial seed numbers were generated and 7 simulations were run to generate different random realizations.

Table 5.4. Adsorption density of AF and TG. Average values and the range of one standard deviation are reported.

Surfactant	case	Number of adsorbate molecules	Adsorption density (molecule/nm^2)
AF*	D2	932 ± 38	0.6
	D2a	1018 ± 11	0.6
	D2b	1108 ± 7	0.7
	D2c	1132 ± 13	0.7
TG**	E2	360 ± 8	0.2
	E2a	389 ± 5	0.2
	E2b	417 ± 2	0.3
	E2c	422 ± 2	0.3

* For AF, the sequence of running the simulation cases was D2 → D2a → D2b → D2c.
** For TG, the sequence of running the simulation cases was E2 → E2a → E2b → E2c.

d. The adsorption of a binary surfactant (AF and TG)

The adsorption of binary surfactant (AF and TG) on CNT was also evaluated to study the effect of anionic and non-ionic surfactant on the shape and size of mixed surfactant aggregates. In Figure 5.11 we display the adsorption of binary surfactants with molar ratio 1:1 at different times. It is seen that the mechanism of binary surfactant adsorption on the CNT surface is primarily similar to that of individual surfactant adsorption. The driving force of the adsorption also comes from the attraction of hydrophobic surfactant tails on the CNT. AF and TG can approach the surface and adsorb as individual molecules, or form a mixed micelle and aggregate on the CNT.

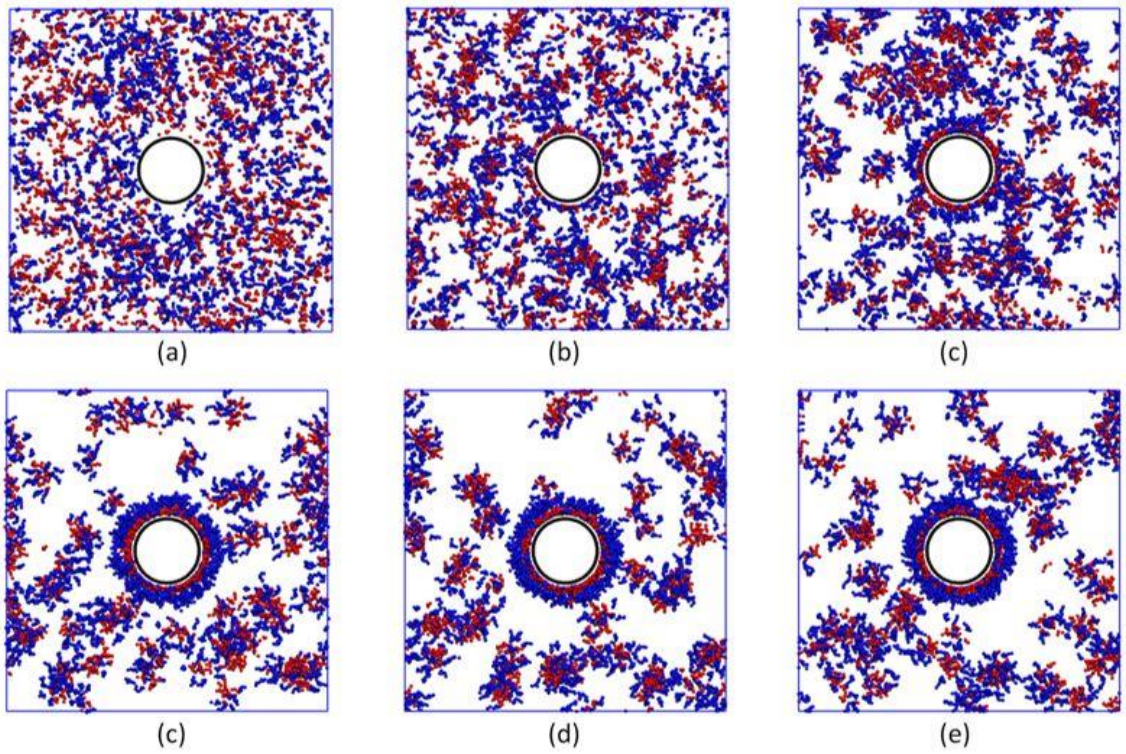

Figure 5.11. Snapshots of the adsorption of mixture of AF and TG (1:1 molar ratio) on CNT surface in top view. All water beads were removed for clarity. Red, blue, black beads are AF, TG and CNT, respectively. (a) At 10 ps; (b) At 50 ps; (c) At 100 ns; (d) At 50 μs; (e) At 0.1 ms; (f) At 0.24 ms.

In the mixture of AF and TG, the hydrophilic property of the CNT surface is supported

by their head groups. The outside of this hydrophilic layer is EO groups of TG and sulfate groups of AF that stand next to each other. The molar ratio of AF and TG on the CNTs, shown in Table 5.5, implies that AF was more favorable to adsorb than TG. However, TG makes the CNT surface to be more hydrophilic because of the number of EO head groups on its molecules. In addition, TG creates a steric repulsion on the CNT surface. This steric effect is a really important factor that results in the stabilization of CNTs in solution. For adsorptive surfactants, the presence of CNTs slightly decreased the CMC of the binary surfactant system (see Table 5.5). But the trend of CMC at different molar fractions could be considered to be an analogous case to the binary surfactant in water.

Table 5.5. The adsorption properties of binary surfactants on the CNT surface.

Case	Initial molar ratio	Molar ratio on CNT	CMC (ppm)	$\langle r_g \rangle$ on CNT (nm)
F1	1:1	1.16:1	80	3.3
F2	1:2	1.11:2	49	3.4
F3	4:1	4.77:1	110	3.2
F4	8:1	9.20:1	98	3.3

With regard to the morphology of binary surfactants on the CNT surface, the shape and size of their aggregates are almost identical to the case of single surfactant adsorption. The sphericity values of simulation cases F1, F2, F3, F4 changed from 0.60 to 0.85 (see Figure 5.9(c)). These results suggest that binary surfactants form hemimicellar aggregates adsorbed on the CNT. Actually, there also existed a few surfactants that were randomly adsorbed. Most of adsorbed surfactants agglomerated, however, into hemimicelles on the surface. The average radius of gyration of binary surfactant hemimicelles on CNT in Table 5.5 is nearly equivalent to that AF or TG adsorption (Tables 5.3). It seems that using both anionic and non-ionic surfactants did not influence the shape and size of

aggregates on the CNT surface.

Table 5.6. Diffusivity of AF and TG in all studied cases. Average values and the range of one standard deviation are reported.

Case	Diffusivity on CNT surface (m^2/s $x10^{-12}$)		Diffusivity in solution (m^2/s $x10^{-11}$)		
	AF	TG	AF	TG	From Stoke-Einstein equation
A	--	--	1.67 ± 0.29	--	6.74 ± 0.35
B	--	--	--	1.19 ± 0.08	5.84 ± 0.43
C1	--	--	1.14 ± 0.08	1.14 ± 0.08	5.33 ± 0.24
C2	--	--	1.08 ± 0.09	1.08 ± 0.09	5.25 ± 0.23
C3	--	--	1.23 ± 0.08	1.23 ± 0.08	5.31 ± 0.23
C4	--	--	1.19 ± 0.14	1.19 ± 0.14	5.29 ± 0.24
D1	2.94 ± 0.51	--	1.41 ± 0.13	--	7.40 ± 0.62
D2	2.23 ± 0.36	--	1.46 ± 0.17	--	7.40 ± 0.47
D3	1.07 ± 0.40	--	1.54 ± 0.21	--	6.76 ± 0.58
E1	--	6.90 ± 2.99	--	1.17 ± 0.57	5.97 ± 0.37
E2	--	4.53 ± 0.73	--	1.19 ± 0.14	5.87 ± 0.31
E3	--	1.58 ± 1.03	--	1.08 ± 0.16	5.80 ± 0.31
F1	1.78 ± 0.52	0.91 ± 0.49	1.04 ± 0.09	1.04 ± 0.09	5.71 ± 0.25
F2	1.17 ± 0.63	0.71 ± 0.53	0.84 ± 0.08	0.84 ± 0.08	5.53 ± 0.30
F3	1.80 ± 0.67	1.09 ± 0.66	1.00 ± 0.14	1.00 ± 0.14	6.13 ± 0.36
F4	1.19 ± 0.37	0.78 ± 0.29	0.96 ± 0.08	0.96 ± 0.08	5.98 ± 0.38

"--": No available value.

e. Diffusivity of surfactants

It has already been mentioned that the mechanism of adsorption of surfactants on the CNT involves first adsorption to the surface and then self-assembly to mainly hemimicellar aggregates for both surfactant systems. This process involves surface diffusion of the surfactants on the CNT surface. The diffusivity was calculated from the

slope of the mean squared displacement curve of all molecules with respect to time (see the Appendix A2 for individual plots). The position of a surfactant was assumed to be the center of mass of the whole molecule. We present in Table 5.6 the diffusivity of AF and TG on CNT surface and in solution for all simulation cases. The slope of the mean squared displacement vs time was computed by using $1.5x10^6$ time steps to obtain the slope. The process was repeated 7 times, every $0.5x10^6$ time steps, to obtain the mean value and the standard deviation of the diffusivity, reported in Table 5.6.

For the system including surfactant and water, the diffusivity of AF was higher than TG (compare simulation cases A and B). In the binary surfactant system, AF and TG had the same diffusivity (as seen for simulation cases C1, C2, C3 and C4). This finding can be explained by considering that both of them form a mixed micelle and diffuse by the same rate at equilibrium. Actually, there were also free surfactant monomers that move faster than a micelle. But the number of them was too small when compared to the number of total surfactant molecules that were in solution. It is found then that the diffusivity of the surfactant depends mainly on the propagation of its micelles.

After adsorption, the adsorbed surfactants could also diffuse on the CNT surface. It is noted that the CNT surface is non-charged in our DPD simulation. The attraction force between surfactant tails and a CNT only holds the surfactant on the CNT surface, so adsorbed surfactants still could exhibit surface diffusivity. Obviously, the diffusivity of surfactants on the surface was lower than in solution, due to the reduced degrees of freedom of surfactants adsorbed on the CNT. The surface diffusivity of surfactants was between 2 and 14 times smaller than the diffusivity in solution. It also depended on the amount of adsorbate surfactants on surface. The higher the concentration of adsorbate

surfactant, the lower its diffusivity was. For the binary surfactant adsorption, the diffusivity of AF and TG was the same in solution, while the surface diffusivity of AF was higher than that of TG on the CNT surface. This is expected since the chemical structure of TG is bulkier than AF. The steric effect of TG also reduced its mobility on CNT surface.

Comparisons of the calculated bulk diffusivities can be done with the Stokes-Einstein equation for the diffusivity of small particles at very low Reynolds numbers. According to the Stokes-Einstein equation, the diffusion coefficient of a spherical particle with radius R_s is given as

$$D = \frac{k_B T}{6\pi\mu R_s} \tag{5.8}$$

where: μ is the dynamic viscosity of the continuum medium. As discussed above, the shape of AF, TG, and binary AF/TG micelles in water is almost spherical. The average radius of gyration has been determined for all cases. Hence, it could be used as R_S to calculate the diffusivity of the surfactant micelles via Equation 5.8. However, the diffusivity from Stokes-Einstein equation is larger by 4 to 6 times than that from our analysis based on the mean square displacement of the molecules. For DPD coarse grained method, it has been shown that the diffusivity of the simulated fluid is over predicted.[67] Basically, each DPD water bead represents many water molecules instead of a single one. Hence, a fluid simulated with DPD exhibits a higher diffusion coefficient. However, the propagation of a particle in a DPD fluid is still maintained correctly. Spaeth et al. demonstrated that the diffusion coefficient of nanoparticle was in good agreement with the Stokes-Einstein relation.[150] Zhao and Wang proved that the diffusion of rigid rod-like polymer in DPD simulation also concurred with the Kirkwood theory in dilute

solution range.[151] Besides, Chen and co-workers also found that DPD results of the settling of a single sphere in a square tube was consistent with those from experimental data and lattice Boltzmann simulations.[76] So, the reduction of diffusivity of surfactant micelles might be caused by their interactions in solution rather than being artifacts of the DPD calculations. Another reason for the discrepancy between the Stokes-Einstein results and the computations could be the electrostatic interaction between micelles and the aqueous medium for ionic surfactants.[152, 153] (In our DPD simulation we have implicitly considered electrostatic interactions via adjusting the repulsion parameters of head groups and water, as already discussed.) It follows that the drag force acting on surfactant micelles could be stronger than the calculations of Equation (5.8).

5.4. Conclusions

We have demonstrated that a DPD technique can be used to simulate the characteristics of commercial AF and TG (anionic and non-ionic) surfactants suspended in an aqueous medium. Their CMC is the important property that was utilized to determine and validate the interaction parameters in our model. There is a good agreement between DPD results and experimental data for the CMC of the surfactants (within 10%). In addition, the other self-assembly properties (aggregation number, shape and size) of AF and TG micelles were determined to provide more details of the behavior of the surfactants in solution. Most of AF and TG micelles were spherical in shape with average r_g equal to 3.64nm and 4.20nm, respectively. For the binary (AF and TG) surfactant system, its CMC was found to be less than the value expected from the ideal solution theory. The mixed micelle surfactant including both AF and TG was also spherical.

Adsorption of each surfactant on CNT surfaces at room temperature was observed, and

both AF and TG formed a monolayer on the surface with mainly hemi-micellar assembly of the adsorbed surfactants and some random adsorption. The adsorbed surfactants preferred to agglomerate in shapes that look like parts of a sphere, rather than follow a random monomer distribution on the CNT surface. The maximum adsorption density of AF and TG on the CNT surface was 0.72 and 0.27 molecules/nm^2, respectively. For binary surfactant systems, the same adsorption mechanism was observed as for single surfactant adsorption. This mechanism is the result of the competition of the surfactant molecules to either form micelles in the bulk solution or adsorb on the surface. After adsorption, the surfactant molecules diffused on the CNT surface and aggregated by rearranging their orientation and forming hemi-micelles, where the hydrophobic CNT served in lieu of the other half of a micelle. These hemi-micelles continued to move on the CNT surface, but at a much slower rate, resulting in the stabilization of CNTs in suspension due to steric effects. The initial adsorption was driven by the hydrophobic – hydrophobic attraction between surfactant tails and the CNT surface. Both AF and TG could adsorb together and change the effective surface properties of the CNT from hydrophobic to hydrophilic, by forming a new particle with the CNT in the center and the hydrophilic heads of the surfactants on the outer surface. The outer surface of the resulting CNT particle was almost completely covered by the hydrophilic heads of AF and TG. Results from binary surfactant adsorption showed that AF is more favorable to adsorb on CNT than TG. Moreover, the size of the hemi-micellar surfactant aggregates on the surface is smaller than the size of the spherical micelles in the bulk solution.

Finally, the surface diffusion of surfactant on the CNT and the diffusivity in solution was quantified. According to these results, we can conclude that the diffusivity of AF is larger

than TG. On the CNT surface, surfactant diffusion depends on its concentration. For the binary surfactant system, the diffusivities became identical while the two surfactants formed micelles in the bulk solution, since the total diffusivity was dominated by the micelles. The diffusivity of absorbate surfactant was relatively smaller than adsorptive one.

Our findings can contribute to the understanding of the morphology of single and binary surfactant systems on hydrophobic surfaces for use in practical applications. This study could be extended to the investigation of other effects (e.g., temperature and salinity) on the adsorption of surfactants on the CNT surface, as well as to obtain adsorption isotherms for anionic and non-ionic surfactants. Furthermore, the results herein for CNTs could be extended to apply for other cylindrical or rod-shaped objects that have hydrophobic surface properties. While the DPD parameters used are specific for the CNT-water interactions, the behavior of ionic and non-ionic surfactants on hydrophobic surfaces would be expected to be similar to the behavior reported in this study.

Chapter 6. Surfactant adsorption and water behavior inside single-walled carbon nanotube

6.1. Introduction [§]

Carbon nanotubes (CNTs) have received a lot of attention both in fundamental studies and applications, because of their special thermal, mechanical, and electrical properties [154, 155]. They are allotropes of carbon in a cylindrical nanostructure with a length-to-diameter ratio that can be significantly large (up to millions) [156]. Basically, CNTs can be visualized as rolled up graphene layers forming a tubular structure. The hollow part of the structure, inside the CNTs, could be considered as a confinement space where certain compounds can enter [157]. Therefore, there are interesting possible applications for open-ended CNTs, such as gas adsorbents [158, 159], using them as molds to form one dimensional (quantum) systems [160, 161], place catalysts on them [162], or use them as molecular filters for water treatment [163]. Hence, the adsorption and diffusion of chemical species (like water, gases *etc.*) inside CNTs should be well-understood to design and support such applications.

The adsorption of chemical compounds inside CNTs has been verified with both experiments and simulations. Davis *et al.* used the internal surface of CNTs to immobilize proteins and enzymes [164]. It was revealed that CNTs could act as a benign host with an ability to encapsulate protein molecules within a protected environment. Fujiwara and co-workers investigated the adsorption of nitrogen and oxygen gases inside and outside single-walled CNTs (SWCNTs) by obtaining adsorption isotherms and X-ray diffraction

[§] Material in this chapter has been published in Minh Vo, Dimitrios V. Papavassiliou, Molecules, 2016, 21, 4, 500.

studies [165]. It was found that the hollow space inside the nanotubes exhibited stronger attraction than the interstitial channels created when CNTs formed bundles. Pan *et al.* showed the striking enhancement of producing ethanol from CO and H_2 by using Rh particles confined inside CNTs [166]. They reported experimental findings that the overall formation rate of ethanol inside CNTs was higher than that on the outside, even though the latter was much more accessible to CO and H_2. With respect to simulation studies, the flow of water through CNTs was investigated with molecular dynamics (MD) simulations [167-169]. It was found that the hydrophobic surface of the CNT interior gives a significant enhancement for water flow through it. The nano-sorption and mobility of water, tyrosol, vanilic acid, and p-coumaric acid inside smooth SWCNTs have been calculated with MD simulations [170]. Additionally, Arai *et al.* studied the self-assembly and polymorphic transition of surfactant in water within a nanotube (inner diameter of around 8.4 nm) by using dissipative particle dynamics (DPD) simulation [127]. They presented evidence of a cornucopia of polymorphic structures of surfactant assemblies on the inner nanotube surface.

In this chapter, we quantify the change of water behavior inside SWCNT in the presence of surfactant adsorption, and the ability of SDS to diffuse into SWCNTs of different size (inner diameter between 1 and 5 nm). The transport properties of water, such as diffusivity, residence time, and radial and axial density distribution profiles, with and without surfactant adsorption were examined. This study provides insights into the dynamics and morphology of water and surfactants in nano-confined structures.

6.2. Computational Details

A schematic representation of the coarse-grained model used in this report is presented

in Figure 6.1, where the model for SDS molecules, water, and the SWCNTs is presented. Five water molecules were grouped into one simulation bead. Then, the volume of a water bead (W) has to be around 150 $Å^3$ [128]. The number density of water (ρ) was set to a value of 3. Thus, the length scale (r_c) of the DPD simulation was 0.766 nm. For the surfactant molecule, its volume is about 410 $Å^3$ [171]. We can then consider a single SDS molecule to be equivalent to 3 water beads: two beads are tail groups (T) and another is head group (H). Two consecutive beads of SDS molecule were also connected by harmonic bond potential with the spring constant (k_s) equal to 100 k_BT/r_c^2.

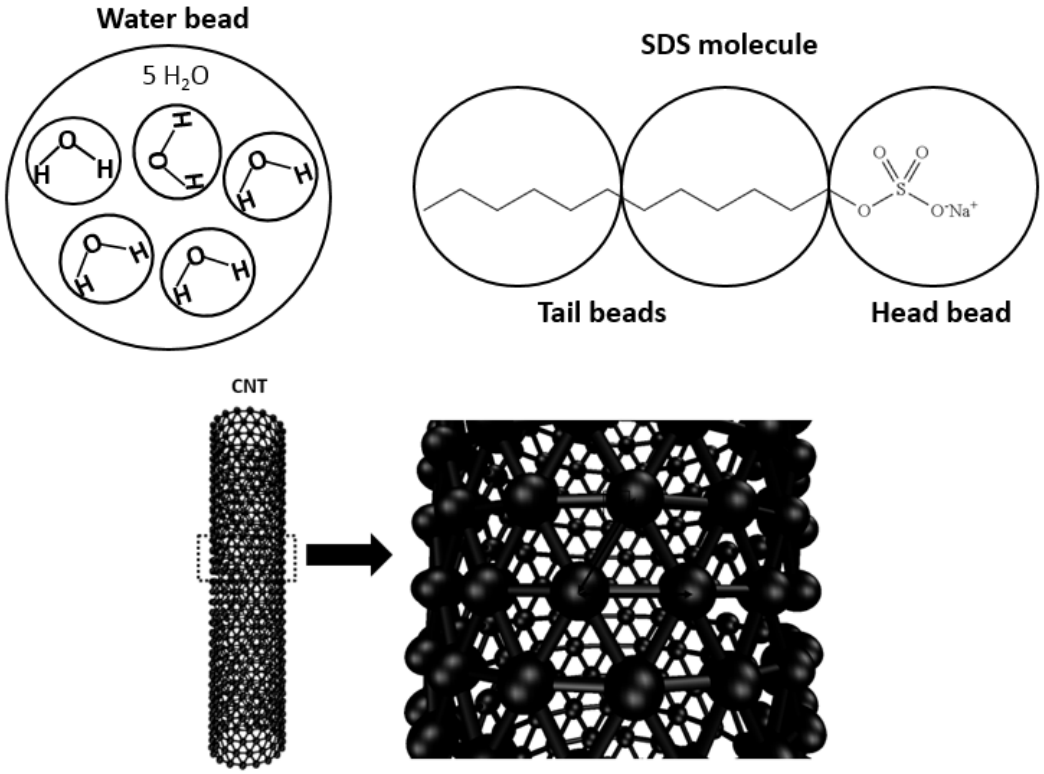

Figure 6.1. A schematic representation of the coarse-grained model for water, SDS surfactant molecule, and CNT in our DPD simulation. Each water bead represents five water molecules. The SDS molecule has three beads, including one head and two tail beads. For the CNT, the distance (h) between two nearest beads is 0.5 r_c.

The CNT was considered as a rigid hollow cylinder in our simulation. Since the objective of our study is to study the properties of water and surfactant inside open-ended CNTs, it

was not needed to have additional bonds and angular potentials among CNT beads. Additionally, Thomas and McGaughey proved that the structure of water inside the CNT is not affected by fixing the carbon atoms of CNT [172]. All CNT beads were arranged in an equilateral triangular lattice with nearest neighbor distance $h = 0.5r_c$ (see Figure 6.1). For simplicity, reduced units were used in DPD calculations. The temperature of the system was kept constant at reduced temperature $k_BT = 1$ (equivalent to 298 K). The pressure of the system was about 0.1 MPa. The canonical ensemble (NVT − constant-temperature, constant-volume) was also applied in all DPD calculations. The noise amplitude and friction coefficients were set to $\sigma = 3$ and $\gamma = 4.5$, respectively [52]. Additionally, all the simulations were carried out for 3×10^6 steps with a time step of 0.01 in reduced DPD units. The visual molecular dynamics (VMD) software was used to visualize all snapshots illustrated in this work.

Table 6.1. All repulsion parameters for water (W), CNT, and SDS beads in k_BT units. H and T represent head and tail beads of SDS molecule.

	W	**CNT**	**T**	**H**
W	25	60	80	15
CNT		25	25	40
T			15	80
H				35

Initially, positions of water and surfactant molecules were randomly distributed in the whole simulation domain. Once every 100 time steps, configurations of the whole system were saved for further analysis. The diffusion constant of water was used to determine the time scale in the DPD simulation [67]. The slope of the mean square displacement of water beads with time is equal to six times the water DPD diffusion constant (D_w), according to Einstein's diffusion theory. Thus, the time scale (τ) in our DPD simulation

was 0.044 ns. With respect to the repulsion parameter, we adopted results from published reports for DPD simulations [8, 52, 108, 133, 173]. A summary of all repulsion parameters applied in this manuscript is presented in Table 6.1. Note that electrostatic interactions were indirectly added into the DPD algorithm by choosing the repulsion parameters of head groups—water and tail groups—water [133]. In solution, surfactant could agglomerate together to form a micelle. In each aggregate, the hydrophobic tail assembled in the center (blue beads) and the polar head beads (orange) were on the outside (see Figure 6.2(a)). Water beads have a strong attraction to head groups and repel tail groups of SDS.

The SDS concentration in our report was higher than its CMC. From experiment, it is seen that CMC of SDS surfactant is around 8.1–8.4 mM (equivalent to 0.23 wt%) [174]. In our DPD calculation, CMC of surfactant was determined by counting the number of free molecules in the solution. Figure 6.2(b) showed the distribution of number of molecules in each micelle. If the number of molecules in any aggregate was lower than 5, it could consider as free surfactants. It was found that the CMC of surfactant in our DPD simulation is around 0.25 wt%. There is a good agreement between simulation and experimental data in terms of CMC.

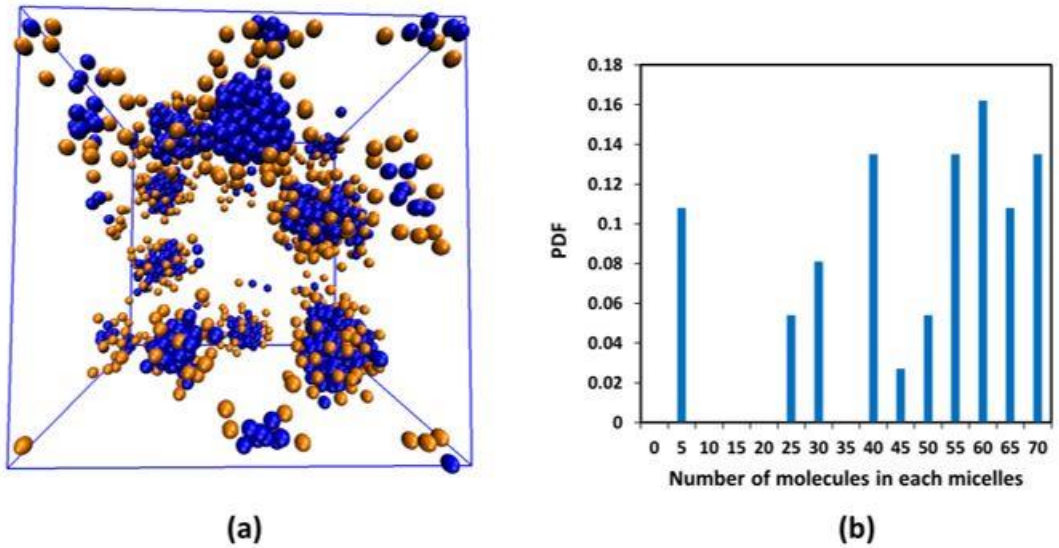

Figure 6.2. (**a**) The equilibrium snapshot of 2 wt% SDS in water. All of the water beads are removed for clarity. Blue and orange beads represent the tail and head beads of the surfactant, respectively; (**b**) the distribution of number of molecules in each SDS micelle in water.

6.3. Results and Discussion

a. The Diffusion of Water inside SWCNTs of Different Diameters

In this section, the distribution of water inside different diameters (d) of open-ended SWCNTs was investigated at room temperature. The chosen SWCNTs had armchair chirality and diameters of 1, 2, 3, 4 and 5 nm, corresponding to chirality indexes of (8, 8), (15, 15), (22, 22), (30, 30), and (37, 37), respectively. During the simulation runs, the SWCNTs were kept stationary at the center of the simulation box (box dimensions: 11.49 × 11.49 × 30.64 nm^3). All SWCNTs tested had the same length of 20 nm, irrespective of diameter. In Figure 6.3, we show the distribution of water beads inside different SWCNTs after the system reached equilibrium. Water beads were able to go into the hollow space in all cases of open ended SWCNTs in our simulation. In DPD simulations, the behavior of beads containing more than one molecule, or containing clusters of atoms within a molecule, like a monomer for polymer simulations, is simulated rather than the behavior

of individual atoms.

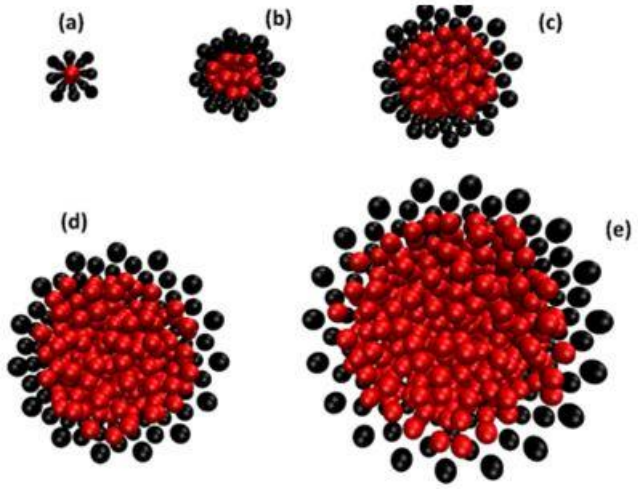

Figure 6.3. A snapshot at equilibrium (top view) of water beads inside an (8, 8) (**a**); (15, 15) (**b**); (22, 22) (**c**); (30, 30) (**d**); and a (37, 37) (**e**) SWCNT at 298 K. The CNT and water are shown in black and red beads, respectively.

In order to evaluate accurately the order of water inside each SWCNT, the radial and axial distribution profile of water inside different SWCNTs are presented in Figure 6.4. In our calculation, the number density of water was selected to be 3. For SWCNT (8, 8), it is seen that the water was ordered in a single-file chain (see Figure 6.3(a) and the purple line in Figure 6.4(b)). Individual water beads were arranged along the length of SWCNT with d = 1 nm. The axial distribution in Figure 6.4(b) indicates clearly the difference of water inside the SWCNTs and in the bulk phase. The center of the nanotube is at r = 0 in Figure 6.4(a), and the nanotube wall is at r = 0.5 nm, 1 nm, 1.5 nm, 2.0 nm, and 2.5 nm, depending on the SWCNT. For the d = 1 nm tube, there is a single density peak inside the nanotube and two distinct peaks outside the CNT.

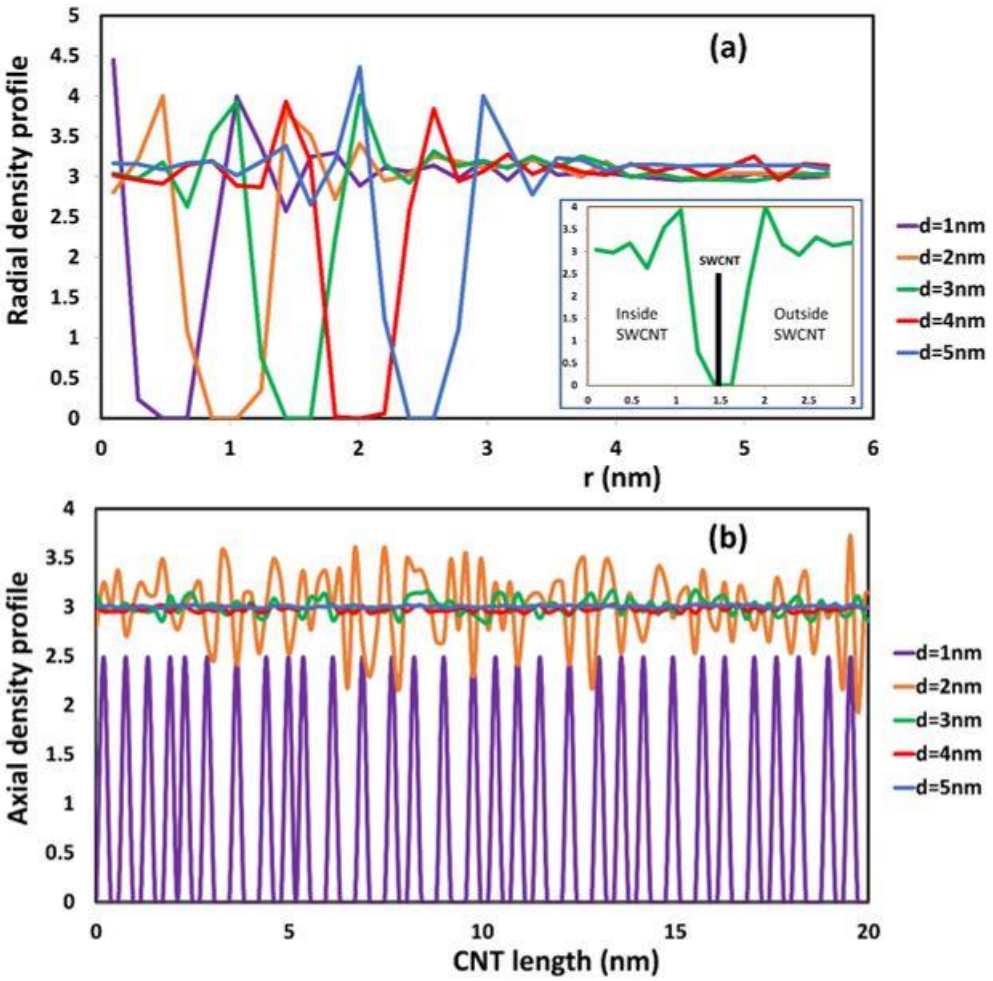

Figure 6.4. Radial (**a**) and axial (**b**) density profile of water inside different SWCNT in the equilibrium state. The inset plot in Figure 6.4(a) is an enlargement of the radial density profile with respect to distance (r) from 0 to 3 nm in the case of the SWCNT with diameter of 3 nm. The thick black line designates the position of the CNT wall. It is seen that the density profile to the right (exterior of the CNT) and to the left (interior of the CNT) is the same.

Along the length of the SWCNT, the axial density profile of water for the d = 1 nm nanotube is always below the density of water in the bulk phase, and it vibrates strongly from 0 to 2.5. The spacing between density peaks is rather even, and the peaks are periodic with periodicity of about 0.67 nm. This is an indication of the arrangement in a single chain of the water, as is also seen in Figure 6.3(a). In MD simulations, it has been shown that the configuration of water in SWCNTs of chirality (8, 8) was in stacked

pentagons [170]. In the present case, each water DPD bead represents five water molecules, instead of individual molecules, like in the MD simulation. However, the radial and axial density profiles from DPD and MD simulations are very similar.

For SWCNTs with $d \geq 2$ nm (see Figure 6.3(b–e)), the configuration of water beads inside the SWCNT is similar to that in the bulk phase. This observation is confirmed by the radial and axial distributions seen in Figure 6.4. For the larger diameter SWCNTs, as seen for example in the inset of Figure 6.4(a) for a SWCNT with $d = 3$ nm, the density profiles towards the inner and towards the outer side of the CNT wall appear to be almost symmetric. In MD simulation, it has been observed that the structure of water inside a SWCNT with $d > 2$ nm is bulk-like liquid behavior [172]. In the region close to the CNT surface, there is a peak of radial density that is higher than bulk density. This peak has often occurred in MD simulations for water molecules [73]. Beyond that point, the radial density oscillated around the bulk density both inside and outside of the CNTs. Along the length of the CNT, the density of water fluctuated around the bulk density of water. In other words, the density profile of water inside a CNT with $d > 2$ nm is the same as to that outside the CNT wall towards the bulk phase. These results and agreement with the MD results provide strong evidence that the mesoscopic DPD simulation can be used to study the transport of water inside confinement (like the interior of a CNT).

Other transport properties, like the diffusivity and residence time, can be used to characterize the behavior of water at the interior of the CNT structure. The mean squared displacement with respect to time was computed, and the slope of the line was used to determine the diffusivity of water beads inside the CNTs. The diffusion of water inside a CNT is almost the translation of water along the length of the CNT (z direction in our

simulation system). Hence, the diffusion inside a CNT can be viewed as 1-D diffusion. In Table 6.2, we give the average residence time and the diffusivity of water inside CNTs at different diameters. Note that the water diffusivity from our calculations is the average value for all water inside the CNT. It has been observed that the water diffusivity relies on its off-center distance [175]. It makes intuitive sense that inside the CNT, the diffusion of water beads close to the CNT surface is higher than in the center of the CNT. This is caused by the hydrophobic character of the CNTs. In order to give the general diffusion data, we take average of mean square displacement of all water beads inside CNT when calculating the diffusivity.

Table 6.2. Diffusivity and average residence time of water inside SWCNT.

Diameter of CNT and Chirality	Average Residence Time (ns)	Diffusivity of Water inside SWCNT (cm^2/s)	Diffusivity Ratio between Water inside SWCNT and in Bulk Phase (from Our DPD Simulation)	Diffusivity Ratio between Water inside SWCNT and in Bulk Phase (from MD Simulation) [175]
1 nm (8, 8)	57.1	1.27×10^{-5}	0.34	0.21
2 nm (15, 15)	26.3	2.53×10^{-5}	0.68	0.95
3 nm (22, 22)	18.6	3.91×10^{-5}	1.05	1.15
4 nm (30, 30)	17.9	3.86×10^{-5}	1.04	1.06
5 nm (37, 37)	18.3	3.77×10^{-5}	1.01	1.02

In our DPD calculations, the diffusivity of water in the bulk was calculated to be around 3.72×10^{-5} cm^2/s. This value is higher than the values for experimental diffusivity reported for water (2.43×10^{-5} cm^2/s). The reason for calculating higher water self-diffusivity arises from the fact that each DPD bead represents a group of several water molecules, instead of a single molecule [52]. Admittedly, our results might not give the exact numerical

value of the diffusivity, but they can give a comparative diffusion of water inside the CNT and in the bulk phase (see fourth column or results on Table 6.2). The diffusivity of water inside the CNT is about 34% of the bulk diffusivity for the (8, 8) SWCNT, then it increases to 68% of the bulk for the (15, 15) SWCNT and shows a maximum of being 105% of the bulk for the (22, 22) SWCNT. Then, for larger diameter SWCNTs it tends to go closer to the bulk diffusivity. These are results in agreement with results from MD simulations [175] (see fifth column or results on Table 6.2), where it was shown that the (20, 20) SWCNT exhibits the higher self-diffusivity of water inside the SWCNT and the (9, 9) the lower. The reason for the increase in diffusivity at higher diameters is that the hydrophobic properties of the CNT surface enhance the diffusion of water. Water is allowed to slip in adjacent regions close to the CNT surface. However, the diffusivity is also affected by the size of the confined space. It is more difficult for water to diffuse when the pore size is too narrow. Hence, the diffusivity of water inside SWCNT with diameter of 1 and 2 nm is smaller than that in the bulk phase. In terms of residence time, water took a longer time to pass through SWCNTs when the diameter of the SWCNT was reduced. Note that all SWCNTs have the same length (20 nm).

b. Can the SDS Molecules Enter the SWCNT?

In experiments, SDS has been used as a surfactant that can stabilize CNTs in an aqueous solution [176]. To determine the size of SWCNT that might allow SDS molecules to migrate and adsorb to the hollow interior of the nanotubes, simulations that included water, CNT, and SDS was performed with DPD methods. The total concentration of SDS in the system varied from 1 to 3 wt%. The simulation domain was 22.98 x 22.98 x 30.64 nm^3 with periodic boundary conditions in all three directions.

In Figure 6.5, we show the adsorption of SDS in different sized SWCNTs at equilibrium. The simulations showed that the SDS molecules cannot go inside the CNT if the diameter of CNT is equal or less than 2 nm. The driving force for surfactant adsorption inside the CNT is based on the attraction of the hydrophobic tail group and the CNT surface. The character of both the inner and outer surface of the CNT became more hydrophilic after the adsorption of the SDS took place. At the interior CNT surface, tails of surfactant self-assembled near to this surface and formed a monolayer. The orientation of SDS head groups were toward to the center of the CNTs.

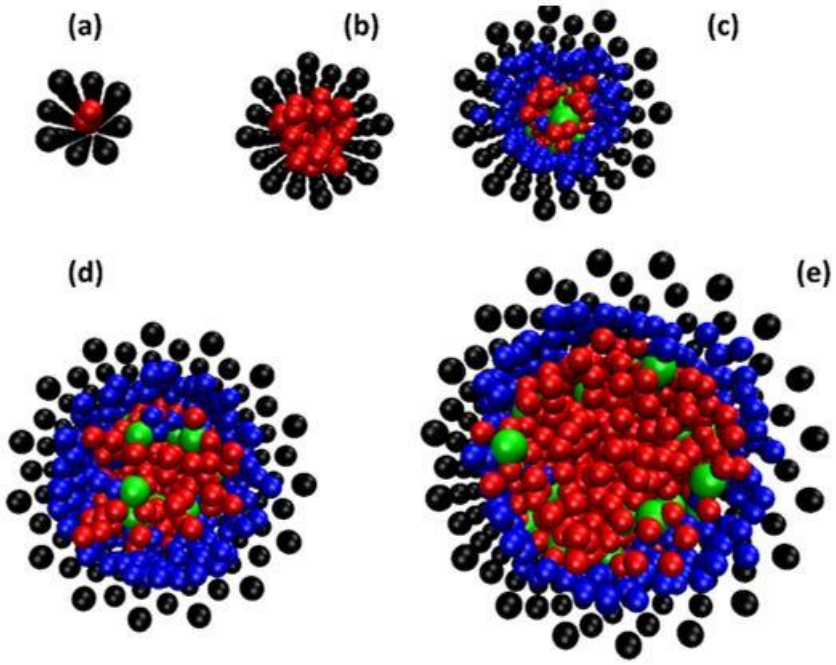

Figure 6.5. The equilibrium snapshot (top view) of SDS and water beads inside an (8, 8) (**a**); a (15, 15) (**b**); a (22, 22) (**c**); a (30, 30) (**d**); and a (37, 37) (**e**) SWCNT at 298K with total SDS concentration of 3 wt%. For SDS molecules, head and tail groups are shown in green and blue beads. CNT and water are in black and red beads, respectively. Note that the surfactant adsorption outside the CNT is removed for clarity.

We present in Figure 6.6 the side view of surfactant adsorption inside the SWCNTs. Differently than the exterior surface, surfactants inside the SWCNTs can only form a

random and hemi-micelle type of adsorption due to space limitations. Hemi-micellar adsorption has been observed on the exterior of multi-walled CNTs with nonionic and anionic surfactants in aqueous solutions with DPD and MD techniques [8, 124, 177]. Blue beads in Figure 6.6 indicate the tail groups of the surfactant adsorbed inside the SWCNTs. It was also seen that once the surfactant was adsorbed inside the SWCNT, it was unable to desorb from surface. Only water beads can enter and pass through the SWCNT.

The ability of SDS to enter the SWCNT is affected by the competition with water beads and by its molecular size. In the SDS-water system, surfactant molecules have to compete with water beads that can easily enter the SWCNTs. For a single molecule, the size of SDS is larger than water. Additionally, the hydrophilic heads of surfactant attract water beads (hydration process). This leads to a further increase of the size of SDS molecules. Therefore, water beads can enter the narrow space of a SWCNT easier. Another factor that needs to be considered is that the surfactant prefers to form a micelle rather than remain as a free surfactant molecule in solution. In all cases in this report, the total concentration of surfactant is higher than its CMC, meaning that both micelles and free surfactants are present in the simulation domain. In our study (the diameter of SWCNTs is less than 5 nm), we observed that only free surfactant molecules can enter and adsorb in the interior of the SWCNT surface. For SDS micelles, their outside is covered by the hydrophilic head groups of the surfactants. These micelles are more difficult to adsorb on the CNT surface due to repulsion forces (hydrophilic head groups and hydrophobic CNT surface). Therefore, SDS micelles favor propagating into the bulk water phase. For low SDS concentration (smaller than CMC), the surfactant only adsorbs on the exterior surface of the CNT where the adsorption can take place more easily and favorably.

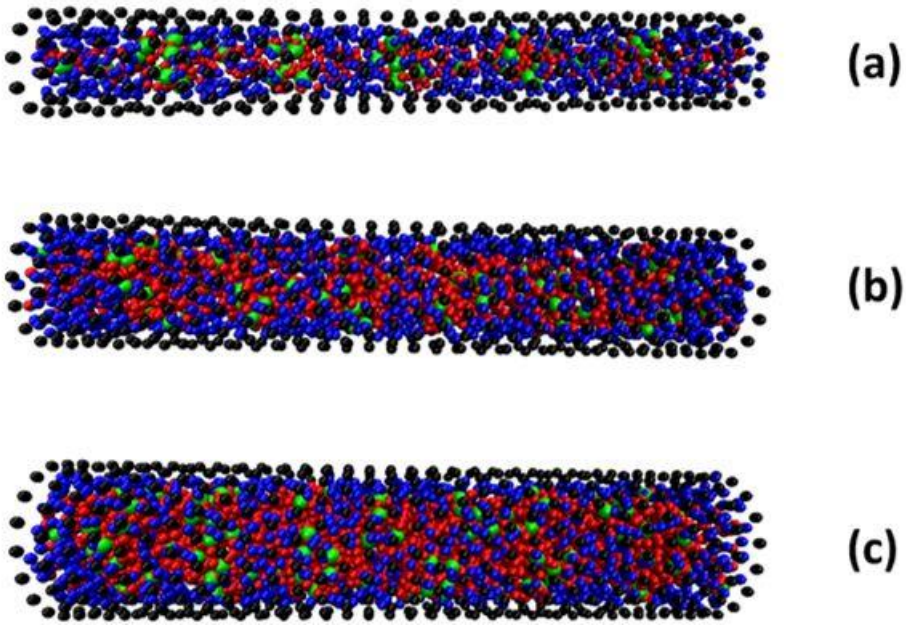

Figure 6.6. The side view of equilibrium snapshot of surfactant and water inside a (22, 22) (**a**); a (30, 30) (**b**); and a (37, 37) (**c**) SWCNT. The surfactant adsorption outside the CNT is removed for clarity. Color code is the same as that in Figure 6.5.

The radial density profile of surfactant at different total SDS concentration was also calculated in Figure 6.7. It indicated that the SDS surfactant prefers to adsorb on the CNT. The density of the surfactant adjacent to the CNT surface is less than the water density. In addition, the density of the surfactant in the bulk phase is significantly lower than the density of water because of the small concentration of surfactant used in this study.

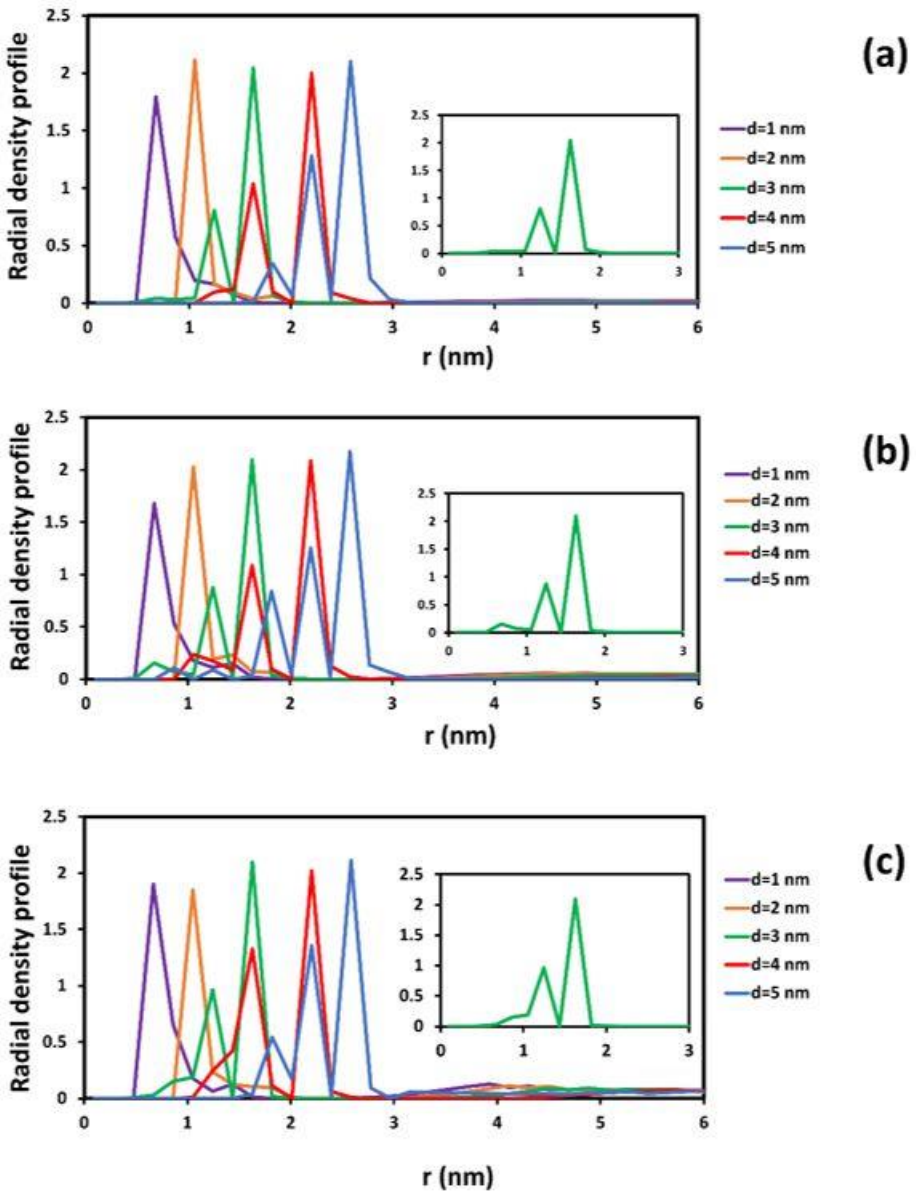

Figure 6.7. Radial density profile of surfactant inside CNTs at different total concentration of SDS: 1 wt% (**a**), 2 wt% (**b**), and 3 wt% (**c**). The insets in each figure exhibit enlargements of radial density profile with respect to distance (r) from 0 to 3 nm in case of SWCNT with diameter of 3 nm.

The concentration of adsorbed SDS surfactant on SWCNT was computed and is presented in the fifth column of Table 6.3. For the same total surfactant concentration in the solution, the amount of adsorbed SDS increased with an increasing diameter of SWCNT, since the total surface area available for adsorption increased (the higher the diameter of the SWCNT, the more available area for adsorption). For the same SWCNT

size, the adsorption of surfactant also increased when the concentration of SDS in the bulk increased. In addition, the adsorption could take place both on the exterior and the interior surface of SWCNT. The distribution of adsorbed surfactant between these two regions was also calculated, and is presented in the third and fourth column of Table 6.3. It is found that the interior surface can contribute from 1 to 13% of the total adsorption of the surfactant, depending on the size of the CNT. As already discussed, adsorption only occurred in the exterior surface of CNTs with diameters equal or smaller than 2 nm.

Table 6.3. Percentage adsorption on the inside and outside surfaces of SWCNTs.

Diameter of CNT	Total Concentration of SDS (wt%)	Percent Adsorption Inside CNT	Percent Adsorption Outside CNT	Total SDS Adsorption (wt%)
1 nm	1	0	100	0.45
	2	0	100	0.44
	3	0	100	0.47
2 nm	1	0	100	0.64
	2	0	100	0.68
	3	0	100	0.67
3 nm	1	1.3	98.7	0.82
	2	1.5	98.5	1.05
	3	2.3	97.7	0.98
4 nm	1	12.9	87.1	0.88
	2	8.7	91.3	1.25
	3	10.1	89.9	1.27
5 nm	1	12.3	87.7	0.90
	2	13.3	86.7	1.48
	3	13.1	86.9	1.50

c. The Effect of SDS Adsorption on Water Distribution and Diffusion Inside the SWCNTs

Obviously, the presence of adsorbed SDS remarkably affects the distribution of water

inside the SWCNTs. In Figure 6.8, we show the radial density profile of water inside CNTs with SDS adsorption. This figure is to be compared to Figure 6.4 for water in a water-CNT suspension. Without SDS adsorption on the inner surface, the radial density profile of water inside the SWCNTs with diameters of 1 and 2 nm in Figure 6.8 is very similar to the case seen in Figure 6.4(a). For larger diameters (d > 3 nm), water beads in the region close to the CNT shifted farther from the CNT wall, because this space was occupied by adsorbed surfactant. This leads to the expansion of the radial density profile from the surface of the CNT. In addition, the magnitude of the peak of the radial density was reduced when the concentration of SDS increased. The density of water near to the CNT surface was dependent on the amount of surfactant adsorption. It dropped when the presence of adsorbed SDS was denser on the CNT surface.

In addition, the axial density profile of water also contributes to the description of the influence of the SDS surfactant on the diffusion of water through the SWCNT (see Figure 6.9 and compare to Figure 6.4(b)). It is found that there is a strong fluctuation of axial density along the length of SWCNTs with diameters of 3, 4, and 5 nm. It can be concluded that the surfactant adsorption changed the structure of the SWCNT interior. The distribution of surfactant inside the CNT was not uniform along the CNT length. This made the fluctuation of axial density profile to be difficult to predict and not periodic. The fluctuations are more apparent when the concentration of SDS increased. For the (8, 8) nanotube with d=1nm, it is notable that the peaks of water density are somewhat fewer than in Figure 6.4(b), but the periodicity of the density peaks is not as regular as it was in Figure 6.4(b). See, for example, in Figure 6.9(a) that there is a larger spacing than 0.67 nm between peaks at z = 14 nm and at z = 18 nm. Same is observed in Figures 6.8(b) and

6.8(c) at other z locations along the SWCNT axis.

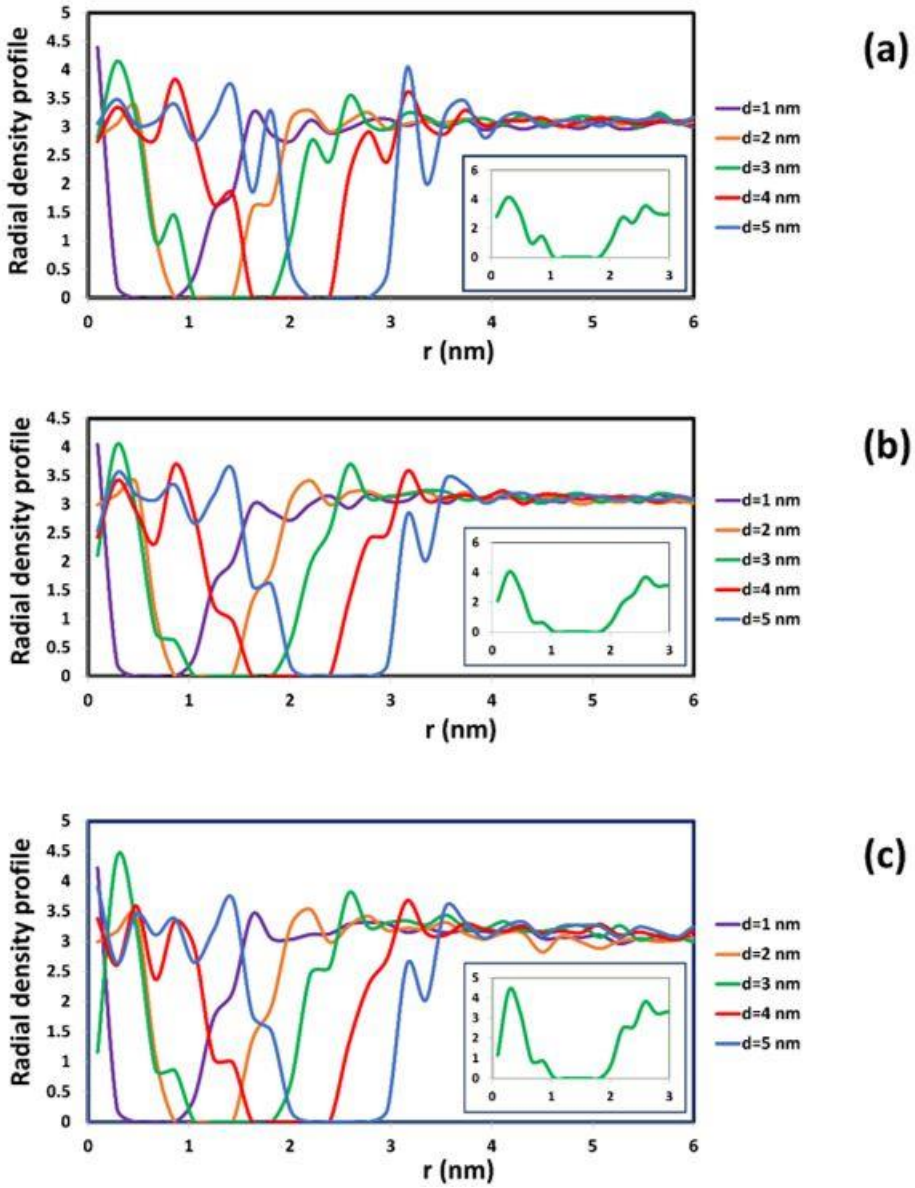

Figure 6.8. Radial density profile of water inside CNT with SDS adsorption at different total concentration of SDS: 1 wt% (**a**), 2 wt% (**b**), and 3 wt% (**c**). The insets in each figure exhibit enlargements of radial density profile with respect to distance (r) from 0 to 3 nm in case of SWCNT with diameter of 3 nm. It is seen that, contrary to the observations in Figure 6.4(a), the radial density profile is different to the exterior and the interior of the CNT wall at r = 1.5 nm.

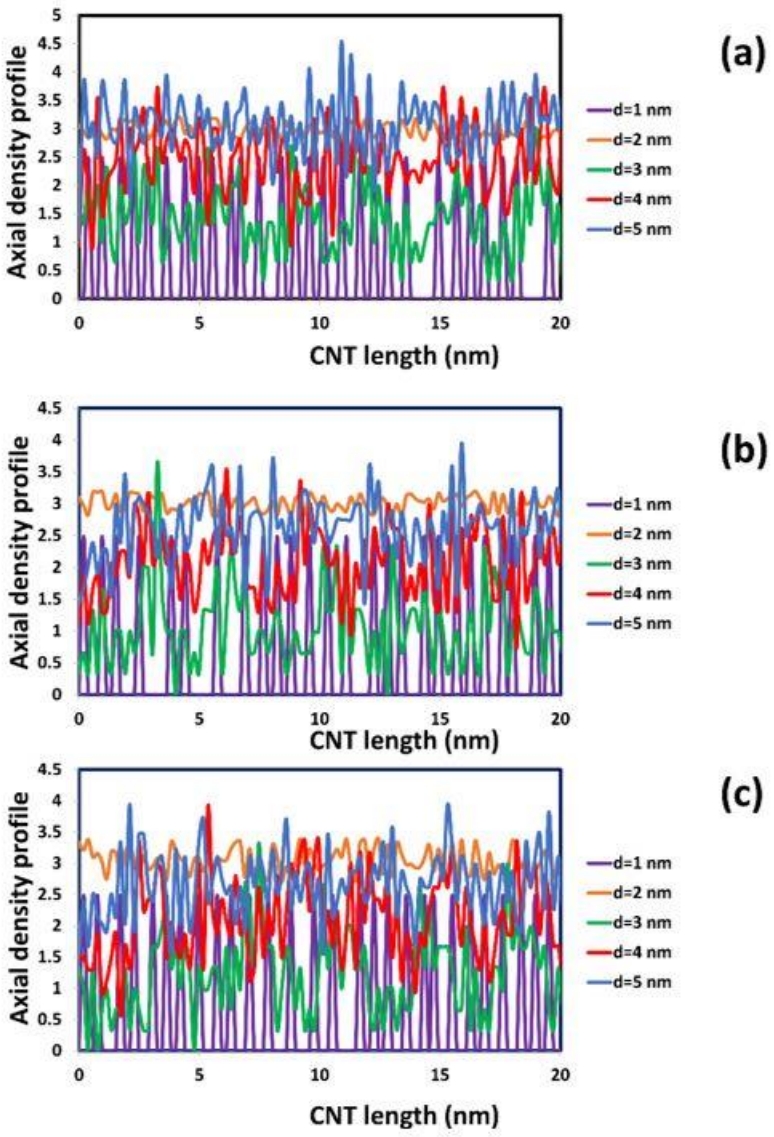

Figure 6.9. Axial density profile of water inside CNT with SDS adsorption at different total concentration of SDS: 1 wt% (**a**), 2 wt% (**b**), and 3 wt% (**c**).

The surfactant adsorption appears to have had a significant impact on diffusivity and on average residence time of water inside the CNT. In Table 6.4, we provide the average residence time for water and the diffusivity for the case of CNTs in the SDS adsorption. There is no effect on residence times for SWCNTs with a diameter of 1 and 2 nm. The adsorption only occurred on the exterior surface of the nanotubes. However, when the surfactant can enter the SWCNT, there is an increase of the average residence time of

water. The adsorption of surfactant molecules changed the surface properties of the interior of the CNT, giving it a more hydrophilic character. The space inside the CNT also narrowed down, because some of it was occupied by surfactants. In addition, the attraction to the surfactant head groups that pointed toward the center of the nanotube made the water retention time longer. Water beads had to spend more time in order to pass through the SWCNTs in the presence of adsorbed surfactants. At the same time, the increase of average residence times led to a decline for the diffusivity of water. This decline is very obvious for SWCNTs with diameters larger or equal to 3 nm.

Table 6.4. Diffusivity and residence time of water in the effect of SDS adsorption.

Diameter of CNT	Total Concentration of SDS (wt%)	Average Residence Time (ns)	Diffusivity of Water Inside SWCNT (cm^2/s)	Ratio between Diffusivity of Water Inside SWCNT with and without SDS Adsorption
1 nm	1	58.1	1.80×10^{-5}	1.42
	2	63.0	1.61×10^{-5}	1.28
	3	61.7	1.78×10^{-5}	1.41
2 nm	1	25.4	2.49×10^{-5}	0.98
	2	24.5	2.59×10^{-5}	1.02
	3	27.7	2.29×10^{-5}	0.90
3 nm	1	20.6	3.07×10^{-5}	0.79
	2	20.8	3.04×10^{-5}	0.78
	3	22.3	2.84×10^{-5}	0.73
4 nm	1	43.8	1.45×10^{-5}	0.37
	2	40.6	1.56×10^{-5}	0.40
	3	42.8	1.48×10^{-5}	0.38
5 nm	1	47.6	1.33×10^{-5}	0.35
	2	51.7	1.22×10^{-5}	0.32
	3	49.4	1.28×10^{-5}	0.34

For the (15, 15) SWCNT that has a diameter of 2 nm, the differences in diffusivity

between the cases with and without surfactant are negligible. However, for the smallest nanotube examined, the (8, 8) SWCNT, there was an increase in diffusivity. This means that even though the average residence time of water inside the CNT is comparable, the distribution of this time is wider for the case with SDS adsorbed at the exterior of the CNT. As was noted when the water density profile along the axial direction of the nanotube was discussed (see discussion above for Figure 6.8 in comparison to Figure 6.4(b)), the distance between peaks in water density is not uniform for water traveling inside narrow tubes with SDS adsorbed around it. The hydrophobic groups of the SDS are adsorbed at the exterior surface of the CNT and their collective effects appear to be felt by the water inside the narrow CNT increasing the diffusivity from ~128% to 142%, as seen in Table 6.4.

The effect of the SDS adsorption on the diffusivity of water inside the CNT is emphasized in Figure 6.10, where we present the changes of relative diffusivity with respect to the CNT diameter as the adsorption of SDS occurs. Note that relative diffusivity with surfactant adsorption is the average value of runs with different total SDS concentration, listed on Table 6.4. Without the presence of surfactant, the diffusivity of water inside the CNT increases with increasing CNT diameter (from 1 to 3 nm). After that, the diffusivity of water is nearly the same as the diffusivity in the bulk phase. In this case, the properties of water inside the CNT become similar to those in the bulk phase. In the occurrence of SDS adsorption, the attraction of hydrophilic head groups to water beads leads to increasing the retention of water beads inside the CNT. For small CNT diameters ($d \leq 2$ nm), when the SDS cannot enter the CNT, the two cases almost coincide. However, for larger CNT diameters ($d \geq 3$nm), when the SDS can enter the CNT, the diffusivity of

water is decreasing as the CNT diameter increases. In contrast to the case of no surfactant present, it does not seem that the diffusivity of water inside the CNT can be equal to that in the bulk for any CNT diameter studied, because of the attraction of hydrophilic tails of adsorbed surfactant and water beads.

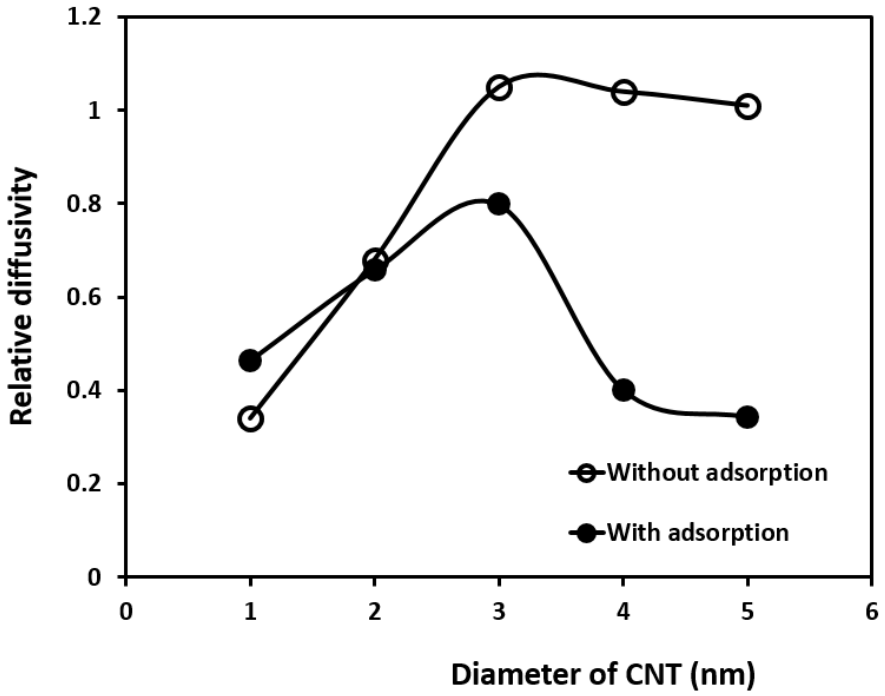

Figure 6.10. The relative diffusivity of water inside CNTs with different diameter with and without SDS adsorption. Relative diffusivity is the ratio of diffusivity of water inside the CNT to that in the bulk phase. The line in this plot is only used to connect the data and guide the eye to see the trend of changing relative diffusivity.

6.4. Conclusions

Our results indicate that DPD can be used to study the transport properties of water in the confined space of SWCNTs. The properties of water in SWCNT from DPD calculation agreed well with MD simulations. For SWCNTs with $d \geq 2$ nm, the radial and axial density of water inside the SWCNT is comparable with those in the bulk phase. Additionally, its diffusivity was enhanced due to the hydrophobic surface of SWCNTs. For SWCNTs with $d < 2$ nm, there was a marked difference in the density profile between

water in the interior of the SWCNTs and in the bulk phase. The diffusivity of water was reduced in those cases, in agreement with prior MD results, because of the ordering of water molecules in almost single file within the interior space of the SWCNTs with small diameters.

It was found that SDS molecules can enter a SWCNT if its diameter is equal or greater than 3 nm. The adsorption of surfactant can occur spontaneously in both the interior and exterior surface of the SWCNT ($d \geq 3$ nm). Obviously, the percentage of surfactant adsorption on the outside of a SWCNT is always dominant, because of the higher available surface for adsorption. The surfactant adsorption inside SWCNT increased with the increasing of SWCNT diameter. Depending on the concentration of surfactant, SDS inside SWCNT can accumulate from 1% to 13% of the total of adsorbed surfactant, and the adsorbed molecules self-assemble in hemi-micellar and random forms. Finally, the adsorption of SDS inside SWCNT led to the change of water properties inside the SWCNT. For SWCNTs with $d \geq 3$ nm, the radial and axial density profile of water inside SWCNT were remarkably different from those in bulk phase. Moreover, the average residence time of water inside SWCNT was increased in the occurrence of surfactant adsorption. The interior of the SWCNT surface was more hydrophilic and able to hold water longer. As a result, the diffusivity of water also decreased with increasing surfactant adsorption inside the SWCNT. In the case of the narrowest SWCNT considered in this study, the water axial diffusivity increased, because of the collective hydrophobic effects of SDS adsorbed on the exterior of the nanotube that can be felt in the confined space.

Chapter 7. Inter-particle and particle-surface interactions

7.1. Introduction

Due to the strong Van der Waals interaction, CNTs tend to form “bundles” or “ropes” into solution [178]. To obtain a well dispersed CNT solution, non-covalent stabilization has been used in experiments [6, 93, 179, 180]. In the presence of polymer on CNT surface, there are steric effects that created repulsive forces among CNTs. The strength of this repulsion depends on the molecular weight and chemical properties of polymer. Besides, the interaction between CNT and solid surface of porous materials was also found to increase the retention of CNTs suspended in the flow. A good stabilizer did not only improve the repulsive forces among CNTs but also prevented the deposition of CNTs on mineral surfaces.

From a simulation approach, many efforts have been applied with different techniques to study the interaction between functionalized CNTs. Nap and Szleifer investigated the interactions between SWCNTs, coated with polymer chains end-grafted to the tubes, and planar surfaces using molecular theory [181]. It was seen that it is possible to immobilize SWCNTs at a desired distance from the surface by proper functionalization of the grafted polymers' free ends. They also proved how the strength and distance of the minimal interaction can be controlled by the proper choice of polymer chain length, surface coverage, and type of functional end-group. From MD simulations, Aztatzi-Pluma and co-workers calculated the interaction between chitosan (CS) at different degrees of deacetylation (DD) and CNTs functionalized with either amine ($-NH_2$) or carboxylic ($-COOH$) groups [182]. It was seen that the attractive interaction between a 50% DD chitosan and the $-NH_2$ functionalized CNT ($CNT–NH_2$) was the strongest among the

different de-acetylated cases under study. For the 50% DD case, a wrapping effect of the CS chain around the CNT–NH_2 structure was attributed to hydrogen bond formation between the amine groups in the CNT and the −OH and $-NH_2$ groups in the CS molecule. Moreover, Zheng et al. studied the interaction between polymers (polyethylene, polypropylene, polystyrene, polyaniline) and SWCNTs by using force field based MD simulations [183]. Results indicated that the interaction between the SWCNT and the polymer is strongly affected by the specific monomer structure such as aromatic rings. The attractive interaction between the simulated polymers and the SCWNTs monotonically increases with increasing SCWNT radius. For the temperature influence, the interaction was strongly affected for polystyrene and polyaniline, but it could be negligible for polyethylene and polypropylene. It was also found that the adhesion energy between the SWCNT and the polymer strongly depends on its chirality. In the mesoscopic scale, Müter et al. calculated surfactant-mediated forces between two CNTs and the influence of their angle and distance by using DPD simulations [184]. It was found that a repulsive region followed by an overall attractive interval with strong oscillations in the force at small distances. Decreasing the angle between CNTs leads to a steady increase in the force, but the relative dependence on the separation distance is maintained. For the case of parallel CNTs, the overall attractive region almost disappeared completely, because of the difference in aggregation and adsorption on CNT surface.

In this chapter, we examine the interaction between two CNTs coated with PVP (called CcP) particles in water. The structure of each CcP particle has been presented in Figure 4.3 (c) in Chapter 4. Additionally, the interaction parameters for CNT and silica surface were determined by comparing with data from molecular theory. Then, the interaction

between CcP particle and silica surface in an aqueous solution was calculated.

7.2. Results and discussion

a. Interaction between two CNT-coated PVP

The propagation of NPs is also affected by the presence of other NPs because of their particle – particle interaction. Without polymer, CNTs agglomerated and formed a bundle in solution due to their strong Van der Waals attraction. The effect of PVP polymer in NH particle on particle-particle interaction was considered. In the calculations, the Lennard-Jones (12, 6) potential was combined with DPD to describe the strong interaction between two CNT particles. In the simulation box, there were two CcP particles. One was kept stationary and the another was allowed to rotate around z axis and move in z direction. Orientation angle (α) is defined as the angle between two major axes of CcP particles initially. The diameter and length of the CNTs was 10 and 50 nm, respectively. The computational domain was 74.97x74.97x47.04 nm^3. All of simulation details about water, CNT and PVP polymer in DPD were presented in section 4.2 of Chapter 4. The system had a total of 258,376 beads consisting of water, CNT and PVP polymer. Every 1000 time steps, the interaction force (F) and position of particle were printed out. Figure 7.1 shows F with respect to distance between two CcP particles in different initial angles.

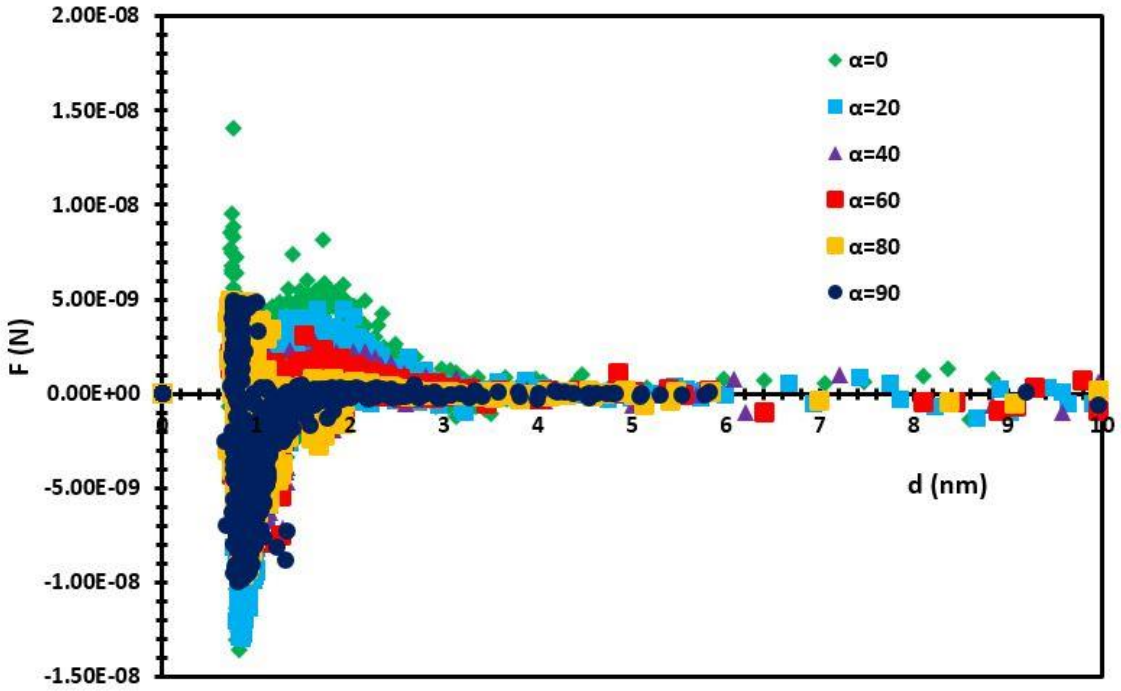

Figure 7.1. Interaction forces between CcP particles

Our results indicate that the PVP created a steric effect on the interaction between CcP – CcP particles. The height of the force peak (around distance of 1.7 nm) depended on the value of α. After distance of 3 nm, the interaction force is nearly negligible. It is better to quantify this interaction via a general equation. We suggest Equation (7.1) to describe this interaction. In this equation, there are two parts. The first one comes from the Van der Waal interaction force with ϵ and σ parameters. These parameters illustrate the depth well of the interaction force and the distance at which the interaction potential is zero. The second part is used to characterize the repulsive force of PVP in CcP particle. The values of the parameters depend on the position of the repulsive peak. The strength of the steric effect is related to parameter b and n.

$$F = 4\varepsilon\left(\frac{12\sigma^{12}}{r^{13}} - \frac{7\sigma^{6}}{r^{7}}\right) \times \left(1 - \sqrt{\pi}\exp\left[\frac{-(r-a)^2}{b}\right] \times n\right) \quad (7.1)$$

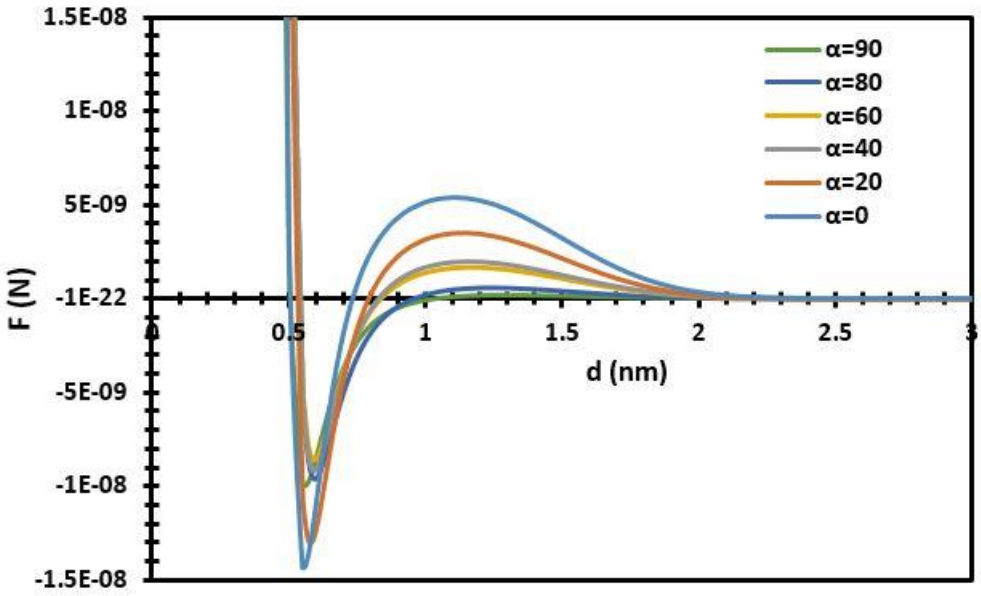

Figure 7.2. Fitting curve of interaction forces between CcP – CcP particles

To determine all these parameters, a non-linear regression with the Levenberg-Marquardt algorithm was used in Polymath software. Data from DPD simulation fluctuated (especially in the distance from 0.6 to 2.5 nm). It was difficult to fit with our model and obtain a high R^2 value. Motulsky and Brown suggested a new method to detect outliers when fitting data with nonlinear regression [185]. Following this algorithm, all parameters in equation (7.1) were computed and shown in Table 7.1 after removing all outlier points of the DPD data.

Table 7.1. Fitting parameters for different α

α	ϵ (N.m)	σ (nm)	a (nm)	b (nm^2)	n
0	3.20E-09	0.45	1.7	0.2	60
20	2.90E-09	0.47	1.7	0.2	35
40	2.05E-09	0.48	1.7	0.2	25
60	1.90E-09	0.48	1.7	0.2	23
80	2.00E-09	0.48	1.7	0.2	9
90	1.90E-09	0.45	1.7	0.2	5

The values of ϵ and n were decreased with increasing of the intial angle (α). Other parameters (σ, a and b) were almost constant with the changes of α. Overall, the

interaction force between two CcP particles depends on the relative orientation between them. The presence of PVP polymer produced a repulsive force which decreases with the increasing of α (Figure 7.2).

b. CNT and silica interaction

Using molecular theory, Nap and Szleifer at NorthWestern University calculated the free energy of the interaction (W) between SWCNT and silica surfaces with different orientation angle (Θ) in Figure 7.3. Results indicated that CNTs were favorable to attach on the silica surface as CNTs reach close to the surface. We can utilize these results to validate the repulsion parameter between CNT and silica. In order to have a good agreement with molecular theory results, it is required to add another potential into DPD algorithm. Because of the strong attraction of CNT on silica, and the shape of free energy in Figure 7.3, we chose the shifted force Lennard-Jones (12,6) potential (Equation 7.2) and Morse potential (Equation 7.3), which were effective in a range of cutoff radius (r_c) and allowed both potential and interaction forces to be continuous at r_c.

$$E = E_{LJ}(r) - E_{LJ}(r_c) + (r - r_c)E_{LJ}(r_c) \qquad \text{where } r < r_c \tag{7.2}$$

$$E_{LJ}(r) = 4\varepsilon\left[\left(\frac{\sigma}{r}\right)^{12} - \left(\frac{\sigma}{r}\right)^{6}\right]$$

$$E_{Morse} = D_o\left[e^{-2\alpha(r-r_o)} - 2e^{-\alpha(r-r_o)}\right] \qquad \text{where } r < r_c \tag{7.3}$$

where E_{LJ} is Lennard-Jones (12,6) potential, ϵ is the depth of the LJ potential well and σ is the finite distance at which the inter-particle potential is zero. D_o, α and r_o are constant parameters for Morse potential.

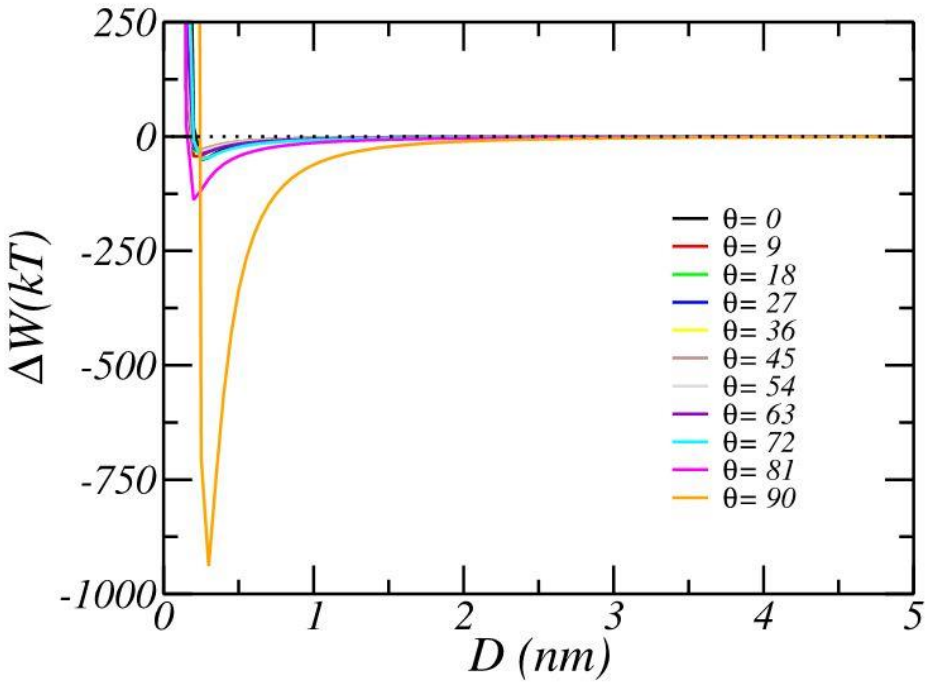

Figure 7.3. Free energy of interaction between SWCNT and silica surface based on molecular theory

Figures 7.4 and 7.5 show the interaction force between SWCNT and silica surface in DPD simulation (red dots) and molecular theory (blue lines). Diameter and length of the CNT are 2.5nm and 5 nm, respectively. For molecular theory, this force (F) is computed from first the derivative of free energy F= -dW/dr. There is a similar shape of interaction force from both molecular theory and DPD. After minimum force, the results from DPD are little higher than molecular theory. This difference comes from the goal of keeping the continuity of potential and force at r_c. These results will provide enough evidence to validate parameter for CNT and silica surface in DPD simulation.

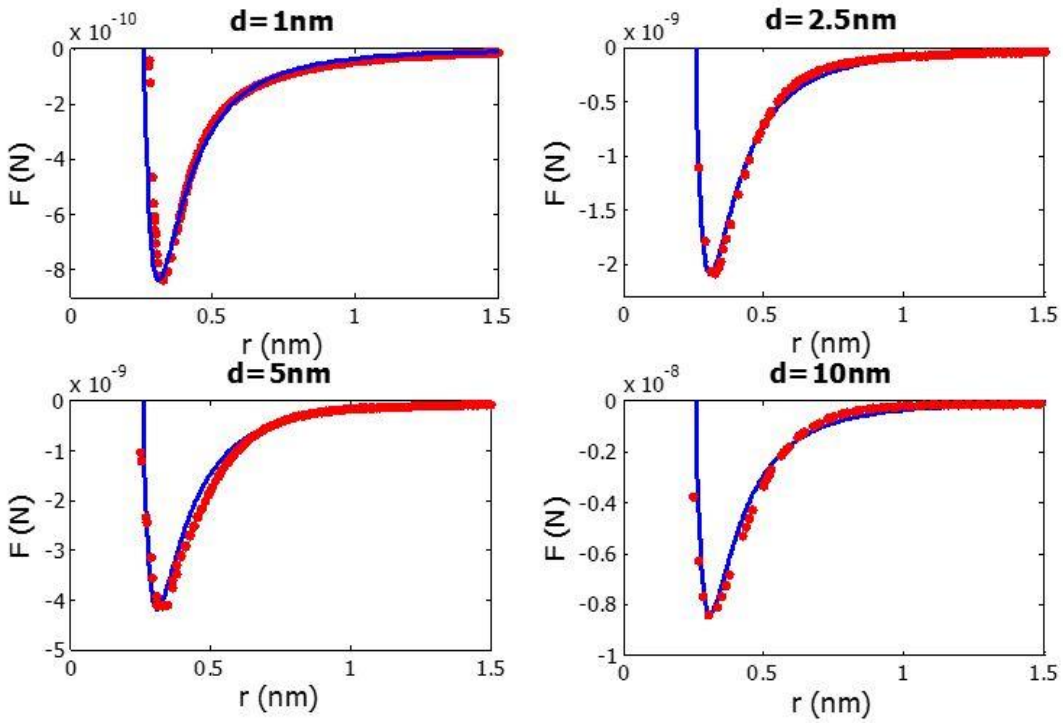

Figure 7.4. Interaction force with respect to distance from molecular theory and DPD simulation in perpendicular case (Θ=0)

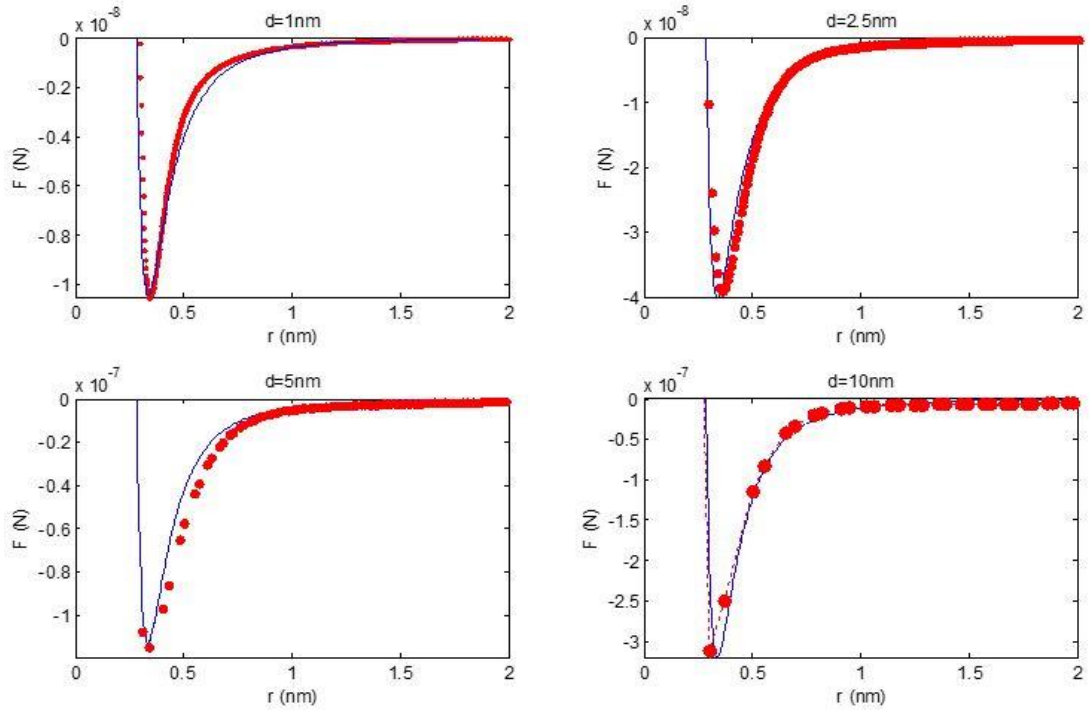

Figure 7.5. Interaction force with respect to distance from molecular theory and DPD simulation in parallel case (Θ=90)

c. CcP and surface (silica) interaction

Using appropriate interaction parameters in Table 7.2 for interaction between CNT and silica surface in DPD simulation, the interaction between CcP particle and silica surface was examined. Silica is the main component in Berea sand. The computational domain was a rectangular box with dimensions 89.67 x 30.87 x 32.34 nm in the x,y and z directions, respectively. The system had a total of 91,062 beads consisting of water, silica, CNT and PVP polymer. The CcP particle in equilibrium was initially placed parallel to the silica surface. A CNT with diameter of 10nm and aspect ratio of 5 was wrapped by 16 chains of PVP polymer. After the water in the system reached equlibrium, the CcP was allowed to move in the water environment. Every 1000 simulation steps, its interaction force and distance of its center of mass to the surface was recorded and plotted in Figure 7.7.

Table 7.2. Interaction parameters of force shifted Lennard-Jones (12,6) and Morse potential for CNT and silica in equation 7.2 and 7.3

ϵ	20
σ	0.455
D_o	550
α	90
r_o	0.455

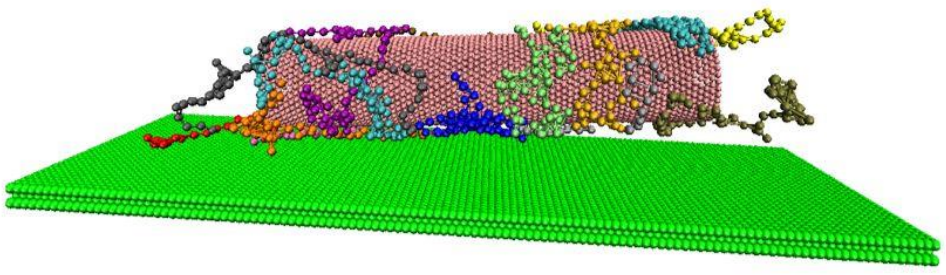

Figure 7.6. Visualization of CcP particle and silica surface (green dots) interaction

Figure 7.7 shows the force curve of CcP particle and surface interaction with respect to distance. As the CcP reached close to the surface, this force got stronger. In this region, the force increased nearly vertically. This indicated that the presence of polymer helps the CcP particle not to attach on a silica surface. There was always a minimum distance between the surface and the particle. Even though CNT and silica are strongly attracted to each other, they can not be any closer. As the distance was becoming larger, the interaction force descreased. This force profile can help to determine the attachment coefficient (k_a) of a particular mineral surface via measuring interaction forces between that surface and the particle.

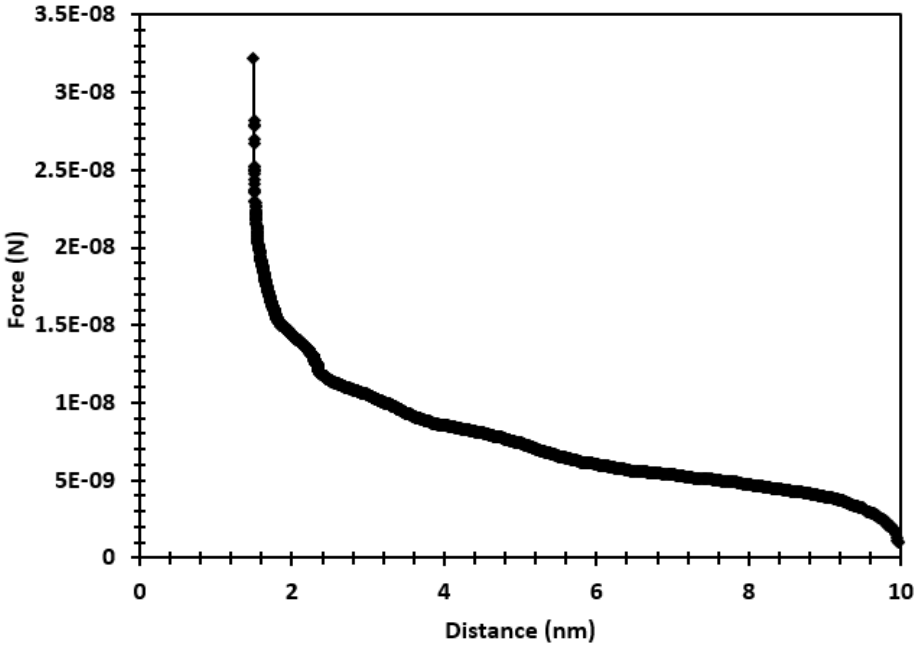

Figure 7.7. Interaction force of CcP particle and silica surface

7.3. Conclusions

We studied the particle – particle and particle – surface interaction using DPD simulation. The steric effect of PVP polymer on the inter-particle interaction was clearly presented via force curves at different orientation angle (α) in respect of distance between two CcP

particles. Based on these data, the CcP – CcP interaction was described by a simple equation (7.1) with different parameters for each value of α.

In addition, appropriate parameters for the interaction between bare CNT and silica surface in DPD simulation were also identified by comparing to molecular theory results. Both shifted force Lennard-Jones (12,6) potential and Morse potential were added into DPD algorithm to duplicate the strong attraction of CNT and silica. The presence of polymer on CNT surface reduced the attractive force between silica and CNT. There existed a minimum distance between CcP particle and silica surface due to the steric effect of adsorbed polymer molecules.

Chapter 8. Propagation of NP in porous media from mesoscopic scale simulation

8.1. Effects of hydrodynamic forces on CcP particle propagation from Lagrangian particle tracking simulation

In addition to Brownian motion, which along with convection are the dominanant effects on nanoparticle motion, other effects can be siginifcant for the determination of the fate of NPs as they propagate in a porous medium. Depending on the size of the NPs and the flow regime, some forces become smaller than others and can be negligible. We modeled the movement of the nanoparticles by considering them to be cylindrical, since our NPs are nanotubes coated with stabilizing polymers as also evidenced by SEM images.

We have examined hydrodynamic forces (such as drag force, gravity and buoyancy force), and whether these are important for such particles, by studying trajectories of NPs moving in micro-channels with size comparable to the pore space in Berea sandstone (10x5x5 μm) and flow velocities comparable to those in column experiments. The simulation conditions are presented in Table 8.1. The velocity profile of the flow was obtained from Lattice Boltzmann method (see in Appendix A3). The forces were obtained as discussed in section 2.2.

Table 8.1. Simulation conditions of flow through microslit

Size of domain	101x52x51 nodes (10x5x5 μm)
Number of released NPs	10,000
Reynolds number	2.52×10^{-4}
Average fluid velocity	4.93×10^{-3} cm/s

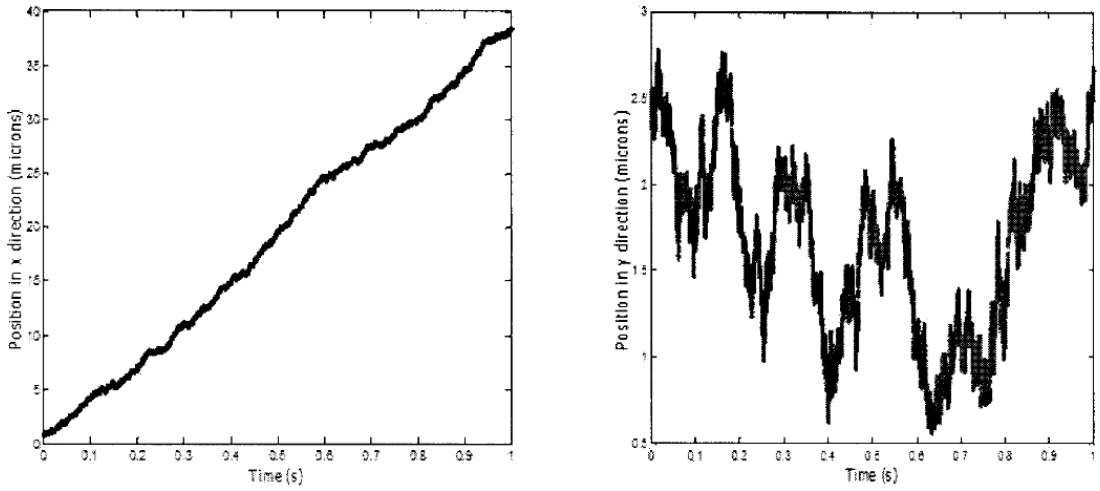

Figure 8.1. Trajectories of particles with β =100, and density eaual to the density of multiwalled carbon nanotubes.

Figure 8.1 is a trajectory in x and y direction for a particle with aspect ration equal to 100, which is the most common case of our NPs. In x direction, the paritcle moves nearly with constant velocity. It depends on the position of the particle in z direction. As the particle goes away from center, it moves lower. Because of the parabolic velocity profile of flow, it has its maximum at the center of the channel. In y direction, particle moves randomly. The effect of gravity and buoyancy force is neglegible. Average magnitube of all hydrodynamic forces is presented in Table 8.2. Random force and drag force are larger than others. To determine the attachment of particles on surface, we need to consider the presence of the interaction among particles as moving and the attration of particles on the solid wall.

Table 8.2. Hydrodynamic forces acting on CcP particles

Drag force (N)	**Gravity & buoyancy force (N)**	**Random force (N)**
0.62×10^{-11}	0.11×10^{-13}	0.61×10^{-11}

Figure 8.2 shows the probability of α during moving of particle in flow. Initially, all

particles having major axis perpendicular to direction of flow are released into flow domain. It means α is 90 degrees in the beginning. The velocity profile of the fluid depends on y position, but the particle also has a long length. So, the fluid velocity acting on a particle is different on the surface of particle. This creates a torque because of the difference of center of mass and center of pressure in particle. The particle rotates simultaneously with the movement in order to balance all forces exerted on its body. The tendency of α is towards having small values.

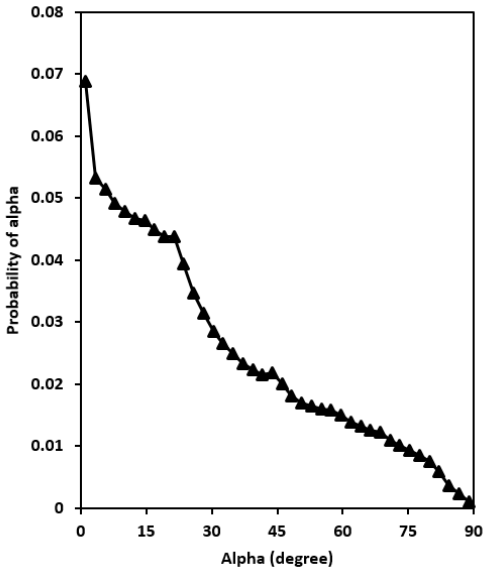

Figure 8.2. Distribution of angle (α) between main axis of particle and plan xz

8.2. CNT propagation at the microscopic scale (with DPD)

a. Motion of a CNT particle in a micropore

To study the behavior of a CNT particle during movement in a micropore, we conducted several simulations for a NP released perpendicular to the flow direction at the center between two parallel slits. The particle had different aspect ratios, keeping the diameter constant (d=10nm). The simulation conditions are presented in Table 8.3. All the

calculations with the DPD method are dimensionless. In order to convert into physical units, we use mass, length, time and temperature scales for the simulations (Table 8.4).

Table 8.3. Simulation conditions

Size of domain	15x15x101 (0.15x0.15x1 μm) with periodic condition in x and y direction.
Reynolds number	0.067
Average fluid velocity	0.052 (around 6.7 cm/s)

Table 8.4. Converting units in DPD

Mass scale	3.32×10^{-23} kg
Length scale	10 nm
Time scale	7.6 ns
Temperature scale	273 K

Figure 8.3 is a presentation of the calculation of the trajectory of NPs with different aspect ratio in x and z direction in DPD simulation. With the same Re number, the particle with the lower aspect ratio goes faster than a particle with higher aspect ratio. This is reasonable because of the bigger hydrodynamic forces acting on the particle with longer length. The trajectory in z direction also indicates the ability of a particle to attach on the surface. Depending on the value of the repulsion parameter of CNT and silica surface, particles can attach on the solid wall. With a suitable parameter, we can create a good approximation to calculate the deposition rate of CNTs on a surface. Addiontially, the distribution of the orientation angle (α – angle between the main axis of CNT and the plane xy) has quite similar shape with results from LPT, as seen in Figure 8.4. It indicates a good relation between LPT and DPD method.

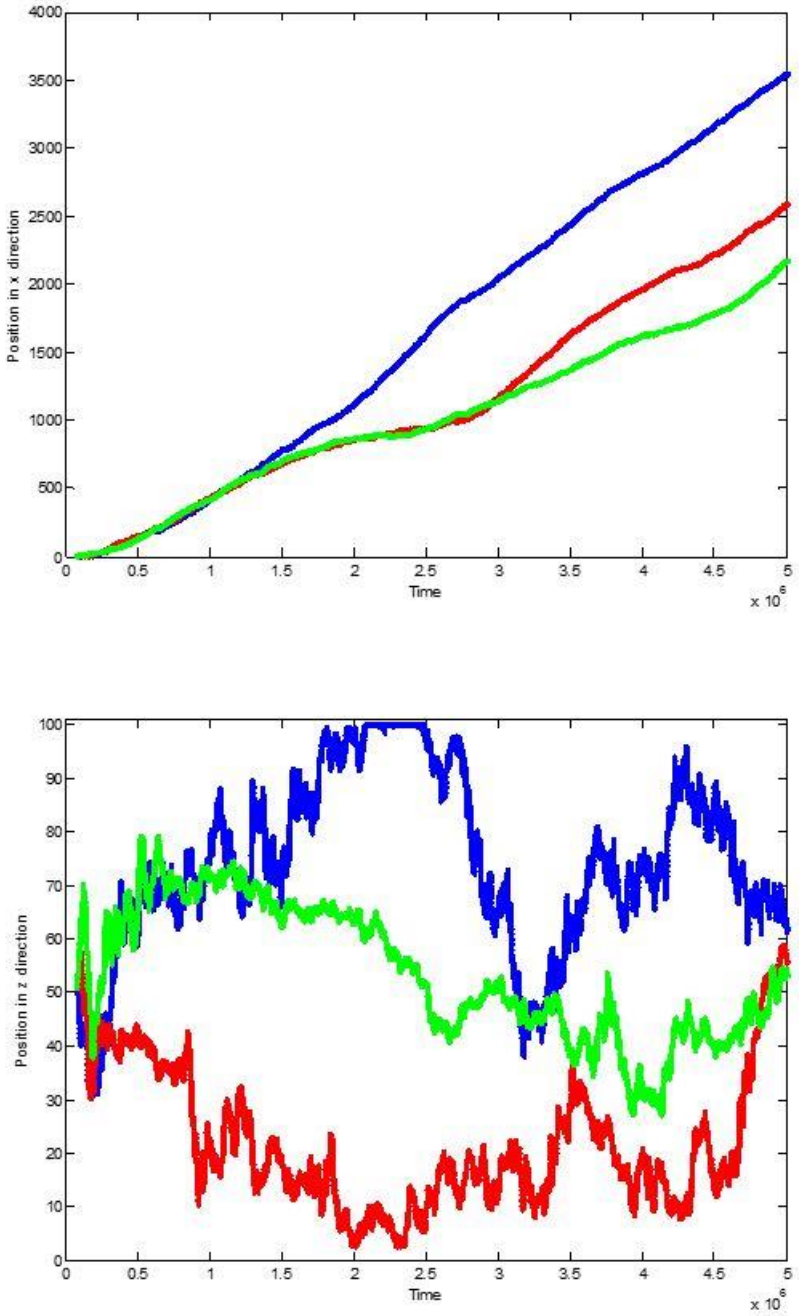

Figure 8.3. Trajectories of particles in x and z direction (*Blue line: β =8; Red line: β =20, Green line: β =50)*

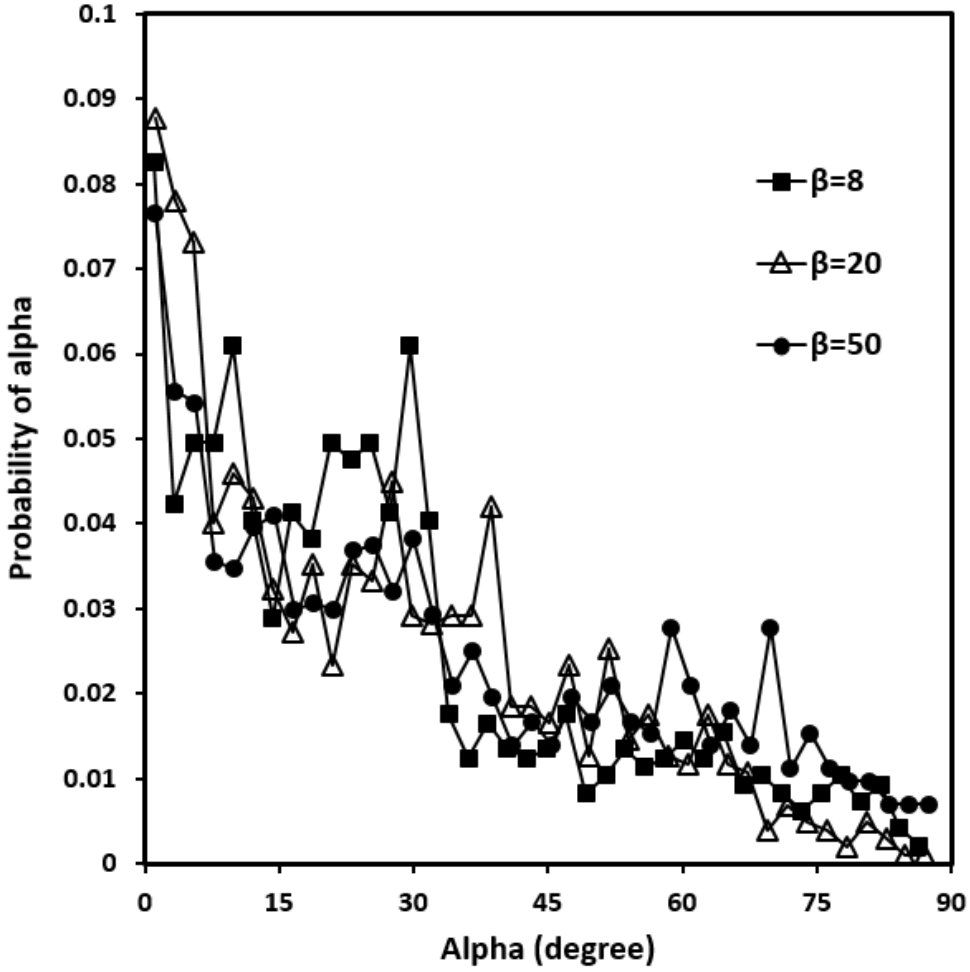

Figure 8.4. Distribution of angle (α) between main axis of particle and plan xz

b. Motion of CNT through an array of solid spheres

In addition, DPD has many advantages for colloidal systems with complicated structure like porous media. We conducted several simulations to study the ability of a CNT to propagate through an array of spherical solids (Figure 8.5). Diameter and length of CNT are 10 nm and 50 nm, respectively. Each spherical solid has diameter of 40 nm and the center-to-center distance between spheres is 60 nm. Our simulation box is 180x180x180 nm with periodic conditions applied in three dimensions.

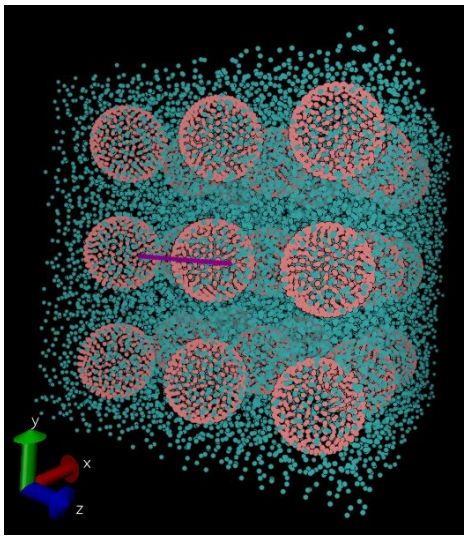

Figure 8.5. Initial position of all DPD beads (Blue points are water, red points are silica solid and purple points are CNT particle)

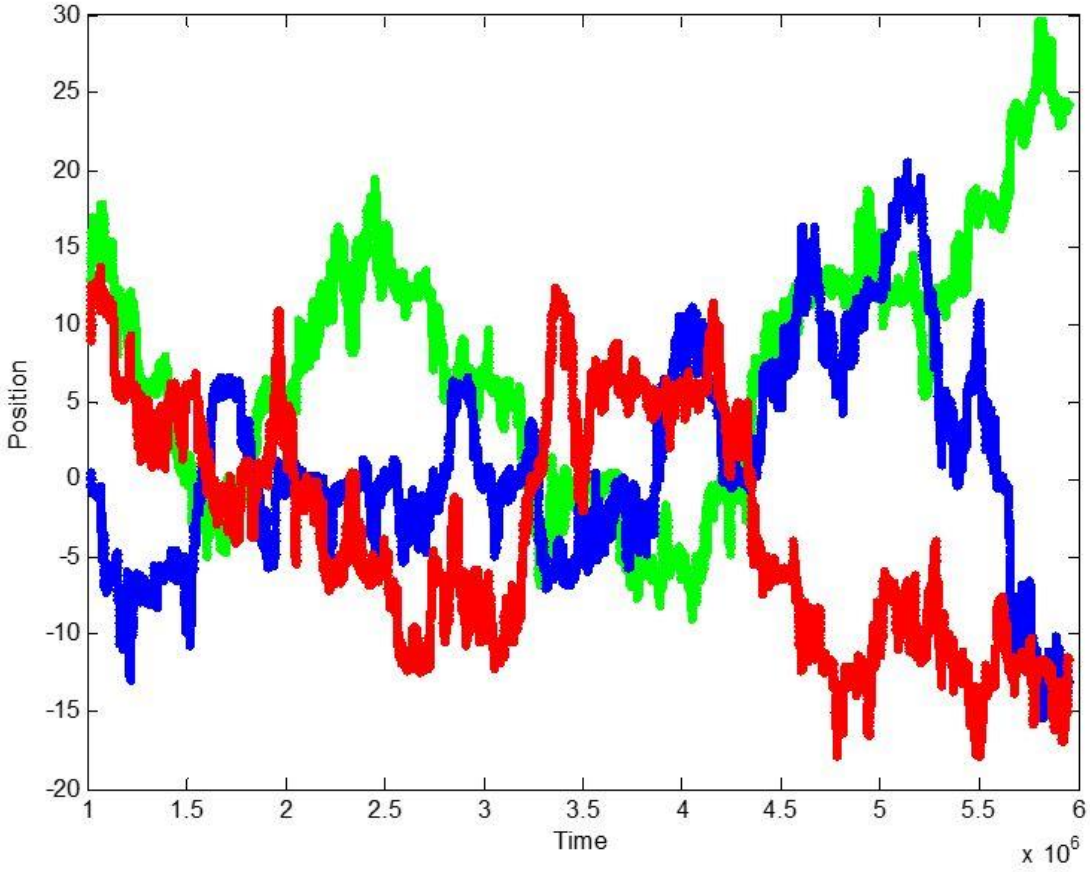

Figure 8.6. Trajectory of particle in x (blue line), y (red line) and z (green line) direction

The movement of a CNT through porous media (array of spheres) is shown in Figure 8.6.

In this case, the length of a particle is larger than the distance between 2 surfaces of spherical solid. Hence, CNT particle undergoes a lot of collisions during travelling among spheres. These results show that the ability of DPD method to explore the diffusivity of particles in complex geometry.

8.3. Motion of Cylindrical and Spherical Nanopartilces in Porous Media with DPD

We carried out several DPD simulations to study the propagation of nanoparticles in porous media of different porosity. In our calculations, an array of spheres is utilized to create the porous medium (see Figure 8.7 for a schematic). The porosity can be adjusted by changing the diameter of the spheres (d_{sphere}) forming the solid structure. The simulation box was 300x300x300 nm with periodic conditions in all 3 dimensions. For water, we grouped 11112 molecules into one bead, so the length scale of DPD calculation is equal to the diamter of the cylindrical particle (10nm). In this case, the geometry of the CNT becomes a string of connecting DPD beads. Time step of simulation was 0.01. Angle orientation of cylindrical particles (α) is defined as the angle between the major axis of particle and the plane (xz). Initially, cylindrical particles were placed perpendicular to the xy plane ($\alpha_o=90^o$). The water flow direction was in the x direction and a nanoparticle was only allowed to move after water reached equilibrium.

When the solid surface is silica, CNT is almost attached and adsorbed on the surface because of the strong interaction between silica and CNT, and a particle could not propagate through our geometry. In the following discussion, however, we assumed that there was no interaction between the particle and surface, and that all collisions of the particle and surface were elastic.

a. The effect of the aspect ratio

The propagation of cylindrical nanoparticle in a porous medium could depend on its aspect ratio (length/diameter), β. To explore this effect, all partilces were kept with the same diameter of 10nm but the aspect ratio β varied from 5 to 20 (see Figure 8.7 for a schematic). One would expect that longer particle would move slower, because of the higher particle mass. In order to observe only the effect of aspect ratio, all particles were adjusted to have the same mass but different β. The porosity of the geometry (ϕ) was 69%. Initial position of particles kept similar. Position of particles was tracked and printed out at every 1000 time steps. Particle trajectories in x direction are presented in Figure 8.8.

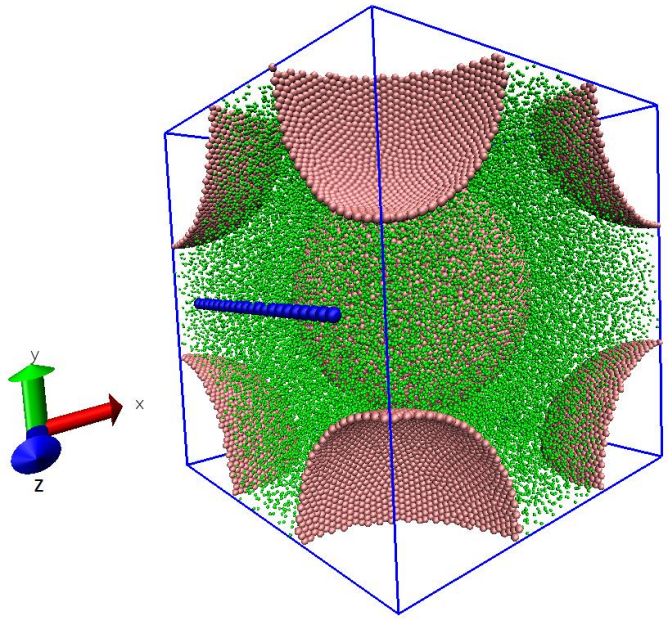

Figure 8.7. Initial position of DPD beads (Green points are water, Red points are silica solids and Blue points are CNT particle)

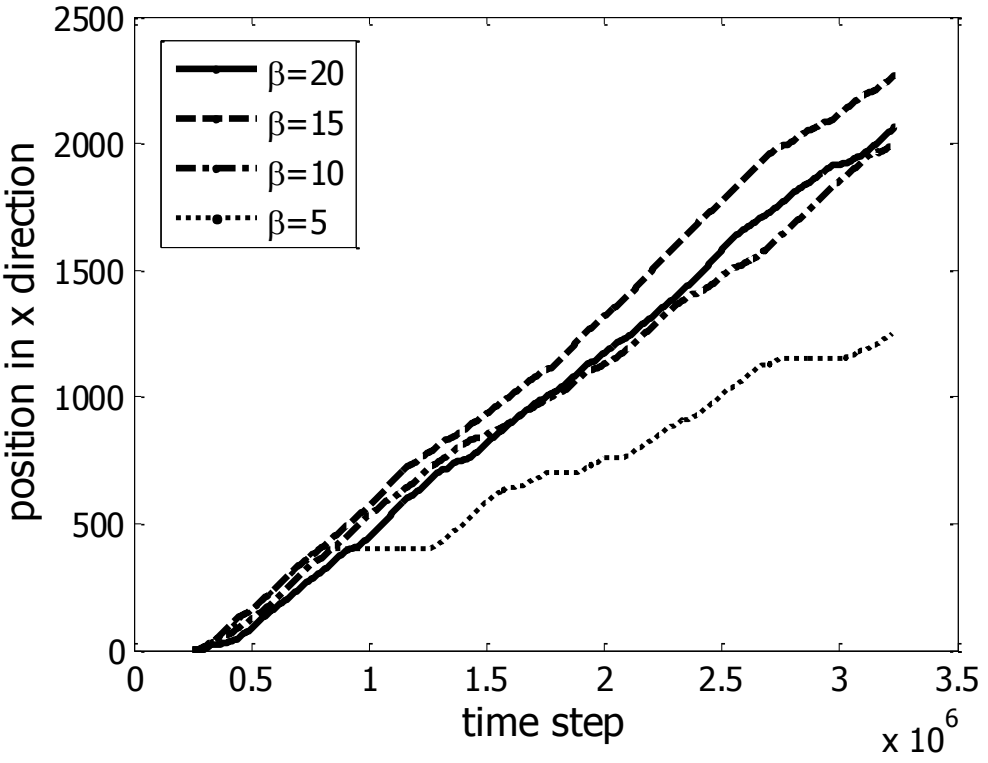

Figure 8.8. Trajectories of a cylindrical particle with different aspect ratio β in x direction.

Results from Figure 8.8 indicate that particles with higher aspect ratio could move faster in porous media than those with small aspect ratios. The collisions play a main role in the propagation of particles. We can see plateaus of the particle trajectory with β=5. During the plateau, the particle was trapped in the space among solid spheres and it had to collide and change its orientation until passing through the solid geometry. After each collision, particles with longer β changed their orientation effectively and kept travelling with the flow. A lower β particle is easy to rotate in the open space of the pore geometry. It can, thus, have a more even distribution of orientations and it undergoes more collisions during movement. The distribution of the rotation angle α in Figure 8.9 strengthens this argument. The orientation of a particle tended to small angles for β>10. Longer particles had a higher probability of α in the range of 0 to 20 degrees, while the probability of a

particle with β=5 is more uniform. Therefore, it is easier for longer aspect ratio particles to propagate through a porous medium, when the interaction between particles and surface is neglected.

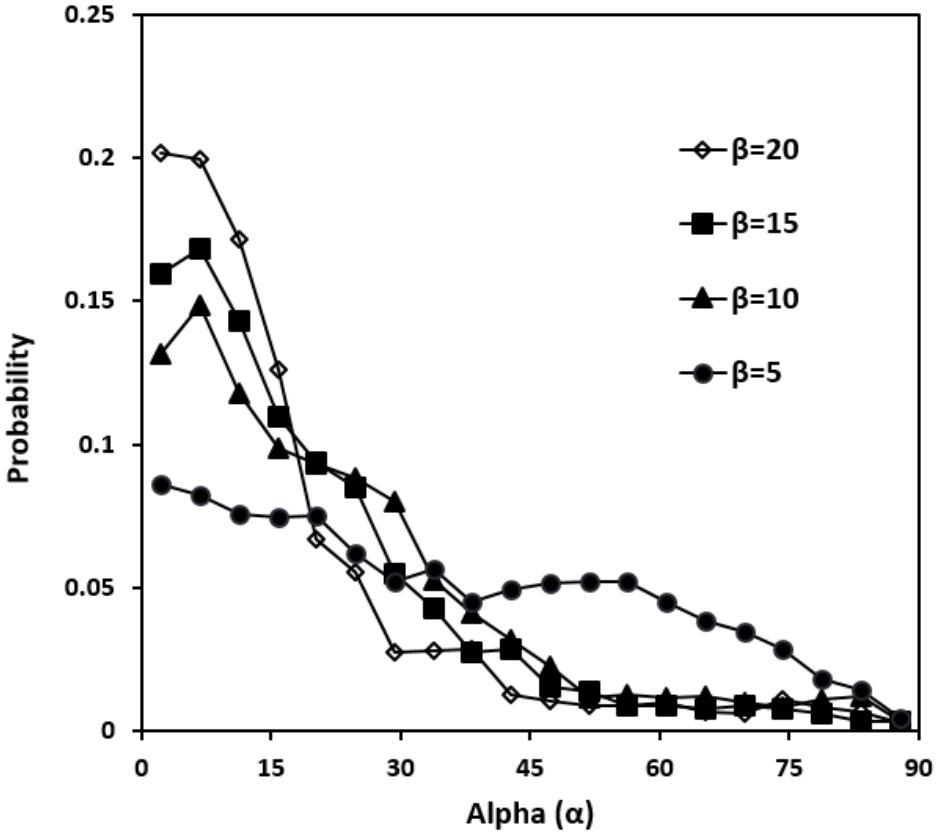

Figure 8.9. The distribution of the rotation angle (α) relative to the xy plane with different aspect ratio

b. The effect of porosity

All partilces were kept at the same diameter of 10nm and aspect ratio (β = 20) while the porosity ϕ was varied from 69 to 93%. Their trajectories in *x* direction are seen in Figure 8.10. With the same flowrate, the fluid velocity is larger as the porosity decreases, due to the mass balance for incompressible flows. A particle is expected to undergo higher hydrodynamic forces in cases of lower porosity. The particle velocity also increased,

leading to a longer distance of particle movement in x direction. In brief, the porosity does not only create the structure retention of the propagation of nanoparticles but also affects the velocity of particles.

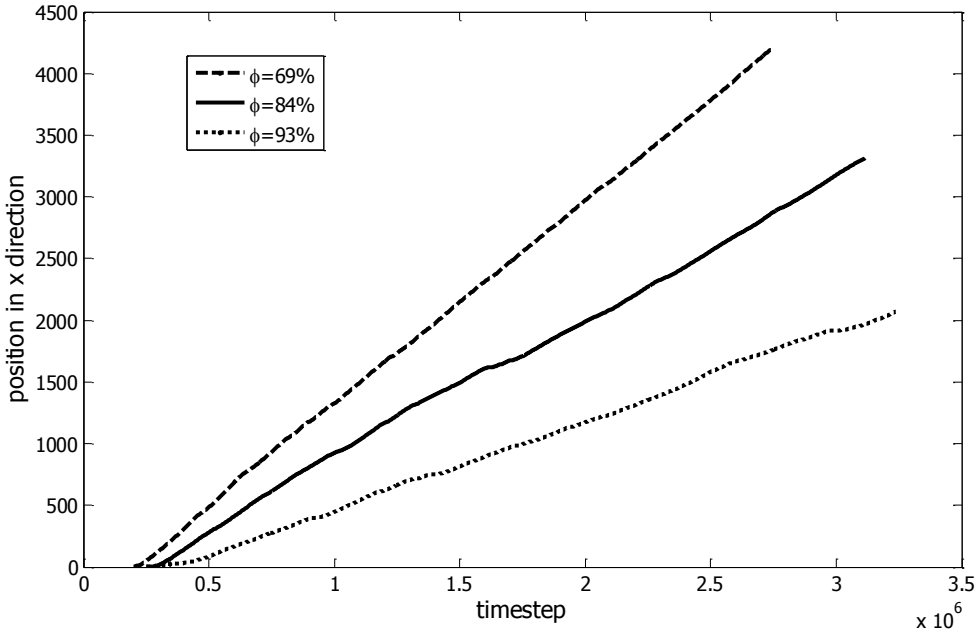

Figure 8.10. Trajectories of cylindrical particle with different ϕ in x direction

c. Spherical vs. cylindrical particles

It is simpler to work with spherical particles than cylindrical ones. We want to determine whether a modification of a spherical model can be used to compute forces and trajectories for cylindrial nanoparticles. To explore further this idea, we calculated the trajetory of spherical particles that had diameters that were equal to the equivalent diameter of the cylinders. For a cylindrical particle, the aspect ratio β was changed from 5 to 20. Similarly, all particles were adjusted to have the same mass but different β. The porosity of the geometry was equal to 69%.

The equivalent diameter (D_{eq})of a cylindrical particle is calculated as follows [186]:

$$D_{eq} = \frac{3d}{2\left[\frac{0.448}{\ln(2\beta)-0.5}+\frac{1.7888}{\ln(2\beta)+0.5}\right]^2} \tag{8.1}$$

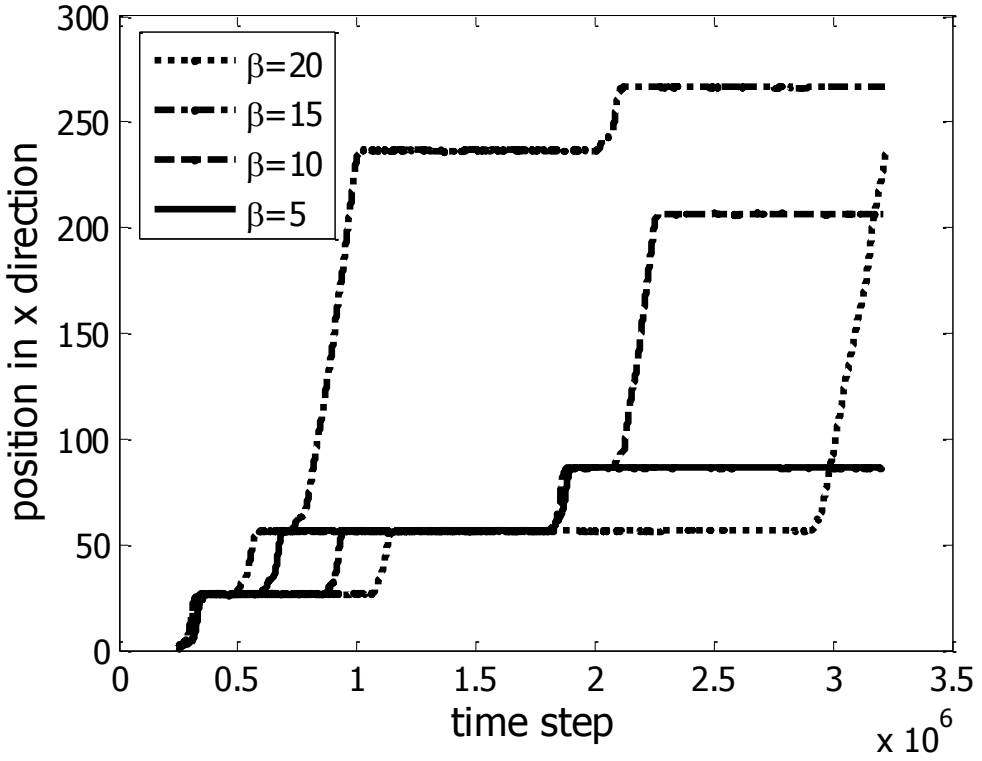

Figure 8.11. Trajectories of spherical particle with equivalent diameter is equal to cylindrical particle in x direction

The trajectories of spherical particles are displayed in Figure 8.11. Comparing with cylindrical particles, appearing on Figure 8.10, spherical particles move very slowly. Their trajectories look like a sequence of step functions, and the distance between steps is on the order of the distance between the solid spheres forming the porous medium matrix. Spherical particles appear to spend a lot of time at a constant x position because of the collisions between the particles and the solid surface. It is more difficult for spherical particles to go around an array of solid spheres. Cylindrical particles only need to change their orientation to reduce the collisions with a solid sphere surface and to keep following the flow. Hence, a spherical particle with the same equivalent diameter suffers

more collisions with the surface than a cylindrical particle under the same conditions. In other words, we might need to update models that apply to spherical particles when calculating the propagation of cylindrical ones.

8.4. Conclusions

We investigated the propagation of NPs in a porous medium (micro-pore and sphere-packed geometry) with LPT and DPD simulation. For cylindrical NPs, drag force and random force are two dominant forces during their movement in low Re regime. The collision of NPs and solid surface caused the deposition of NPs in porous media. Depending on the surface properties of the wall and the particles, CNTs can be attached on the wall or collide and jump away from the wall.

In addition, the motion of cylindrical NPs with different aspect ratio and porosity of geometry were also carried out in DPD simulation. It was found that longer aspect ratio NPs can propagate easier through a porous medium, when the interaction between particle and surface is neglected. Besides, the distribution of the angles α indicated the similarity between LPT and DPD simulation. Cylindrical NPs preferred to rotate orientation (main axis) following the direction of the flow.

Moreover, spherical and cylindrical NPs showed different ways to go through a sphere-packed geometry. Due to the symmetry in all directions, spherical NPs required to undergo many collisions with solid surface during their movement. It was observed that cylindrical NPs have less collisions than spherical ones. A cylinder can change its orientation to pass through a narrow space.

Chapter 9. Summary and Recommendations for Future Research

9.1. Summary

This dissertation was focused on the study the non-covalent stabilization of CNTs in water by using polymer and surfactant, as well as the propagation of stabilized NPs in porous media. Some main points can be drawn as follows:

✓ In terms of DPD methodology, all required interaction parameters for the systems of water and CNT; PVP molecules in water; CNT and silica surface; ionic (Alfotera – AF) or/and non-ionic (Tergitol – TG) surfactants in water were calculated and validated.

✓ For polymer stabilization, the conformation of carbon nanotubes (CNT) grafted with polyvinyl pyrrolidone (PVP) and the physical adsorption of the PVP under shear flow was carried out in DPD simulation. The behavior of PVP on the surface of CNTs was illustrated after the physical adsorption of PVP on the CNT reached equilibrium in an aqueous medium. It was found that PVP molecules prefer to adsorb on the CNT surface and to occupy an "island" area. To examine the structure of CNT-PVP under shear flow, equilibrium CNT-PVP particles were released into Couette flow. Depending on the shear rate, the polymer could be in one of three configurations: adsorbed, shear-affected and separated. Additionally, the conformation of the polymer was influenced. Average values of the end-to-end distance and the radius of gyration were found to increase when the shear force increases. In addition, the influence of particle shape on the physical adsorption of PVP polymer on carbon nanoparticles (CNP) was also considered. It was found that the polymer was stably adsorbed under higher shear conditions for graphene-

like particle. Additionally, the end-to-end distance and the radius of gyration of the polymer adsorbate was clearly related to the adsorption state, as the polymer underwent a transition from adsorbed to the separated state when the shear rate increased. The critical shear rate at which the polymer desorbed from the surface could be useful in applications where nanoparticles can be used as a molecular delivery system. The physical adsorption and desorption of the same polymer molecules on a flat surface were also investigated. The desorption of the polymer from the flat surface occurred when the shearing force was stronger than the attraction between PVP and the surface.

✓ For surfactant stabilization, the adsorption of the commercial surfactants alfoterra 123-8s (AF) and tergitol 15-s-40 (TG) on CNTs was also investigated with DPD simulations. Properties of surfactants (i.e., critical micelle concentration, aggregation number, shape and size of micelle, diffusivity) in water were determined to validate the simulation model. Results indicated that the assembly of surfactants (AF and TG) on CNTs depends on the interaction of the surfactant tail and the CNT surface, where surfactants formed mainly hemi-micellar structures. Most surfactant micelles formed spherical shapes in solution. The particles formed by the CNT and the adsorbed surfactant became hydrophilic, due to the outward orientation of the head groups of the surfactants that formed monolayer adsorption. In the binary surfactant system, the presence of TG on the CNT surface provided a considerable hydrophilic steric effect, due to the EO groups of TG molecules. It was also seen that the adsorption of AF was more favorable than TG on the CNT surface. Diffusion coefficients for the surfactants in the bulk and surface diffusion on the CNT were calculated. Our results are applicable, in a qualitative sense, to the more general case of adsorption of surfactants on the hydrophobic surface

of cylindrically-shaped nanoscale objects.

✓ The ability of sodium dodecyl sulfate (SDS) to adsorb inside a SWCNT, as well as the effect of surfactant on the properties of water inside the SWCNT were studied in DPD simulation. The diameter of the SWCNT varied from 1 to 5 nm. The radial and axial density profiles of water inside the SWCNTs were computed and compared with published molecular dynamics results. The average residence time and diffusivity were also calculated to show the size effect on mobility of water inside the SWCNT. It was found that nanotubes with diameter smaller than 3 nm do not allow SDS molecules to enter the SWCNT space. For larger SWCNT diameter, SDS adsorbed inside and outside the nanotube. When SDS was adsorbed in the hollow part of the SWCNT, the behavior of water inside the nanotube was found to be significantly changed. Both radial and axial density profiles of water inside the SWCNT fluctuated strongly and were different from those in bulk phase. In addition, SDS molecules increased the retention of water beads inside SWCNT ($d \geq 3nm$) while water diffusivity was decreased.

✓ The steric repulsion of adsorbed polymer on NPs surface was illustrated by calculating particle – particle and particle – surface interaction forces.

✓ Hydrodynamic forces were computed when releasing thousands of NPs into a micropore in low Re flow. Drag force and random force were dominant in our case study. Neglecting surface deposition, both spherical and cylindrical NPs can propagate through porous media even though spherical and cylindrical particles overcame physical retention differently. Cylindrical particles can propagate easier through packed spheres than spherical particles.

9.2. Recommendations for Future Research

Based on our current results, the following future works could be carried out as follows:

- Investigate the dispersion of CNTs under the influence of both salinity (charged ions) and temperature.
- Explore the distribution of adsorbed surfactants on CNT at oil/water interface.
- Study the effect of extensional stresses on the physical adsorption of polymer and CNT; deformation of surfactant micelles.
- Examine the role of NPs, surfactant and liquids in a system of capillary foam.
- Calculate the diffusivity of NPs in the simulation domain.

References

[1] Kong X, Ohadi MM. Applications of Micro and Nano Technologies in the Oil and Gas Industry - Overview of the Recent Progress. Society of Petroleum Engineers 2010:138241.

[2] BP Energy Outlook; 2016.

[3] Green DW, Willhite GP. Enhanced Oil Recovery. Richardson, Texas: Society of Petroleum Engineers; 1998.

[4] Nabhani N, Emami M, Moghadam ABT. Application of Nanotechnology and Nanomaterials in Oil and Gas Industry. AIP Conf Proc 2011;1415:128-31.

[5] Cookson C. Nanotech SensorsTo Reveal Reservoir: American Oil & Gas Reporter; 2014.

[6] Kadhum MJ, Swatske DP, Harwell JH, Shiau B, Resasco DE. Propagation of Interfacially Active Carbon Nanohybrids in Porous Media. Energy Fuels 2013;27(11):6518–27.

[7] Kadhum MJ. Interfacially active carbon nanotube hybrids for reservoir development applications. The University of Oklahoma PhD Ph.D. Thesis, 2013.

[8] Calvaresi M, Dallavalle M, Zerbetto F. Wrapping Nanotubes with Micelles, Hemimicelles, and Cylindrical Micelles. Small 2009;5(19):2191-8.

[9] Mishra AK. Nanomedicine for Drug Delivery and Therapeutics. Canada: Wiley-Scrivener; 2013.

[10] Zhang Y, Chen Y, Westerhoff P, Hristovski K, Crittenden JC. Stability of commercial metal oxide nanoparticles in water. Water Res 2008;42:2204-12.

[11] Tso C-p, Zhung C-m, Shih Y-h, Tseng Y-M, Wu S-c, Doong R-a. Stability of metal oxide nanoparticles in aqueous solutions. Water Sci Technol 2010;61(1):127-33.

[12] Jiang J, Oberdörster G, Biswas P. Characterization of size, surface charge, and agglomeration state of nanoparticle dispersions for toxicological studies. Journal of Nanoparticle Research 2009;11(1):77-89.

[13] Murdock RC, Braydich-Stolle L, Schrand AM, Schlager JJ, Hussain SM. Characterization of Nanomaterial Dispersion in Solution Prior to In Vitro Exposure Using Dynamic Light Scattering Technique. Toxicol Sci 2008;101(2):239-53.

[14] Yu W, Xie H. A Review on Nanofluids: Preparation, Stability Mechanisms, and Applications. Journal of Nanomaterials 2012;2012:435873.

[15] Villamizar LC, Lohateeraparp P, Harwell JH, Resasco DE, Shiau BJ. Dispersion Stability and Transport of Nanohybrids through Porous Media. Transport Porous Media 2013;96(1):63-81.

[16] Liu HH, Surawanvijit S, Rallo R, Orkoulas G, Cohen Y. Analysis of Nanoparticle Agglomeration in Aqueous Suspensions via Constant-Number Monte Carlo Simulation. Environ Sci Technol 2011;45(21):9284–92.

[17] Hang J, Shi L, Feng X, Xiao L. Electrostatic and electrosteric stabilization of aqueous suspensions of barite nanoparticles. Powder Technol 2009;192(2):166-70.

[18] Zhu H, Zhang C, Tang Y, Wang J, Ren B, Yin Y. Preparation and thermal conductivity of suspensions of graphite nanoparticles. Carbon 2007;45(1):226-8.

[19] Tang E, Cheng G, Ma X, Pang X, Zhao Q. Surface modification of zinc oxide nanoparticle by PMAA and its dispersion in aqueous system. Appl Surf Sci 2006;252(14):5227-32.

[20] Sato K, Li JG, Kamiya H, Ishigaki T. Ultrasonic dispersion of TiO2 nanoparticles in aqueous suspension. J Am Ceram Soc 2008;91(8):2481-7.
[21] Higashitani K, Yoshida K, Tanise N, Murata H. Dispersion of coagulated colloids by ultrasonication. Colloids and Surfaces A: Physicochemical and Engineering Aspects 1993;81:167-75.
[22] Özcan-Taşkin NG, Padron G, Voelkel A. Effect of particle type on the mechanisms of break up of nanoscale particle clusters. Chem Eng Res Des 2009;87(4):468-73.
[23] Nguyen VS, Rouxel D, Hadji R, Vincent B, Fort Y. Effect of ultrasonication and dispersion stability on the cluster size of alumina nanoscale particles in aqueous solutions. Ultrason Sonochem 2011;18(1):382-8.
[24] Guzmán KAD, Taylor MR, Banfield JF. Environmental risks of nanotechnology: national nanotechnology initiative funding. Environ Sci Technol 2006;40(5):1401–7.
[25] Lecoanet HF, Bottero J-Y, Wiesner MR. Laboratory Assessment of the Mobility of Nanomaterials in Porous Media. Environ Sci Technol 2004;38(19):5164–9.
[26] Darlington TK, Neigh AM, Spencer MT, Nguyen OT, Oldenburg SJ. Nanoparticle characteristics affecting environmental fate and transport through soil. Environ Toxicol Chem 2009;28(6):1191-9.
[27] Alaskar M, Ames M, Connor S, Liu C, Cui Y, Li K, et al. Nanoparticle and Microparticle Flow in Porous and Fractured Media: An Experimental Study. SPE Annual Technical Conference and Exhibition. Denver, Colorado, USA.
[28] Godinez IG, Darnault CJG. Aggregation and transport of nano-TiO2 in saturated porous media: Effects of pH, surfactants and flow velocity. Water Res 2011;45(2):839–51.
[29] Jeong S-W, Kim S-D. Aggregation and transport of copper oxide nanoparticles in porous media. J Environ Monit 2009;11:1595-600.
[30] French RA, Jacobson AR, Kim B, Isley SL, Penn RL, Baveye PC. Influence of Ionic Strength, pH, and Cation Valence on Aggregation Kinetics of Titanium Dioxide Nanoparticles. Environ Sci Technol 2009;43(5):1354–9.
[31] Andreescu S, Njagi J, Ispas C, Ravalli MT. JEM spotlight: applications of advanced nanomaterials for environmental monitoring. J Environ Monit 2007;11:27-40.
[32] Qu X, Alvarez PJJ, Li Q. Applications of nanotechnology in water and wastewater treatment. Water Res 2013;47:3931-46.
[33] Zheng LX, O'Connell MJ, Doorn SK, Liao XZ, Zhao YH, Akhadov EA, et al. Ultralong single-wall carbon nanotubes. Nat Mater 2004;3:673-6.
[34] Jaisi DP, Saleh NB, Blake RE, Elimelech M. Transport of Single-Walled Carbon Nanotubes in Porous Media: Filtration Mechanisms and Reversibility. Environ Sci Technol 2008;42(22):8317-23.
[35] Kasel D, Bradford SA, Šimůnek J, Heggen M, Vereecken H, Klumpp E. Transport and retention of multi-walled carbon nanotubes in saturated porous media: Effects of input concentration and grain size. Water Res 2013;47(2):933–44.
[36] Tian Y, Gao B, Silvera-Batista C, Ziegler KJ. Transport of engineered nanoparticles in saturated porous media. Journal of Nanoparticle Research 2010;12(7):2371–80.
[37] Pham NH, Papavassiliou DV. Nanoparticle transport in heterogeneous porous media with particle tracking numerical methods. Computational Particle Mechanics 2016.

[38] Messina F, Icardi M, Marchisio D, Sethi R. Microscale Simulation of Nanoparticles Transport in Porous Media for Groundwater Remediation. COMSOL Conference 2012. Milan, Italy.
[39] McQuarrie DA. Statistical Mechanics. 1st ed: University Science Books; 2000.
[40] Ortiz V, Nielsen SO, Discher DE, Klein ML, Lipowsky R, Shillcock J. Dissipative Particle Dynamics Simulations of Polymersomes. J Phys Chem B 2005;109(37):17708–14.
[41] Zhao T, Wang X, Jiang L, Larson RG. Dissipative particle dynamics simulation of dilute polymer solutions—Inertial effects and hydrodynamic interactions. Journal of Rheology 2014;58(4):1039-58.
[42] Wang J-J, Li Z-Z, Gu X-P, Feng L-F, Zhang C-L, Hu G-H. A dissipative particle dynamics study on the compatibilizing process of immiscible polymer blends with graft copolymers. Polymer 2012;53(20):4448–54.
[43] N. Arai, K. Yasuoka, Zeng XC. Self-Assembly of Surfactants and Polymorphic Transition in Nanotubes. Journal of the American Chemical Society 2008;130(25):7916-20.
[44] P. Angelikopoulos, Bock H. Directed self-assembly of surfactants in carbon nanotube materials. J Phys Chem B 2008;112(44):13793–801.
[45] Maiti A, Wescott J, Kung P. Nanotube–polymer composites: insights from Flory–Huggins theory and mesoscale simulations. Mol Simul 2005;31(2-3):143-9.
[46] Chen S, Guo C, Hu G-H, Liu H-Z, Liang X-F, Wang J, et al. Dissipative particle dynamics simulation of gold nanoparticles stabilization by PEO–PPO–PEO block copolymer micelles. Colloid Polym Sci 2007;285(14):1543-52.
[47] Boek ES, Coveney PV, Lekkerkerker HNW, Schoot PVd. Simulating the rheology of dense colloidalsuspensions using dissipative particle dynamics. Phys Rev E 1997;55(3):3124-33.
[48] Hoogerbrugge PJ, Koelman J. Simulation microscopic hydrodynamics phenomena with dissipative particle dynamics. Europhys Lett 1992;19:155-60.
[49] Español P, Warren PB. Statistical Mechanics of Dissipative Particle Dynamics. Europhys Lett 1995;30(4):191-6.
[50] Huilgol RR, Phan-Thien N. Fluid Mechanics of Viscoelasticity: General Principles, Constitutive Modelling, Analytical and Numerical Techniques. Amsterdam: Elsevier; 1997.
[51] Allen MP, Tildesley DJ. Computer simulation of liquids. Oxford: Oxford University Press; 1987.
[52] Groot RD, Warren PB. Dissipative particle dynamics: Bridging the gap between atomistic and mesoscopic simulation. J Chem Phys 1997;107(11):4423-35.
[53] Plimpton SJ. Fast Parallel Algorithms for Short-Range Molecular Dynamics. J Comput Phys 1995;117:1-19.
[54] Lowe CP. An alternative approach to dissipative particle dynamics. Europhys Lett 1999;47(2):145-51.
[55] Llamas M, Giner V, Sancho M. The dynamic evolution of cell chaining in a biological suspension induced by an electrical field. Journal of Physic D: Applied Physics 1998;31(21):3160-7.
[56] Yin C, Rosendahl L, Kær SK, Sørensen H. Modelling the motion of cylindrical particles in a nonuniform flow. Chemical Enginnering Science 2003;58(15):3489 – 98.

[57] Ganser GH. A rational approach to drag prediction of spherical and nonspherical particles. Powder Technol 1993;77(2):143-52.
[58] J. M. V. A. Koelman, Hoogerbrugge PJ. Dynamic Simulations of Hard-Sphere Suspensions Under Steady Shear. Europhys Lett 1993;21:363-8.
[59] Español P. Dissipative Particle Dynamics. In: Yip S, ed. Handbook of Materials Modeling. Dordrecht, The Netherlands: Springer 2005, p. 2503-12.
[60] Kim JM, Phillips RJ. Dissipative particle dynamics simulation of flow around spheres and cylinders at finite Reynolds numbers. Chem Eng Sci 2004;59:4155 – 68.
[61] Liba O, Kauzlarić D, Abrams ZR, Hanein Y, Greiner A, Korvink JG. A dissipative particle dynamics model of carbon nanotubes. Mol Simul 2008;34(8):737-48.
[62] J. H. Walther, T. Werder, R. L. Jaffe, Koumoutsakos P. Hydrodynamic properties of carbon nanotubes. Phys Rev E 2004;69:062201.
[63] Palma PD, Valentini P, Napolitano M. Dissipative particle dynamics simulation of a colloidal micropump. Phys Fluids 2006;18:027103.
[64] Schlijper AG, Hoogerbrugge PJ, Manke CW. Computer-simulation of dilute polymer-solutions with the dissipative particle dynamics method. J Rheol 1995;39:567-79.
[65] E. E. Keaveny, I. V. Pivkin, M. Maxey, Karniadakis GE. A comparative study between dissipative particle dynamics and molecular dynamics for simple- and complex-geometry flows. J Chem Phys 2005;123:104107.
[66] Rudolf M. Füchslin, Harold Fellermann, Anders Eriksson, Ziock H-J. Coarse graining and scaling in dissipative particle dynamics. J Chem Phys 2009;130:214102.
[67] R. D. Groot, Rabone KL. Mesoscopic simulation of cell membrane damage, morphology change and rupture by nonionic surfactants. Biophys J 2001;81:725-36.
[68] Groot RD. Electrostatic interactions in dissipative particle dynamics—simulation of polyelectrolytes and anionic surfactants. J Chem Phys 2003;118:11265.
[69] Probstein RF. Physicochemical Hydrodynamics. London: Butterworths; 1989.
[70] Batchelor GK. An Introduction to Fluid Dynamics. 1st ed. Cambridge: Cambridge University Press; 1967.
[71] Ou J, Perot B, Rothstein JP. Laminar drag reduction in microchannels using ultrahydrophobic surfaces. Phys Fluids 2004;16:4635-43.
[72] Roman S. Voronov, Dimitrios V. Papavassiliou, Lee LL. Slip length and contact angle over hydrophobic surfaces. Chem Phys Lett 2007;441(4-6):273-6.
[73] Vega C, McBride C, Sanz E, Abascal JL. Radial distribution functions and densities for the SPC/E, TIP4Pand TIP5P models for liquid water and ices Ih,Ic, II, III, IV, V,VI, VII, VIII, IX, XI and XII. Phys Chem Chem Phys 2005;7:1450–6.
[74] Igor V. Pivkin, Karniadakis GE. Controlling Density Fluctuations in Wall-Bounded Dissipative Particle Dynamics Systems. Phys Rev Lett 2006;96:206001.
[75] Altenhoff AM, Walther JH, Koumoutsakos P. A stochastic boundary forcing for dissipative particle dynamics. J Comput Phys 2007;225:1125-36.
[76] S. Chen, N. Phan-Thien, B. C. Khoo and X. J. Fan. Flow around spheres by dissipative particle dynamics. Phys Fluids 2006;18(10):103605.
[77] Harinath Reddy, Abraham J. Dissipative-particle dynamics simulations of flow over a stationary sphere in compliant channels. Phys Fluids 2009;21:053303.
[78] Igor V. Pivkin, Karniadakis GE. Coarse-graining limits in open and wall-bounded dissipative particle dynamics systems. J Chem Phys 2006;124:184101.

[79] Trofimov S. Thermodynamic consistency in dissipative particle dynamics. Technische Universiteit Eindhoven, Ph.D, 2003.
[80] Xijun Fan, Nhan Phan-Thien, Ng Teng Yong, Xuhong Wu, Xu D. Microchannel flow of a macromolecular suspension. Phys Fluids 2003;15:11-21.
[81] Z. Li, Drazer G. Hydrodynamic interactions in dissipative particle dynamics. Phys Fluids 2008;20(10):103601.
[82] Kumar A, Asako Y, Abu-Nada E, Krafczyk M, Faghri M. From dissipative particle dynamics scales to physical scales: a coarse-graining study for water flow in microchannel. Microfluid Nanofluidics 2009;7(4):467-77.
[83] D. Pan, N. Phan-Thien, N. Mai-Duy, Khoo BC. Numerical investigations on the compressibility of a DPD fluid. J Comput Phys 2013;242:196-210.
[84] Wang J. Carbon-Nanotube Based Electrochemical Biosensors: A Review. Electroanalysis 2004;17(1):7-14.
[85] Bhushan B. Springer Handbook of Nanotechnology. Berlin: Springer; 2006.
[86] Liu Z, Robinson JT, Tabakman SM, Yang K, Dai H. Carbon materials for drug delivery & cancer therapy. Materials Today 2011;14(7-8):316-23.
[87] Chung HT, Won JH, Zelenay P. Active and stable carbon nanotube/nanoparticle composite electrocatalyst for oxygen reduction. Nature Communications 2013;4:1922.
[88] Hopley EL, Salmasi S, Kalaskar DM, Seifalian AM. Carbon nanotubes leading the way forward in new generation 3D tissue engineering. Biotechnology Advances 2014;32(5):1000-14.
[89] ShamsiJazeyi H, Miller CA, Wong MS, Tour JM, Verduzco R. Polymer-coated nanoparticles for enhanced oil recovery. J Appl Polym Sci 2014;131(15):40576.
[90] Shenderova OA, Zhirnov VV, Brenner DW. Carbon Nanostructures. Crit Rev Solid State Mater Sci 2002;27(3-4):227-356.
[91] Buford MC, Hamilton RFJ, Holian A. A comparison of dispersing media for various engineered carbon nanoparticles. Particle and Fibre Toxicology 2007;4(6).
[92] Tarn D, Ashley CE, Xue M, Carnes EC, Zink JI, Brinker CJ. Mesoporous Silica Nanoparticle Nanocarriers: Biofunctionality and Biocompatibility. Acc Chem Res 2013;46(3):792-801.
[93] O'Connell MJ, Boul P, Ericson LM, Huffman C, Wang Y, Haroz E, et al. Reversible water-solubilization of single-walled carbon nanotubes by polymer wrapping. Chem Phys Lett 2001;342:265-71.
[94] Nativ-Roth E, Shvartzman-Cohen R, Bounioux Cl, Florent M, Zhang D, Szleifer I, et al. Physical Adsorption of Block Copolymers to SWNT and MWNT: A Nonwrapping Mechanism. Macromolecules 2007;40(10):3676-85.
[95] Zhao L, Seth A, Wibowo N, Zhao C-X, Mitter N, Yu C, et al. Nanoparticle vaccines. Vaccine 2014;32(3):327-37.
[96] Gregory AE, Titball R, Williamson D. Vaccine delivery using nanoparticles. Frontiers in Cellular and Infection Microbiology 2013;3:13.
[97] Zhang H, Yu M, Song H, Noonan O, Zhang J, Yang Y, et al. Self-Organized Mesostructured Hollow Carbon Nanoparticles via a Surfactant-Free Sequential Heterogeneous Nucleation Pathway. Chem Mater 2015;27(18):6297-304.
[98] Gupta S, Bansal R, Gupta S, Jindal N, Jindal A. Nanocarriers and nanoparticles for skin care and dermatological treatments. Indian Dermatology Online Journal 2013;4(4):267-72.

[99] Ganeshkumar M, Ponrasu T, Sathishkumar M, Suguna L. Preparation of amphiphilic hollow carbon nanosphere loaded insulin for oral delivery. Colloids and Surfaces B: Biointerfaces 2013;103:238-43.
[100] Yamashita T, Yamashita K, Nabeshi H, Yoshikawa T, Yoshioka Y, Tsunoda S-i, et al. Carbon Nanomaterials: Efficacy and Safety for Nanomedicine. Materials 2012;5(2):350-63.
[101] Zhang M, Yamaguchi T, Iijima S, Yudasaka M. Size-dependent biodistribution of carbon nanohorns in vivo. Nanomedicine: Nanotechnology, Biology and Medicine 2013;9(5):657-64.
[102] Liu Z, Robinson JT, Sun X, Dai H. PEGylated Nano-Graphene Oxide for Delivery of Water Insoluble Cancer Drugs. J Am Chem Soc 2008;130(33):10876-7.
[103] Skandani AA, Al-Haik M. Reciprocal effects of the chirality and the surface functionalization on the drug delivery permissibility of carbon nanotubes. Soft Matter 2013;9:11645-9.
[104] Pham NH, Swatske DP, Harwell JH, Shiau B-J, Papavassiliou DV. Transport of nanoparticles and kinetics in packed beds: A numerical approach with lattice Boltzmann simulations and particle tracking. Int J Heat Mass Transfer 2014;72:319-28.
[105] Pham NH, Chen C, Shiau B, Harwell JH, Resasco DE, Papavassiliou DV. Transport and deposition kinetics of polymer-coated multiwalled carbon nanotubes in packed beds. AIChE J 2016;62(10):3774–83.
[106] Villamizar LC, Lohateeraparp P, Harwell JH, Resasco DE, Shiau B. Interfacially Active SWNT/Silica Nanohybrid Used In Enhanced Oil Recovery. SPE Improved Oil Recovery Symposium. Tulsa, Oklahoma, USA: Society of Petroleum Engineers. http://dx.doi.org/10.2118/129901-MS.
[107] Baez J, Ruiz MP, Faria J, Harwell JH, Shiau B, Resasco DE. Stabilization of Interfacially-Active-Nanohybrids/Polymer Suspensions and Transport through Porous Media. SPE Improved Oil Recovery Symposium. Tulsa, Oklahoma, USA: Society of Petroleum Engineers. http://dx.doi.org/10.2118/154052-MS.
[108] Vo M, Papavassiliou DV. Interaction parameters between carbon nanotubes and water in Dissipative Particle Dynamics. Mol Simul 2016;42(9):737-44.
[109] Pivkin IV, Karniadakis GE. A new method to impose no-slip boundary conditions in dissipative particle dynamics. J Comput Phys 2005;207(1):114-28.
[110] Lees AW, Edwards SF. The computer study of transport processes under extreme conditions. Journal of Physics C: Solid State Physics 1972;5(15):1921-9.
[111] Teraoka I. Polymer solutions: An introduction to physical properties. New York: John Wiley & Sons, Inc.; 2002.
[112] Kokuoz B, Kornev KG, Luzinov I. Gluing Nanoparticles with a Polymer Bonding Layer: The Strength of an Adhesive Bond. ACS Appl Mater Interfaces 2009;1(3):575–83.
[113] McFarlane NL, Wagner NJ, Kaler EW, Lynch ML. Poly(ethylene oxide) (PEO) and Poly(vinyl pyrolidone) (PVP) Induce Different Changes in the Colloid Stability of Nanoparticles. Langmuir 2010;26(17): 13823–30.
[114] Fleer GJ, Scheutjens JMHM. Adsorption of interacting oligomers and polymers at an interface. Adv Colloid Interface Sci 1982;16(1):341-59.
[115] Wichterle K, Sobolik V, Lutz M, Denk V. Shera rate on centrifugal pump impeller. Chem Eng Sci 1996;51(23):5227-8.

[116] Pipe CJ, Majmudar TS, McKinley GH. High shear rate viscometry. Rheol Acta 2008;47(5-6):621-42.
[117] Goncalves FD, Ahmadian M, Carlson JD. Investigating the magnetorheological effect at high flow velocities. Smart Materials and Structures 2006;15(1):75-85.
[118] Pham NH, Voronov RS, Tummala NR, Papavassiliou DV. Bulk stress distributions in the pore space of sphere-packed beds under Darcy flow conditions. Phys Rev E 2014;89(3):033016.
[119] Thomas S, Farouq Ali SM. Miscellar Flooding and ASP – Chemical Methods for Enhanced Oil Recovery. Annual Technical Meeting, Calgary, Alberta, June 14 - 18th, 1999: Petroleum Society of Canada.
[120] Melrose JC, Brandner CF. Role of Capillary Forces In Detennining Microscopic Displacement Efficiency For Oil Recovery By Waterflooding. Journal of Canadian Petroleum Technology 1974;13(4):54-62.
[121] Zaitoun A, Fonseca C, Berger P, Bazin B, Monin N. New Surfactant for Chemical Flood in High-Salinity Reservoir. International Symposium on Oilfield Chemistry, Houston, Texas, 5-7 February, 2003: Society of Petroleum Engineers.
[122] Dawe B, Oswald T. Reduced adsorption and separation of blended surfactant on sand and clay. Journal of Canadian Petroleum Technology 1991;30(2):133-7.
[123] Liu Q, Dong M, Zhou W, Ayub M, Zhang YP, Huang S. Improved oil recovery by adsorption–desorption in chemical flooding. J Pet Sci Eng 2004;43(1-2):75-86.
[124] Tummala NR, Striolo A. SDS Surfactants on Carbon Nanotubes: Aggregate Morphology. ACS Nano 2009;3(3):595-602.
[125] Lin S, Blankschtein D. Role of the Bile Salt Surfactant Sodium Cholate in Enhancing the Aqueous Dispersion Stability of Single-Walled Carbon Nanotubes: A Molecular Dynamics Simulation Study. J Phys Chem B 2010;114(47):15616–25.
[126] Sohrabi B, Poorgholami-Bejarpasi N, Nayeri N. Dispersion of Carbon Nanotubes Using Mixed Surfactants: Experimental and Molecular Dynamics Simulation Studies. J Phys Chem B 2014;118(11):3094-103.
[127] Arai N, Yasuoka K, Zeng XC. Self-Assembly of Surfactants and Polymorphic Transition in Nanotubes. J Am Chem Soc 2008;130(25):7916-20.
[128] Lu JR, Li ZX, Thomas RK, Staples EJ, Tucker I, Penfold J. Neutron Reflection from a Layer of Monododecyl Hexaethylene Glycol Adsorbed at the Air-Liquid Interface: The Configuration of the Ethylene Glycol Chain. J Phys Chem 1993;97(30):8012-20.
[129] Rosen MJ. Surfactants and Interfacial Phenomena. 2nd ed. New York: John Wiley and Sons; 1989.
[130] Velinova M, Sengupta D, Tadjer AV, Marrink S-J. Sphere-to-Rod Transitions of Nonionic Surfactant Micelles in Aqueous Solution Modeled by Molecular Dynamics Simulations. Langmuir 2011;27(23):14071–7.
[131] Denham N, Holmes MC, Zvelindovsky AV. The Phases in a Non-Ionic Surfactant (C12E6)−Water Ternary System: A Coarse-Grained Computer Simulation. J Phys Chem B 2011;155(6):1385-93.
[132] Mai Z, Couallier E, Rakib M, Rousseau B. Parameterization of a mesoscopic model for the self-assembly of linear sodium alkyl sulfates. J Chem Phys 2014;140(20):204902-12.
[133] Duan B, Zhang X, Qiao B, Kong B, Yang X. Description of Ionic Surfactant/Water System by Adjusting Mesoscopic Parameters. J Phys Chem B

2009;113(26):8854–9.
[134] Maiti A, McGrother S. Bead–bead interaction parameters in dissipative particle dynamics: Relation to bead-size, solubility parameter, and surface tension. J Chem Phys 2004;120(3):1594-601.
[135] Kuo M-Y, Yang H-C, Hua C-Y, Chen C-L, Mao S-Z, Deng F, et al. Computer Simulation of Ionic and Nonionic Mixed Surfactants in Aqueous Solution. ChemPhysChem 2004;5(4):575-80.
[136] Vishnyakov A, Lee M-T, Neimark AV. Prediction of the Critical Micelle Concentration of Nonionic Surfactants by Dissipative Particle Dynamics Simulations. Journal of Physical Chemistry Letters 2013;4(5):797-802.
[137] Lee M-T, Vishnyakov A, Neimark AV. Calculations of Critical Micelle Concentration by Dissipative Particle Dynamics Simulations: The Role of Chain Rigidity. J Phys Chem B 2013;117(35):10304-10.
[138] Maiti PK, Lansac Y, Glaser MA, Clark NA. Self-Assembly in Surfactant Oligomers: A Coarse-Grained Description through Molecular Dynamics Simulations. Langmuir 2002;18(5):1908-18.
[139] Witthayapanyanon A, Acosta EJ, Harwell JH, Sabatini DA. Formulation of ultralow interfacial tension systems using extended surfactants. J Surfactants Deterg 2006;9(4):331-9.
[140] Rudnick J, Gaspari G. The aspherity of random walks. J Phys A: Math Gen 1986;19(4):L191-L3.
[141] Noguchi H, Yoshikawa K. Morphological variation in a collapsed single homopolymer chain. J Chem Phys 1998;109(12):5070-7.
[142] Becher P. Nonionic surface-active compounds IV. Micelle formation by polyoxyethylene alkanols and alkyl phenols in aqueous solution. Journal of Colloid Science 1961;16(1):49-56.
[143] Clint JH. Surfactant Aggregation. New York: Springer Science+Business Media; 1992.
[144] Akbaş H, Işcan M, Sidim T. Composition of mixed anionic/nonionic surfactant micelles. J Surfactants Deterg 2000;3(1):77-80.
[145] Richard C, Balavoine F, Schultz P, Ebbesen TW, Mioskowski C. Supramolecular Self-Assembly of Lipid Derivatives on Carbon Nanotubes. Science 2003;300(5620):775-8.
[146] Nativ-Roth E, Yerushalmi-Rozen R, Regev O. Phase Behavior and Shear Alignment in SWNT-Surfactant Dispersions. Small 2008;4(9):1459-67.
[147] Islam MF, Rojas E, Bergey DM, Johnson AT, Yodh AG. High Weight Fraction Surfactant Solubilization of Single-Wall Carbon Nanotubes in Water. Nano Lett 2003;3(2):269-73.
[148] Moore VC, Strano MS, Haroz EH, Hauge RH, Smalley RE. Individually Suspended Single-Walled Carbon Nanotubes in Various Surfactants. Nano Lett 2003;3(10):1379-82.
[149] Wadell H. Volume, Shape, and Roundness of Quartz Particles. The Journal of Geology 1935;43(3):250-80.
[150] Spaeth JR, Kevrekidis IG, Panagiotopoulos AZ. A comparison of implicit- and explicit-solvent simulations of self-assembly in block copolymer and solute systems. J Chem Phys 2011;134:164902.

[151] Zhao T, Wang X. Diffusion of rigid rodlike polymer in isotropic solutions studied by dissipative particle dynamics simulation. Polymer 2013;54(19):5241–9.
[152] Streletzky K, Phillies GDJ. Temperature Dependence of Triton X-100 Micelle Size and Hydration. Langmuir 1995;11(1):42-7.
[153] Abe M, Scamehorn JF. Mixed surfactant systems. 2nd ed. New York: Marcel Dekker; 2004.
[154] Baughman RH, Zakhidov AA, Heer WAd. Carbon Nanotubes—the Route Toward Applications. Science 2002;297:787-92.
[155] Ijima S, Ichiashi T. Single-shell carbon nanotubes of 1-nm diameter. Nature 1993;363:603-5.
[156] Wang X, Li Q, Xie J, Jin Z, Wang J, Li Y, et al. Fabrication of Ultralong and Electrically Uniform Single-Walled Carbon Nanotubes on Clean Substrates. Nano Lett 2009;9(9):3137-41.
[157] Dujardin E, Ebbesen TW, Hiura H, Tanigaki K. Capillarity and Wetting of Carbon Nanotubes. Science 1994;265(5180):1850-2.
[158] Gadd GE, Blackford M, Moricca S, Webb N, Evans PJ, Smith AM, et al. The World's Smallest Gas Cylinders? Science 1997;277(5328):933-6.
[159] Kuznetsova A, Jr. JTY, Liu J, Smalley RE. Physical adsorption of xenon in open single walled carbon nanotubes: Observation of a quasi-one-dimensional confined Xe phase. J Chem Phys 2000;112(21):9590-8.
[160] Yano H, Yoshizaki S, Inagaki S, Fukushima Y, Wada N. Observation of Superfluid ^{4}He Adsorbed in One-Dimensional Mesopores. J Low Temp Phys 1998;110(1):573-8.
[161] Gordillo MC, Boronat J, Casulleras J. Quasi-one-dimensional ^{4}He inside carbon nanotubes. Physical Review B 1999;61(2):878-81.
[162] Pan X, Bao X. The Effects of Confinement inside Carbon Nanotubes on Catalysis. Acc Chem Res 2011;44(8):553-62.
[163] Lee B, Baek Y, Lee M, Jeong DH, Lee HH, Yoon J, et al. A carbon nanotube wall membrane for water treatment. Nature Communications 2015;6:7109.
[164] Davis JJ, Green MLH, Hill HAO, Leung YC, Sadler PJ, Sloan J, et al. The immobilisation of proteins in carbon nanotubes. Inorg Chim Acta 1998;272(1-2):261-6.
[165] Fujiwara A, Ishii K, Suematsu H, Kataura H, Maniwa Y, Suzuki S, et al. Gas adsorption in the inside and outside of single-walled carbon nanotubes. Chem Phys Lett 2001;336(3-4):205-11.
[166] Pan X, Fan Z, Chen W, Ding Y, Luo H, Bao X. Enhanced ethanol production inside carbon-nanotube reactors containing catalytic particles. Nat Mater 2007;6:507-11.
[167] Sun MZ, Duan WH, Wang Q, Dowman M, Kodikara J. Driving Forces and Transportation Efficiency in Water Transportation Through Single-Walled Carbon Nanotubes. Journal of Nanotechnology in Engineering and Medicine 2012;3(2):020904.
[168] Hummer G, Rasaiah JC, Noworyta JP. Water conduction through the hydrophobic channel of a carbon nanotube. Nature 2001;414:188-90.
[169] Walther JH, Ritos K, Cruz-Chu ER, Megaridis CM, Koumoutsakos P. Barriers to Superfast Water Transport in Carbon Nanotube Membranes. Nano Lett 2013;13(5):1910-4.
[170] Anastassiou A, Karahaliou EK, Alexiadis O, Mavrantzas VG. Detailed atomistic simulation of the nano-sorption and nano-diffusivity of water, tyrosol, vanillic acid, and

p-coumaric acid in single wall carbon nanotubes. J Chem Phys 2013;139:164711.
[171] Nagarajan R, Wang C-C. Theory of Surfactant Aggregation in Water/Ethylene Glycol Mixed Solvents. Langmuir 2004;16(12):5242-51.
[172] Thomas JA, McGaughey AJH. Water Flow in Carbon Nanotubes: Transition to Subcontinuum Transport. Phys Rev Lett 2009;102:184502.
[173] Wua H, Xu J, He X, Zhao Y, Wen H. Mesoscopic simulation of self-assembly in surfactant oligomers by dissipative particle dynamics. Colloids and Surfaces A: Physicochemical and Engineering Aspects 2006;290(1-3):239-46.
[174] Cifuentes A, Bernal JL, Diez-Masa JC. Determination of Critical Micelle Concentration Values Using Capillary Electrophoresis Instrumentation. Anal Chem 1997;69(20):4271-4.
[175] Farimani AB, Aluru NR. Spatial Diffusion of Water in Carbon Nanotubes: From Fickian to Ballistic Motion. J Phys Chem B 2011;115(42):12145-9.
[176] Duan WH, Wang Q, Collins F. Dispersion of carbon nanotubes with SDS surfactants: a study from a binding energy perspective. Chemical Science 2011;2(7):1407-13.
[177] Vo MD, Shiau B, Harwell JH, Papavassiliou DV. Adsorption of anionic and non-ionic surfactants on Carbon nanotubes in water with Dissipative Particle Dynamics simulation. J Chem Phys 2016;144(20):204701.
[178] Girifalco LA, Hodak M, Lee RS. Carbon nanotubes, buckyballs, ropes, and a universal graphitic potential. Physical Review B 2000;62(19):13104-10.
[179] Tang BZ, Xu H. Preparation, Alignment, and Optical Properties of Soluble Poly(phenylacetylene)-Wrapped Carbon Nanotubes. Macromolecules 1999;32(8):2569–76.
[180] Lemasson FA, Strunk T, Gerstel P, Hennrich F, Lebedkin S, Barner-Kowollik C, et al. Selective dispersion of single-walled carbon nanotubes with specific chiral indices by poly(N-decyl-2,7-carbazole). J Am Chem Soc 2010;133(4):652-5.
[181] Nap R, Szleifer I. Control of Carbon Nanotube−Surface Interactions: The Role of Grafted Polymers. Langmuir 2005;21(26):12072–5.
[182] Aztatzi-Pluma D, Castrejón-González EO, Almendarez-Camarillo A, Alvarado JFJ, Durán-Morales Y. Study of the Molecular Interactions between Functionalized Carbon Nanotubes and Chitosan. J Phys Chem C 2016;120(4):2371–8.
[183] Zheng Q, Xue Q, Yan K, Hao L, Li Q, Gao X. Investigation of Molecular Interactions between SWNT and Polyethylene/Polypropylene/Polystyrene/Polyaniline Molecules. J Phys Chem C 2007;111(12):4628–35.
[184] Müter D, Angelikopoulos P, Bock H. Angular Dependence of Surfactant-Mediated Forces Between Carbon Nanotubes. Journal of Physcal Chemistry B 2012;116(51):14869–75.
[185] Motulsky HJ, Brown RE. Detecting outliers when fitting data with nonlinear regression – a new method based on robust nonlinear regression and the false discovery rate. Bioinformatics 2006;7-123.
[186] Henn AR. Calculation of the Stokes and aerodynamic equivalent diameters of a short reinforcing fiber. Particle & Particle Systems Characterization 1996;13(4):249–53.
[187] Voronov R, VanGordon S, Sikavitsas VI, Papavassiliou DV. Computational modeling of llow-induced shear stresses within 3d salt-leached porous scaffolds imaged

via micro-CT. Journal of Biomechanics 2010;43:1279-86.
[188] Qian YH, D'Humières D, Lallemand P. Lattice BGK models for Navier-Stokes equation. Europhys Lett 1992;17(6):479-84.
[189] Bhatnagar PL, Gross EP, Krook M. A model for collision processes in gases. I. Small amplitude processes in charged and neutral one-component systems. Physical Review 1954;94(3):511-25.
[190] Chen S, Doolen GD. Lattice Boltzmann method for fluid flows. Annual Review of Fluid Mechanics 1998;30:329-64.

Appendices

A1. Sphericity of particles with different shapes

Sphericity indicates quantitatively how round a particle is [149]. For unknown shape of an object, it can determine its shape via sphericity value in the following table.

Table A1. The sphericity of several particle shape.

Particle shape	Sphericity
- Tetrahedron	0.671
- Cube	0.806
- Octahedron	0.846
- Cylinder (height is equal to diameter)	0.874
- Dodecahedron	0.910
- Icosahedrons	0.939
- Sphere	1
- Hemisphere	0.840
- Part of a half-sphere (see Figure A1)	
○ V=37.32% V_{hs}	0.810
○ V=20.46% V_{hs}	0.731
○ V=11.05% V_{hs}	0.657
○ V=2.42% V_{hs}	0.543

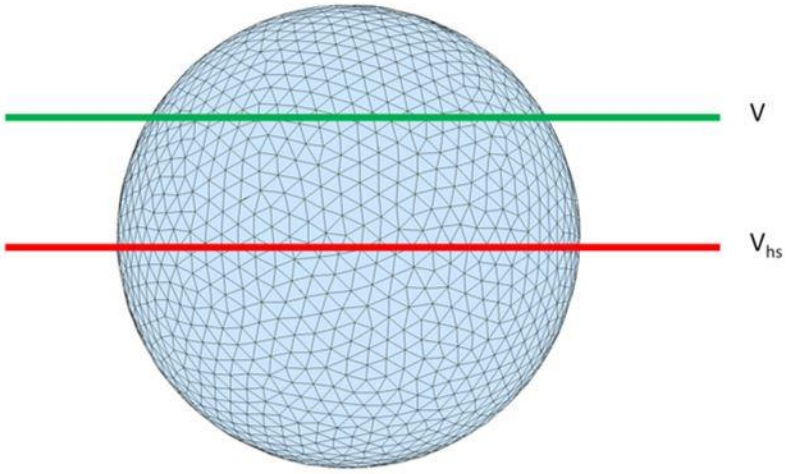

Figure A1. Definition shape of the part of a half-sphere. Above red line, V_{hs} is the volume of a half-sphere. Above green line, V is the volume of a part of the half-sphere.

A2. Mean squared displacement vs time

To display the actual diffusion behavior of surfactant molecules, the following plots of mean squared displacement with respect to time for all simulation cases were drawn.

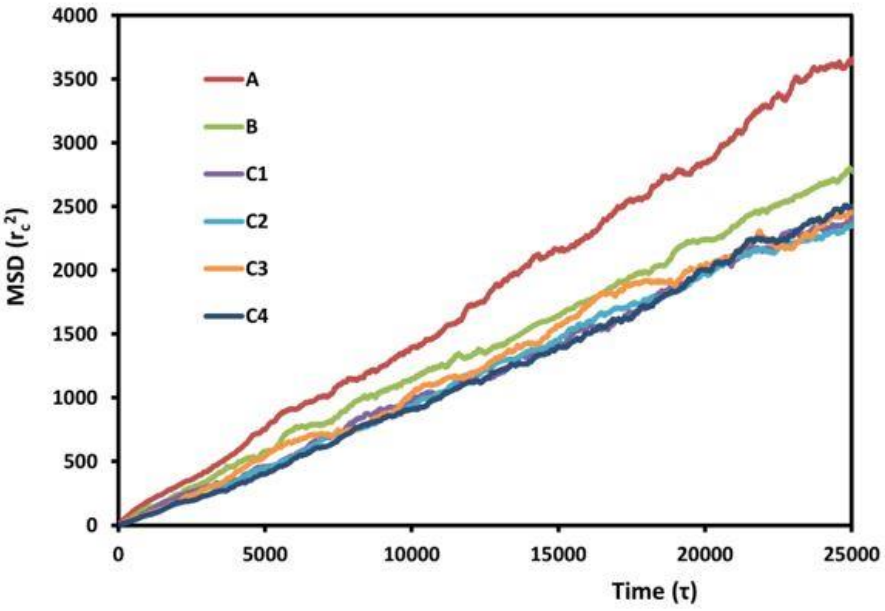

Figure A2. The mean squared displacement of surfactant micelles in water with respect

to time. The different lines correspond to different simulation runs, as described in Table 5.6.

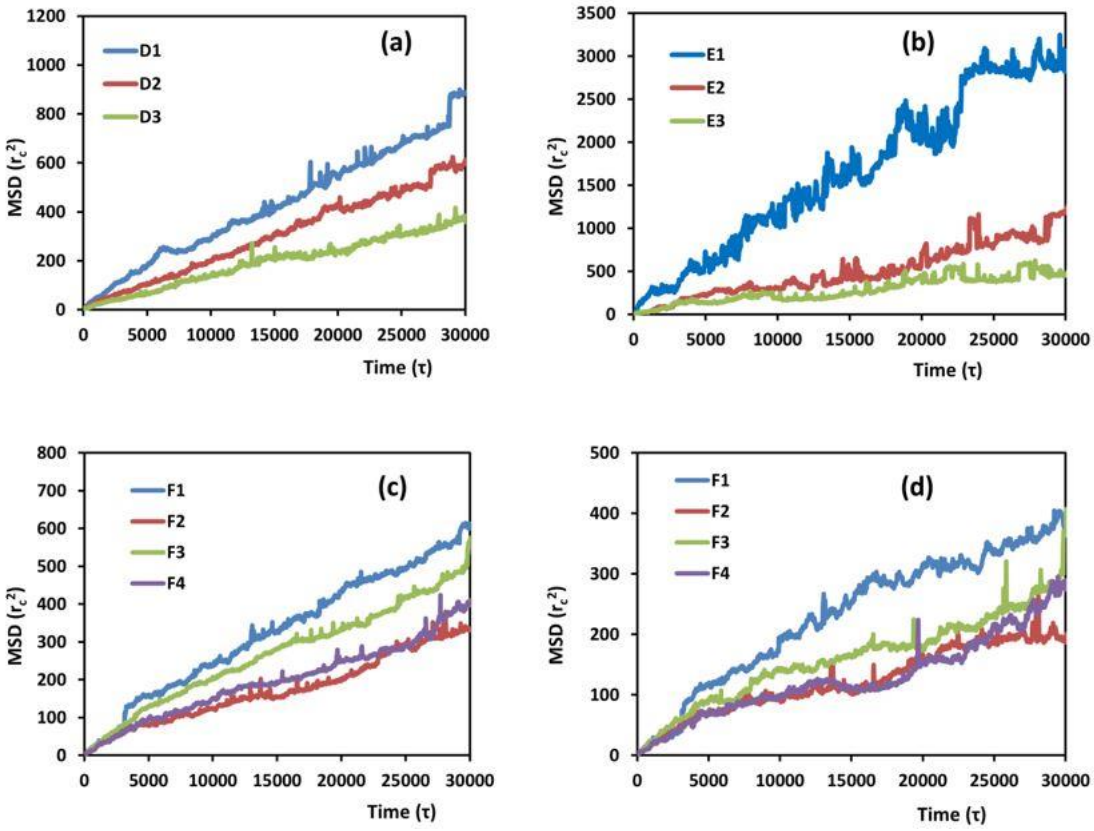

Figure A3. The mean squared displacement of surfactant on the CNT surface with respect to time. (a) AF, (b) TG, (c) AF in the binary surfactant system and (d) TG in the binary surfactant system. The different lines correspond to different simulation runs, as described in Table 5.6.

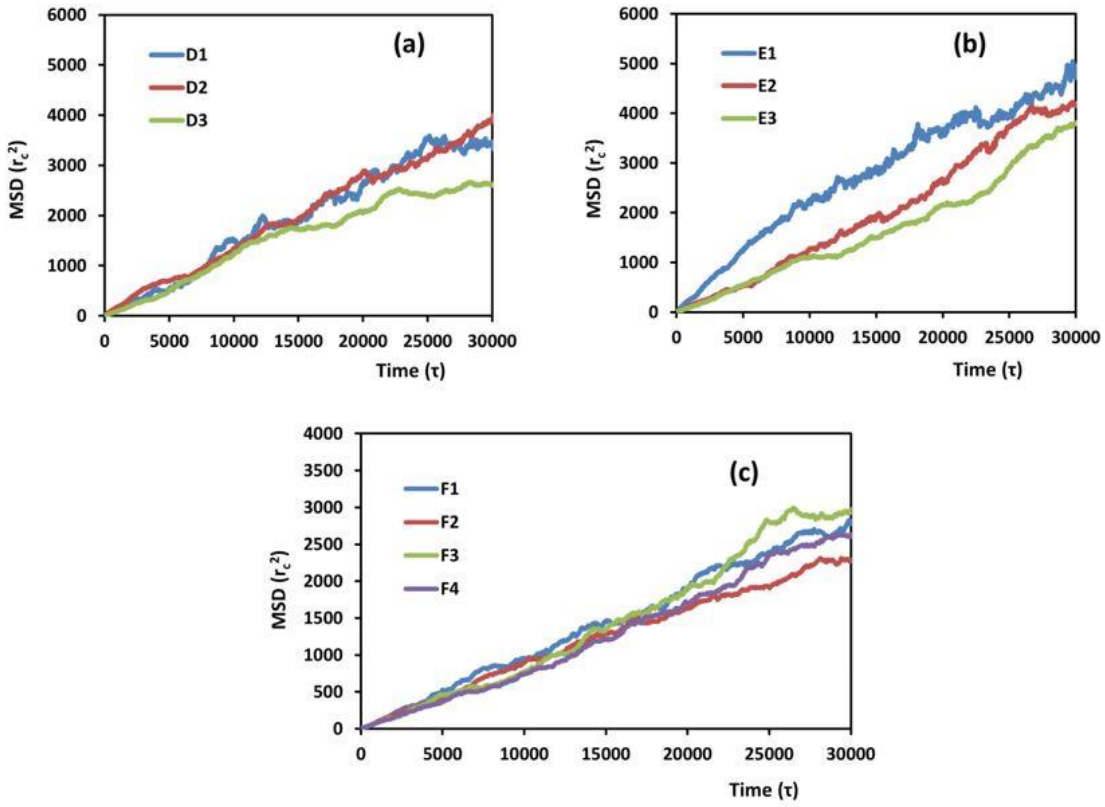

Figure A4. The mean squared displacement of surfactant in the bulk phase with respect to time. (a) AF, (b) TG and (c) AF and TG in the binary surfactant system. The different lines correspond to different simulation runs, as described in Table 5.6.

A3. Lattice Boltzmann method

Lattice Boltzmann Method (LBM) can provide the velocity within the porous media. A custom-written code has been developed, the details of which can be found in Voronov et al. [187].

In LBM, the geometry of the porous medium is discretized into lattice points (solid walls are the ones that are described by logical 'TRUE' value and void pores are described as logical 'FALSE'). The fluid flow is simulated by calculating the collisions and interactions between fluid particles that move on a rectangular lattice in phase space by

solving the discrete Boltzmann equation. The Boltzmann equation is an evolution equation for a single particle probability distribution function that is calculated as a function of space and time as follows:

$$\underbrace{f_i(\vec{x}+\vec{e}_i\Delta t, t+\Delta t) = f_i(\vec{x},t)}_{STREAMING} + \underbrace{\Omega_i(\vec{x},t)}_{COLLISION} \pm \underbrace{ff_i}_{FORCING}$$

(A3.1)

where f is the particle distribution function, $\vec{x}$ is position, t is time, Δt is the time step, $\vec{e}$ is the microscopic velocity, Ω is the collision operator, ff is the forcing factor (pressure drop over length)and the subscript 'i' is a lattice direction index (there are 15 such directions in our model, which is commonly called D3Q15 in the LBM literature [188]).

The terms on the right hand side of Equation (A3.1) constitute the three steps of the Lattice Boltzmann algorithm, namely the streaming, collision and forcing steps. Several collision models are available, but the simplest and most commonly used is the single-relaxation time approximation of the collision term given by Bhatnagar-Gross and Krook (BGK) [189]. In the BGK model, the collision operator is approximated as

$$\Omega_i(\vec{x},t) = -\frac{1}{\tau}(f_i - f_i^{eq})$$

(A3.2)

where the particle equilibrium distribution function, f^{eq}, is given by

$$f_i^{eq}(\vec{x}) = w_i \rho(\vec{x})\left[1 + 3\frac{\vec{e}_i \cdot \vec{U}}{c^2} + 9\frac{(\vec{e}_i \cdot \vec{U})^2}{c^4} - \frac{3}{2}\frac{\vec{U}^2}{c^2}\right]$$

(A3.3)

where c=Δx/Δt is the lattice speed, Δx is the lattice constant, w is a lattice specific weighing factor and U is the macroscopic velocity. The time τ appearing in Equation (A3.2) is the time scale with which the local particle distribution function relaxes to equilibrium, and is often referred to as the "relaxation time". It is related to the kinematic viscosity of the fluid:

$$\nu = \frac{1}{3}\left(\tau - \frac{1}{2}\right)$$

(A3.4)

The final step in the LBM algorithm is to calculate the macroscopic properties of the fluid such as density, ρ, and velocity, U, at any instant, from the conservation equations of mass and momentum given by

$$\rho = \sum_{i=0}^{n} f_i$$

(A3.5)

$$\rho\vec{U} = \sum_{i=0}^{n} f_i \vec{e}_i$$

(A3.6)

where *n* is the number of allowable directions that the fluid particles are allowed to move, in addition to the zero position, which is the rest position that a fluid particle can stay when it does not move. The simulation mesh consists of N_X, N_Y and N_Z nodes in the *x*, *y* and *z* directions, respectively. Among these, *fluid* nodes are those within the flow field (i.e., within the empty pore space, given the logical value "TRUE") and *wall* nodes are those that make up the rigid wall (those given the logical value "FALSE"). The velocity

field generated by solving the above equation is equivalent to solving the Navier-Stokes equations for single-phase or multi-phase flows through the pore spaces with 2^{nd} order accuracy [190]. Periodic boundary conditions were applied in all three directions. The no-slip boundary condition was applied at the wall faces using the "bounce-back" technique. In order to take advantage of the LBM parallelizability, the domain was decomposed using message passing interface.